A New Boussinesq-Type Model for Surface Water Wave Propagation

Maurício Felga Gobbi and James T. Kirby

RESEARCH REPORT NO. CACR-98-01
January, 1998

Center for Applied Coastal Research
Ocean Engineering Laboratory
University of Delaware
Newark, DE 19716
U.S.A.

ACKNOWLEDGEMENTS

This work has been supported by the Brazilian agency Coordenação de Aperfeiçoamento de Pessoal de Nível Superior (CAPES), and by the U. S. Army Research Office through University Research Initiative grant DAAL 03-92-G-0116. This report is identical to the Ph. D. dissertation by the first author, submitted to the University of Delaware in December 1997.

TABLE OF CONTENTS

LIST OF FIGURES

LIST OF TABLES

ABSTRACT

A new Boussinesq-type model for surface water wave propagation in coastal regions is derived. The model is fully nonlinear and accurate to $O(\mu^4)$, where μ is the wave number nondimensionalized by the water depth. As an extension to the second order model proposed by Nwogu (1993), a new dependent variable is defined as a weighted average between the velocity potential at two distinct water depths to force the model to have a (4,4) Padé approximation of the exact linear dispersion relationship. The fourth order polynomial approximation for the velocity potential vertical profile represents a great improvement over existing $O(\mu^2)$ models, specially over the intermediate to deep water range. Nonlinear effects including generation of super and subharmonics, and amplitude dispersion are investigated. A finite-difference numerical scheme is developed for the 1-dimensional version of the model for the free surface displacement and a velocity-type variable. Several solitary wave solutions are studied and compared with other models, as well as the solution to the full problem. Computations of waves propagating over submerged bars are compared with laboratory measurements and with results of the fully nonlinear $O(\mu^2)$ Boussinesq model by Wei et all (1995). All computations show that the present model represents a considerable improvement over the $O(\mu^2)$ model.

Chapter 1

INTRODUCTION

One of the most important tasks of coastal engineers is to accurately predict waves in coastal regions. Wind generated waves (or surface waves) can propagate from deep ocean to the continental shelf with little energy loss. As the waves enter the continental shelf, several transformations occur directly and indirectly related to the fact that the waves can now "feel" the bottom. Deep water waves are quite well understood in terms of both linear and nonlinear wave theories. Due to the fact only the upper layer of the ocean (about half of a wave length) is affected by the presence of the waves, in deep water the treatment of the vertical dependence of the flow is simpler than in nearshore areas, as it does not depend on the bottom topography. When the waves approach the coast, the water depth is no longer large compared to the wave length, and the waves experience effects such as refraction, diffraction, reflection, shoaling, nonlinear interactions, and finally reach the surf-zone, where wave breaking takes place. At this point sudden reduction in the momentum flux of the wave causes effects such as set-up (cross-shore increase in the free surface mean level to balance the momentum flux reduction), longshore current (which, combined with the fact that wave breaking puts sediment in suspension, strongly contributes to sediment transport), among others. The basic aim of this dissertation is to contribute an accurate and reasonably efficient model capable of modeling waves from deep to shallow water up to the point of (but excluding) wave breaking.

The earliest nonlinear model in water of finite depth was due to Airy (1845), known as nonlinear long wave theory or nonlinear shallow water theory. Airy's theory assumes dispersive effects to be negligible (flow is depth independent). This is a good approximation only for very long waves (water depth is small compared to the wave length) such as tsunamis, infra-gravity waves, and waves whose length is of the order of the width of the ocean basin, in which case Coriolis effects are also important. For surface gravity waves, shallow water theory is not applicable in most of the depth range in coastal regions.

The difficulty in modeling surface wave propagation is the fact that in intermediate to shallow water, the vertical structure of the flow changes quickly, and therefore models need either to be 3-dimensional, which is computationally costly, or, somehow, to eliminate the vertical dependence, but account for its effects in the 2-dimensional (horizontal) model. The latter has been the choice adopted in almost the totality of the dispersive nonlinear wave models in existence, including the present work. We now briefly review some of these models.

1.1 Existing Boussinesq-Type Models

The earliest model which is independent of the vertical coordinate, but includes weakly dispersive and nonlinear effects, was derived by Boussinesq (1872). The model, which was derived for horizontal bottom only, assumes irrotationality of the flow, parabolic vertical dependence of the horizontal velocity (or velocity potential) and linear vertical dependence of the vertical velocity, also, it has the depth averaged horizontal velocity and the free surface elevation as the dependent variables. As an aside, in this work, we refer to Boussinesq-type (or simply Boussinesq) models as those which assume irrotationality and that the velocity potential (or horizontal velocity) has a polynomial vertical dependence, leading

to a set of equations governing the free surface elevation and a vertically independent horizontal velocity-related variable (e.g. depth-averaged velocity, total mass flux, velocity potential at the bottom, etc). Korteweg and deVries (1895) used the same assumptions as Boussinesq (1872) and, eliminating the velocity variable, derived a single equation (known as KdV equation) governing the free surface elevation of weakly nonlinear weakly dispersive long waves propagating in one direction. The KdV equation appears in many branches of physics and has received much attention, mostly due to the fact that it has analytical solutions in terms of non-elementary functions. In the case of gravity waves, well known solutions for the KdV equation are the cnoidal wave and the solitary wave.

To overcome the horizontal bottom limitation in the original Boussinesq model, which prevents the model from being a very useful tool in coastal engineering, Mei and Méhauté (1966) and Peregrine (1966) derived Boussinesq models for variable depth. The two models are similar in the sense that both use the same asymptotic assumptions (weak nonlinearity and dispersiveness), but Mei and Méhauté (1966) used the velocity at the bottom as a dependent variable, whereas Peregrine (1966) used the depth-averaged velocity. Due to its wide popularity in the coastal engineering community, the model by Peregrine (1966) is often called the standard Boussinesq model.

Although standard Boussinesq models can predict wave transformation in coastal regions with relative accuracy, its range of validity is limited to fairly shallow water (McCowan, 1987), since its linear dispersion relationship is only a polynomial approximation of the exact one. In order to be applicable in deeper water, many authors have suggested extending the validity of Boussinesq models. These "extended Boussinesq models" have adjustable rational polynomial approximations for the dispersion relationship, a major improvement over the

approximation resulting from the standard Boussinesq models.

Madsen *et al.* (1991) and Madsen and Sørensen (1992) included higher order terms with adjustable coefficients into the standard Boussinesq equations for constant and variable depth, respectively. The addition of these terms resulted in a rational polynomial expansion as the linear dispersion relationship. The coefficients were then adjusted to give better linear shoaling coefficient and a more accurate approximation to the exact linear dispersion relationship, namely, the (2,2) Padé approximant (Witting, 1984).

By defining the dependent variable as the velocity at an arbitrary depth, Nwogu (1993) achieved a rational polynomial approximation to the exact linear dispersion relationship without the need to add higher order terms to the equations. Although the arbitrary location could be chosen to give a (2,2) Padé approximant as the linear dispersion relationship, Nwogu (1993) chose an alternative value which minimized the error in the linear phase speed over some depth range. Chen and Liu (1995) derived a model analogous to Nwogu's but used a velocity potential at an arbitrary depth as the dependent variable.

Wei *et al.* (1995) used Nwogu's approach to derive a Boussinesq model (referred to henceforth as the WKGS model) without the weak nonlinearity restriction. Numerical computations showed a major improvement over the weakly nonlinear model of Nwogu, and compared well with solitary wave solutions of the full potential problem obtained with the boundary elements method by Grilli *et al.* (1989).

Schäffer and Madsen (1995) combined the idea by Madsen and Sørensen (1992) of including higher order terms in the equations with the approach of redefining the dependent variable as in Nwogu (1993), to obtain a Boussinesq

model which has an extremely accurate linear dispersion relationship given by a (4,4) Padé approximant, despite having only second order vertical polynomial approximation for the horizontal velocity.

Boussinesq-type equations can also be derived using a Hamiltonian formulation (Broer, 1974, Broer, 1975, Broer *et al.*, 1976), where the canonical variables are the free surface elevation and the velocity potential evaluated at the free surface. The equations derived by Broer do not produce a positive definite linear dispersion relationship and predicts negative phase speeds in deeper water. Improvements over Broer's model to extend the validity of the equations for shorter waves were made by Van der Veen and Wubs (1993) whose dispersion relationship is a (2,2) Padé approximant. Mooiman (1991) uses a rational polynomial approximation with arbitrary coefficients for the Hamiltonian operator, and the coefficients are determined by a minimization of the error in the linear dispersion relationship. Due to the difficulty involved in computing the kinetic energy part of the total Hamiltonian, all Hamiltonian-based models to this date are only weakly nonlinear.

1.2 Other Existing Models

Although they are the most widely used, Boussinesq models are not the only type of models that eliminate the vertical dependence from the full problem, while including dispersive and nonlinear effects.

Serre (1953) derived a fully nonlinear model consisting of equations for the horizontal velocity and the free surface elevation. In the derivation, the flow is not assumed irrotational, the horizontal velocity is assumed constant over the depth and the vertical velocity variation is assumed linear. Interestingly, the fully nonlinear version of the standard Boussinesq model (with depth average velocity)

given in Mei (1989) has the exact same form as Serre's equations, with the depth-averaged velocity replacing Serre's constant-over-depth velocity. Exact solitary wave solutions of Serre's equations were found by Su and Gardner (1969) and Seabra-Santos *et al.* (1987), and the extension to variable depth and 2-dimensional horizontal coordinates was presented by Seabra-Santos *et al.* (1987), where the transformation of solitary waves over a shelf was investigated.

Green *et al.* (1974) and Green and Naghdi (1976) derived a family of models which became known as Green-Naghdi (or GN) models. GN is a very general theory whose only assumption is that the vertical and horizontal velocities are polynomials of order N and $(N-1)$, respectively. There is no assumption regarding irrotationality, nonlinearity, or even dispersiveness (not directly, at least). With $N = 1$, GN recovers Serre's model (Kirby, 1997). By a different method, Shields and Webster (1988) derived GN equations and investigated several solutions including periodic and solitary wave properties for $N = 1$, $N = 2$, and $N = 3$, and a variable depth numerical implementation of the unsteady model with $N = 2$. The results agreed well with laboratory measurements by Hansen and Svendsen (1979). Other applications of GN models can be found in Demirbilek and Webster (1992) and Webster and Wehausen (1995).

1.3 Present Model and Dissertation Outline

Although existing Boussinesq models have relatively accurate linear dispersion relationship and no weak nonlinearity limitation, the approximation to the vertical profile of the horizontal velocity (or velocity potential) variable is only a second order polynomial, which leads to a poor representation of the internal kinematics in intermediate to deep water. The inaccuracies are even more evident in the vertical velocity, which has a linear depth dependence. To overcome this

problem, we propose a Boussinesq model which approximates the horizontal velocity (or velocity potential) by a fourth order polynomial in the vertical coordinate, and consequently a third order polynomial for the vertical velocity is achieved. In order to obtain a (4,4) Padé approximant for the exact linear dispersion relationship, a new dependent variable is introduced as the weighted average of the velocity potential at 2 different elevations in the water column. Since the weight and the locations at which the new variable is defined are arbitrary, they can be chosen so that the (4,4) Padé approximant is achieved. The resulting model is a fully nonlinear fourth order (in terms of vertical polynomial approximation to the velocity potential) model with (4,4) Padé approximant as the linear dispersion relationship. The model does not include wave breaking or bottom friction effects. The outline of the dissertation is now presented.

In Chapter 2 we derive the model starting from the full potential flow boundary value problem for an inviscid, incompressible fluid. A pair of coupled equations approximating the conservation of mass and momentum is obtained for the free surface elevation and the average (as defined above) velocity potential. A three-equation model is then derived for the free surface elevation and the average horizontal velocity vector.

In Chapter 3, we analyze some analytical properties of the model, including linear dispersion, where we obtain the (4,4) Padé approximant for the dispersion relationship, second order Stokes-type interaction in a random sea, where we present the model's ability to predict super and sub-harmonics transfer coefficients, and third order interactions in a narrow banded sea, where we derive the model's amplitude dispersion coefficient and also its Schrödinger equation governing the propagation of the envelope of wave groups.

A numerical implementation of the 1-dimensional version of the model

derived in Chapter 2 is presented in Chapter 4. Wave generation inside the domain and wave absorption by sponge layers to simulate radiation boundary conditions are also discussed and several examples are shown.

In Chapter 5, we apply the numerical implementation of the model to the propagation of solitary waves over both constant and variable depth. Several solitary wave properties are discussed and compared with other models' results.

In Chapter 6, we compare the model's predictions with data sets from two distinct laboratory experiments of regular waves propagating over a submerged bar. The results are also compared with WKGS model.

The conclusions and recommendations for future work are presented in Chapter 7.

Chapter 2

DERIVATION OF FOURTH ORDER FULLY NONLINEAR MODEL

In this chapter we derive a fully nonlinear Boussinesq-type model based on a 4^{th} order vertical polynomial for the velocity potential. A set of equations for a velocity-type variable is then given. We assume the fluid is inviscid and incompressible, and the flow is irrotational, so that a velocity potential ϕ exists and the velocity field can be written as:

$$\mathbf{u} = \nabla_3 \phi, \tag{2.1}$$

where the fluid velocity vector $\mathbf{u} \equiv (u, v, w)$, and ϕ are functions of the spatial Cartesian coordinates x, y, z and time t, and ∇_3 is the 3 dimensional gradient operator $\nabla_3 \equiv (\partial/\partial x, \partial/\partial y, \partial/\partial z)$.

The full boundary value problem for potential flow is given in terms of nondimensional variables by

$$\phi_{zz} + \mu^2 \nabla^2 \phi = 0; \quad -h \leq z \leq \delta\eta \tag{2.2}$$

$$\phi_z + \mu^2 \nabla h \cdot \nabla \phi = 0; \quad z = -h \tag{2.3}$$

$$\eta + \phi_t + \frac{1}{2}\delta \left[(\nabla\phi)^2 + \frac{1}{\mu^2} (\phi_z)^2 \right] = 0; \quad z = \delta\eta \tag{2.4}$$

$$\eta_t + \delta \nabla\phi \cdot \nabla\eta - \frac{1}{\mu^2}\phi_z = 0; \quad z = \delta\eta \tag{2.5}$$

x and y are the horizontal coordinates scaled by a representative wave number $k_0 = 2\pi/L_0$, where L_0 is a wave length, z is the vertical coordinate starting at the still water level and pointing upwards and h is the water depth, both scaled by a typical depth h_0. η is the water surface displacement scaled by a representative amplitude a_0. Two dimensionless parameters are apparent: $\delta = a_0/h_0$ and $\mu^2 = (k_0 h_0)^2$. Time t is scaled by $(k_0(gh_0)^{1/2})^{-1}$, and ϕ, the velocity potential, is scaled by $\delta h_0(gh_0)^{1/2}$. g is the acceleration due to the gravitational field, and ∇ is the 2-dimensional horizontal (x, y) gradient operator.

Integrating (2.2) over the water column and using (2.3) and (2.5), we obtain a mass conservation equation

$$\eta_t + \nabla \cdot \mathbf{M} = 0; \quad \mathbf{M} = \int_{-h}^{\delta\eta} \nabla\phi dz. \tag{2.6}$$

We now proceed to derive model equations for waves over an arbitrary bottom $h(x, y)$, and assuming $\delta = O(1)$ and $O(\mu^2) << 1$. We assume an N^{th} degree polynomial approximation for ϕ in the z coordinate:

$$\phi = \sum_{n=0}^{N} \zeta^n \phi_n(x, y, t), \tag{2.7}$$

where

$$\zeta = (h + z), \tag{2.8}$$

ϕ_n are functions of the horizontal spatial coordinates and time, and are to be determined. By taking the limit of (2.7) as $\zeta \to 0$, it is clear that ϕ_0 is the velocity potential at the bottom $\zeta = 0$. Substituting (2.7) into (2.3), we obtain an expression for ϕ_1 in terms of ϕ_0:

$$\phi_1 = -\mu^2 G \nabla h \cdot \nabla\phi_0, \tag{2.9}$$

where $G \equiv (1+\mu^2|\nabla h|^2)^{-1}$. Since we are seeking an asymptotic approximation for ϕ in terms of the parameter small parameter μ^2, it would be consistent if we expanded G in a binomial expansion around $\mu^2 = 0$. However, we choose not to do this in order to maintain the positive definiteness of this quantity as the bottom slope becomes steep. Substituting (2.7) into (2.2), and equating coefficients of like powers of ζ to zero, we obtain the following recursion formula:

$$\begin{aligned}(n+2)(n+1)\phi_{n+2} &+ \mu^2\left[(n+2)(n+1)|\nabla h|^2\phi_{n+2} + (n+1)\nabla^2 h\phi_{n+1}\right.\\ &+ \left. 2(n+1)\nabla h\cdot\nabla\phi_{n+1} + \nabla^2\phi_n\right] = 0 \qquad (2.10)\end{aligned}$$

We now use (2.9) and (2.10) to obtain ϕ_2, ϕ_3, ..., in terms of ϕ_0. The series is truncated at $N = 4$, yielding:

$$\begin{aligned}\phi &= \phi_0 - \mu^2\left(G\nabla h\cdot\nabla\phi_0\zeta + \frac{1}{2}G\nabla^2\phi_0\zeta^2\right)\\ &+ \mu^4\left\{\left[\frac{1}{2}G^2\nabla^2 h\nabla h\cdot\nabla\phi_0 + G\nabla h\cdot\nabla\left(G\nabla h\cdot\nabla\phi_0\right)\right]\zeta^2\right.\\ &+ \left[\frac{1}{6}G^2\nabla^2 h\nabla^2\phi_0 + \frac{1}{3}G\nabla h\cdot\nabla\left(G\nabla^2\phi_0\right)\right.\\ &+ \left.\left.\frac{1}{6}G\nabla^2\left(G\nabla h\cdot\nabla\phi_0\right)\right]\zeta^3 + \frac{1}{24}G\nabla^2\left(G\nabla^2\phi_0\right)\zeta^4\right\} \qquad (2.11)\end{aligned}$$

Commensurate with the extension of the velocity potential to $O(\mu^4)$, we seek to derive a set of model equations having a corresponding dispersion relationship in the form of a (4,4) Padé approximant (Witting, 1984) representing the approximation

$$\frac{\tanh\mu}{\mu} \approx \frac{1+(1/9)\mu^2+(1/945)\mu^4}{1+(4/9)\mu^2+(1/63)\mu^4} + O(\mu^6). \qquad (2.12)$$

For the case of approximations retaining terms to $O(\mu^2)$, the goal of obtaining the corresponding (2,2) Padé approximant is achieved by redefining the velocity potential in terms of the value of the potential at an elevation $z_\alpha = h[(1+2\alpha)^{1/2}-1]; \alpha =$

$-2/5$ and using the resulting reference value $\phi_\alpha = \phi(z_\alpha)$ as the dependent variable; see Nwogu (1993), Chen and Liu (1995) and Kirby (1997). This procedure is not adequate for a (4,4) Padé approximant, as shown in Appendix A. Instead, we define a new dependent variable

$$\tilde{\phi} = \beta\phi_a + (1-\beta)\phi_b \tag{2.13}$$

where ϕ_a and ϕ_b are the velocity potentials at elevations $z = z_a$ and $z = z_b$, and β is a weight parameter. Relationships between these parameters to give the appropriate dispersion relationship will be presented in Chapter 3. $\tilde{\phi}$ may be written in terms of ϕ_0 using (2.11) yielding:

$$\begin{aligned}
\tilde{\phi} &= \phi_0 - \mu^2\left(AhG\nabla h\cdot\nabla\phi_0 + \frac{1}{2}Bh^2G\nabla^2\phi_0\right) \\
&+ \mu^4\left\{Bh^2\left[\frac{1}{2}G^2\nabla^2 h\nabla h\cdot\nabla\phi_0 + G\nabla h\cdot\nabla\left(G\nabla h\cdot\nabla\phi_0\right)\right]\right. \\
&+ Ch^3\left[\frac{1}{6}G^2\nabla^2 h\nabla^2\phi_0 + \frac{1}{3}G\nabla h\cdot\nabla\left(G\nabla^2\phi_0\right)\right. \\
&+ \left.\left.\frac{1}{6}G\nabla^2\left(G\nabla h\cdot\nabla\phi_0\right)\right] + \frac{1}{24}Dh^4G\nabla^2\left(G\nabla^2\phi_0\right)\right\},
\end{aligned} \tag{2.14}$$

where

$$A \equiv \frac{1}{h}\left[\beta(h+z_a) + (1-\beta)(h+z_b)\right] \tag{2.15}$$

$$B \equiv \frac{1}{h^2}\left[\beta(h+z_a)^2 + (1-\beta)(h+z_b)^2\right] \tag{2.16}$$

$$C \equiv \frac{1}{h^3}\left[\beta(h+z_a)^3 + (1-\beta)(h+z_b)^3\right] \tag{2.17}$$

$$D \equiv \frac{1}{h^4}\left[\beta(h+z_a)^4 + (1-\beta)(h+z_b)^4\right] \tag{2.18}$$

Inverting (2.14) gives a formula for ϕ_0 in terms of $\tilde{\phi}$ which is substituted into (2.11), leading to an approximation to the full velocity potential in terms of $\tilde{\phi}$:

$$\begin{aligned}
\phi &= \tilde{\phi} + \mu^2\left[\left(Ah-\zeta\right)F_1(\tilde{\phi}) + \left(Bh^2-\zeta^2\right)F_2(\tilde{\phi})\right] + \mu^4\left[\left(Ah-\zeta\right)F_3(\tilde{\phi})\right. \\
&+ \left.\left(Bh^2-\zeta^2\right)F_4(\tilde{\phi}) + \left(Ch^3-\zeta^3\right)F_5(\tilde{\phi}) + \left(Dh^4-\zeta^4\right)F_6(\tilde{\phi})\right],
\end{aligned} \tag{2.19}$$

where

$$\begin{aligned}
F_1(\tilde{\phi}) &\equiv G\nabla h\cdot\nabla\tilde{\phi}\\
F_2(\tilde{\phi}) &\equiv \frac{1}{2}G\nabla^2\tilde{\phi}\\
F_3(\tilde{\phi}) &\equiv \nabla h\cdot\nabla\left(Ah\nabla h\cdot\nabla\tilde{\phi}\right)+\frac{1}{2}\nabla h\cdot\nabla\left(Bh^2\nabla^2\tilde{\phi}\right)\\
F_4(\tilde{\phi}) &\equiv \frac{1}{2}\nabla^2\left(Ah\nabla h\cdot\nabla\tilde{\phi}\right)+\frac{1}{4}\nabla^2\left(Bh^2\nabla^2\tilde{\phi}\right)\\
&- \frac{1}{2}^2\nabla^2 h\nabla h\cdot\nabla\tilde{\phi}-\nabla h\cdot\nabla\left(\nabla h\cdot\nabla\tilde{\phi}\right)\\
F_5(\tilde{\phi}) &\equiv -\frac{1}{6}\nabla^2 h\nabla^2\tilde{\phi}-\frac{1}{3}\nabla h\cdot\nabla\left(\nabla^2\tilde{\phi}\right)-\frac{1}{6}\nabla^2\left(\nabla h\cdot\nabla\tilde{\phi}\right)\\
F_6(\tilde{\phi}) &\equiv -\frac{1}{24}\nabla^2\left(\nabla^2\tilde{\phi}\right).
\end{aligned}\tag{2.20}$$

By substituting (2.19) into (2.6), and neglecting terms of $O(\mu^6)$ and higher, we obtain the approximate conservation of mass equation:

$$\eta_t=-\nabla\cdot\mathbf{M},\tag{2.21}$$

where

$$\begin{aligned}
\mathbf{M} &= H\nabla\tilde{\phi}+\mu^2H\left\{\left[(A-1)F_1(\tilde{\phi})+2\left(Bh-\frac{H}{2}\right)F_2(\tilde{\phi})\right]\nabla h\right.\\
&+ \left.\left(Ah-\frac{H}{2}\right)\nabla F_1(\tilde{\phi})+\left(Bh^2-\frac{H^2}{3}\right)\nabla F_2(\tilde{\phi})\right\}\\
&+ \mu^4H\left\{\left[(A-1)F_3(\tilde{\phi})+2\left(Bh-\frac{H}{2}\right)F_4(\tilde{\phi})\right.\right.\\
&+ \left.3\left(Ch^2-\frac{H^2}{3}\right)F_5(\tilde{\phi})+4\left(Dh^3-\frac{H^3}{4}\right)F_6(\tilde{\phi})\right]\nabla h\\
&+ \left(Ah-\frac{H}{2}\right)\nabla F_3(\tilde{\phi})+\left(Bh^2-\frac{H^2}{3}\right)\nabla F_4(\tilde{\phi})\\
&+ \left.\left(Ch^3-\frac{H^3}{4}\right)\nabla F_5(\tilde{\phi})+\left(Dh^4-\frac{H^4}{5}\right)\nabla F_6(\tilde{\phi})\right\},
\end{aligned}\tag{2.22}$$

and $H = h + \delta\eta$. Substituting (2.19) into (2.4) and neglecting terms of $O(\mu^6)$ and higher, we obtain the approximate Bernoulli equation evaluated at $z = \delta\eta$:

$$\begin{aligned}
\eta \;+\; & \tilde{\phi}_t + \mu^2\left[(Ah - H)\,F_1(\tilde{\phi}_t) + \left(Bh^2 - H^2\right)F_2(\tilde{\phi}_t)\right] \\
+\; & \mu^4\left[(Ah - H)\,F_3(\tilde{\phi}_t) + \left(Bh^2 - H^2\right)F_4(\tilde{\phi}_t)\right. \\
+\; & \left.\left(Ch^3 - H^3\right)F_5(\phi_t) + \left(Dh^4 - H^4\right)F_6(\tilde{\phi}_t)\right] \\
+\; & \frac{\delta}{2}\left\{\left|\nabla\tilde{\phi}\right|^2 + 2\nabla\tilde{\phi}\cdot\nabla\left[\mu^2\left\{(Ah - H)\,F_1(\tilde{\phi}) + \left(Bh^2 - H^2\right)F_2(\tilde{\phi})\right\}\right.\right. \\
+\; & \mu^4\left\{(Ah - H)\,F_3(\tilde{\phi}) + \left(Bh^2 - H^2\right)F_4(\tilde{\phi}) + \left(Ch^3 - H^3\right)F_5(\tilde{\phi})\right. \\
+\; & \left.\left.\left(Dh^4 - H^4\right)F_6(\tilde{\phi})\right\}\right. \\
+\; & \mu^4\left|\nabla\left\{(Ah - H)\,F_1(\tilde{\phi}) + \left(Bh^2 - H^2\right)F_2(\tilde{\phi})\right\}\right|^2 \\
+\; & \mu^2\left[F_1(\tilde{\phi}) + 2F_2(\tilde{\phi})\right]^2 + 2\mu^4\left[F_3(\tilde{\phi}) + 2HF_4(\tilde{\phi}) + 3H^2F_5(\tilde{\phi})\right. \\
+\; & \left.4H^3F_6(\tilde{\phi})\right]\left[F_1(\tilde{\phi}) + 2HF_2(\tilde{\phi})\right] = 0. \qquad (2.23)
\end{aligned}$$

The pair of equations (2.22) and (2.23) form a fully nonlinear Boussinesq-type model based on a velocity potential-type variable, $\tilde{\phi}$. We now define a velocity-type vector:

$$\tilde{\mathbf{u}}(x, y, t) = \beta\left[\nabla\phi\right]_{z=z_a} + (1 - \beta)\left[\nabla\phi\right]_{z=z_b}. \qquad (2.24)$$

The relationship between $\tilde{\mathbf{u}}$ and $\tilde{\phi}$ can be found by inverting the gradient of (2.19) and substituting into (2.24), and is given by

$$\begin{aligned}
\nabla\tilde{\phi} \;=\; & \tilde{\mathbf{u}} - \mu^2\nabla h\left[(A - 1)\,F_{21} + 2\,(B - A)\,hF_{22}\right] \\
-\; & \mu^4\nabla h\left[(A - 1)\,(F_{41} + F_{43}) + 2\,(B - A)\,h\,(F_{42} + F_{44})\right. \\
+\; & \left.3\,(C - B)\,h^2F_{45} + 4\,(D - C)\,h^3F_{46}\right], \qquad (2.25)
\end{aligned}$$

where

$$F_{21}(\tilde{\mathbf{u}}) \;\equiv\; G\nabla h\cdot\tilde{\mathbf{u}}$$

$$
\begin{aligned}
F_{22}(\tilde{\mathbf{u}}) &\equiv \frac{1}{2}G\nabla\cdot\tilde{\mathbf{u}} \\
F_{41}(\tilde{\mathbf{u}}) &\equiv -|\nabla h|^2\left[(A-1)\nabla h\cdot\tilde{\mathbf{u}}+(B-A)h\nabla\cdot\tilde{\mathbf{u}}\right] \\
F_{42}(\tilde{\mathbf{u}}) &\equiv -\frac{1}{2}\nabla^2 h\left[(A-1)\nabla h\cdot\tilde{\mathbf{u}}+(B-A)h\nabla\cdot\tilde{\mathbf{u}}\right] \\
F_{43}(\tilde{\mathbf{u}}) &\equiv \nabla h\cdot\nabla\left(Ah\nabla h\cdot\tilde{\mathbf{u}}\right)+\frac{1}{2}\nabla h\cdot\nabla\left(Bh^2\nabla\cdot\tilde{\mathbf{u}}\right) \\
F_{44}(\tilde{\mathbf{u}}) &\equiv \frac{1}{2}\nabla^2\left(Ah\nabla h\cdot\tilde{\mathbf{u}}\right)+\frac{1}{4}\nabla^2\left(Bh^2\nabla\cdot\tilde{\mathbf{u}}\right) \\
&- \frac{1}{2}\nabla^2 h\nabla h\cdot\tilde{\mathbf{u}}-\nabla h\cdot\nabla\left(\nabla h\cdot\tilde{\mathbf{u}}\right) \\
F_{45}(\tilde{\mathbf{u}}) &\equiv -\frac{1}{6}\nabla^2 h\nabla\cdot\tilde{\mathbf{u}}-\frac{1}{3}\nabla h\cdot\nabla\left(\nabla\cdot\tilde{\mathbf{u}}\right)-\frac{1}{6}\nabla^2\left(\nabla h\cdot\tilde{\mathbf{u}}\right) \\
F_{46}(\tilde{\mathbf{u}}) &\equiv -\frac{1}{24}\nabla^2\left(\nabla\cdot\tilde{\mathbf{u}}\right). \qquad (2.26)
\end{aligned}
$$

Now we substitute (2.25) into the expression (2.22) for $\mathbf{M}$, and into the gradient of the Bernoulli equation (2.23). The resulting set of evolution equations are the approximate conservation laws using the velocity-type variable $\tilde{\mathbf{u}}$, and is given by (2.21) with:

$$
\begin{aligned}
\mathbf{M} &= H\left\{\tilde{\mathbf{u}}+\mu^2\left[\left(Ah-\frac{H}{2}\right)\left(2\nabla hF_{22}+\nabla F_{21}\right)+\left(Bh^2-\frac{H^2}{3}\right)\nabla F_{22}\right]\right. \\
&+ \mu^4\left[\left(Ah-\frac{H}{2}\right)\left(2\nabla hF_{42}+\nabla F_{41}+2\nabla hF_{44}+\nabla F_{43}\right)\right. \\
&+ \left(Bh^2-\frac{H^2}{3}\right)\left(\nabla F_{42}+3\nabla hF_{45}+\nabla F_{44}\right) \\
&+ \left.\left.\left(Ch^3-\frac{H^3}{4}\right)\left(4\nabla hF_{46}+\nabla F_{45}\right)+\left(Dh^4-\frac{H^4}{5}\right)\nabla F_{46}\right]\right\}, \qquad (2.27)
\end{aligned}
$$

for mass conservation, and

$$
\mathbf{U}_t=-\nabla\eta-\frac{\delta}{2}\nabla\left(|\tilde{\mathbf{u}}|^2\right)+\Gamma_1\left(\eta,\tilde{\mathbf{u}}_t\right)+\Gamma_2\left(\eta,\tilde{\mathbf{u}}\right), \qquad (2.28)
$$

for momentum conservation. $\mathbf{U}$, Γ_1, and Γ_2 are given by

$$
\mathbf{U} \equiv \tilde{\mathbf{u}}+\mu^2\left[(A-1)h\left(2\nabla hF_{22}+\nabla F_{21}\right)+(B-1)h^2\nabla F_{22}\right]
$$

$$
\begin{aligned}
&+ \quad \mu^4 \left[(A-1)\, h \left(2\nabla h F_{42} + \nabla F_{41} + 2\nabla h F_{44} + \nabla F_{43} \right) \right. \\
&+ \quad (B-1)\, h^2 \left(\nabla F_{42} + 3\nabla h F_{45} + \nabla F_{44} \right) \\
&+ \quad \left. (C-1)\, h^3 \left(4\nabla h F_{46} + \nabla F_{45} \right) + (D-1)\, h^4 \nabla F_{46} \right] \qquad (2.29) \\
\Gamma_1 \quad &\equiv \quad \mu^2 \nabla \left[\eta F_{21t} + \left(2h\eta + \eta^2 \right) F_{22t} \right] \\
&+ \quad \mu^4 \nabla \left[\eta \left(F_{41t} + F_{43t} \right) + \left(2h\eta + \eta^2 \right) \left(F_{42t} + F_{44t} \right) \right. \\
&+ \quad \left. \left(3h^2\eta + 3h\eta^2 + \eta^3 \right) F_{45t} + \left(4h^3\eta + 6h^2\eta^2 + 4h\eta^3 + \eta^4 \right) F_{45t} \right] \qquad (2.30) \\
\Gamma_2 \quad &\equiv - \quad \mu^2 \delta \nabla \left\{ \tilde{\mathbf{u}} \cdot \left[(Ah - H) \left(\nabla F_{21} + 2\nabla h F_{22} \right) + \left(Bh^2 - H^2 \right) \nabla F_{22} \right] \right. \\
&+ \quad \left. \frac{1}{2} \left(F_{21} + 2H F_{22} \right)^2 \right\} \\
&- \quad \mu^4 \delta \nabla \left\{ \tilde{\mathbf{u}} \cdot \left[(Ah - H) \left(\nabla F_{41} + 2\nabla h F_{42} + \nabla F_{43} + 2\nabla h F_{44} \right) \right. \right. \\
&+ \quad \left(Bh^2 - H^2 \right) \left(\nabla F_{42} + \nabla F_{44} + 3\nabla h F_{45} \right) \\
&+ \quad \left. \left(Ch^3 - H^3 \right) \left(\nabla F_{45} + 4\nabla h F_{46} \right) + \left(Dh^4 - H^4 \right) \nabla F_{46} \right] \\
&+ \quad \frac{1}{2} \left| (Ah - H) \right) \left(\nabla F_{21} + 2\nabla h F_{22} \right) + \left(Bh^2 - H^2 \right) \nabla F_{42} \Big|^2 \\
&+ \quad \frac{1}{2} \left[\left(F_{21} + 2H F_{22} \right) \left(F_{41} + 2H F_{42} \right. \right. \\
&+ \quad \left. \left. F_{43} + 2H F_{44} + 3H^2 F_{45} + 4H^3 F_{46} \right) \right] \Big\} \qquad (2.31)
\end{aligned}
$$

Once $\tilde{\mathbf{u}}$ is known, the actual velocity field can be computed from substituting (2.25) into the gradient of (2.19):

$$
\begin{aligned}
(u, v) \quad &= \quad \tilde{\mathbf{u}} + \mu^2 \left[(Ah - \zeta) \left(\nabla F_{21} + 2\nabla h F_{22} \right) + \left(Bh^2 - \zeta^2 \right) \nabla F_{22} \right] \\
&+ \quad \mu^4 \left[(Ah - \zeta) \left(\nabla F_{41} + 2\nabla h F_{42} + \nabla F_{43} + 2\nabla h F_{44} \right) \right. \\
&+ \quad \left(Bh^2 - \zeta^2 \right) \left(\nabla F_{42} + \nabla F_{44} + 3\nabla h F_{45} \right) \\
&+ \quad \left. \left(Ch^3 - \zeta^3 \right) \left(\nabla F_{45} + 4\nabla h F_{46} \right) + \left(Dh^4 - \zeta^4 \right) \nabla F_{46} \right] \qquad (2.32) \\
w \quad &= \quad -\mu^2 \left[F_{21} + 2\zeta F_{22} \right] - \mu^4 \left[F_{41} + F_{43} \right. \\
&+ \quad \left. 2\zeta \left(F_{42} + F_{44} \right) + 3\zeta^2 F_{45} + 4\zeta^3 F_{46} \right]. \qquad (2.33)
\end{aligned}
$$

The free parameters β, z_a, and z_b will be considered in Chapter 3, when we study

the dispersion properties of the model. To obtain a set of $O(\mu^4)$ weakly dispersive, weakly nonlinear equations with $O(\delta) = O(\mu^2)$, terms of $O(\delta^2\mu^2, \delta^3\mu^2, \delta\mu^4, \delta^2\mu^4, \delta^3\mu^4, \delta^4\mu^4, \delta^5\mu^4)$ should be neglected. The assumption $O(\delta) = O(\mu^2)$ is used in the standard Boussinesq model. To recover the WKGS model, one must neglect $O(\mu^4)$ terms while keeping all terms proportional to powers of δ, and setting $\beta = 1$, and with Nwogu's α_N being related to A and B by

$$\begin{aligned} A &= \sqrt{B} \\ B &= 2\alpha_N + 1 \end{aligned} \tag{2.34}$$

and $\tilde{u}$ being replaced by WKGS's u_α.

Equations (2.21) with (2.27), and (2.28) form the 2-dimensional version of the $O(\mu^4)$ fully nonlinear model . A one-dimensional version in x can be obtained by assuming $\tilde{\mathbf{u}} \equiv \tilde{u}$, and $\nabla \equiv \partial/\partial x$. We, hereafter, shall refer to the $O(\mu^4)$ fully nonlinear model as FN4 and the $O(\mu^4)$ weakly nonlinear model as WN4.

Chapter 3

ANALYTICAL PROPERTIES

3.1 Linear Properties

In this section we consider the flat bottom linearized version of the model governing η and $\tilde{\phi}$ derived in Chapter 2, and analyze several linear properties of the model.

3.1.1 Dispersion

Neglecting all terms containing δ and assuming a flat bottom ($h = h_0 = 1$) in (2.22) and (2.23) we have the following linear equations. Mass conservation:

$$\begin{aligned} \eta_t &+ \nabla^2\tilde{\phi} + \frac{\mu^2}{2}\left(B - \frac{1}{3}\right)\nabla^2\nabla^2\tilde{\phi} \\ &+ \frac{\mu^4}{4}\left(B^2 - \frac{B}{3} - \frac{D}{6} + \frac{1}{30}\right)\nabla^2\nabla^2\nabla^2\tilde{\phi} = 0 \end{aligned} \tag{3.1}$$

Bernoulli equation:

$$\begin{aligned} \eta &+ \tilde{\phi}_t + \frac{\mu^2}{2}(B-1)\nabla^2\tilde{\phi}_t \\ &+ \frac{\mu^4}{4}\left(B^2 - B - \frac{D}{6} + \frac{1}{6}\right)\nabla^2\nabla^2\tilde{\phi}_t = 0 \end{aligned} \tag{3.2}$$

To analyze the dispersion properties of these equations, we assume the following general solution to the equations:

$$\eta = ae^{i(\mathbf{x}-\omega t)} \qquad \tilde{\phi} = be^{i(\mathbf{x}-\omega t)} \tag{3.3}$$

where ω is the angular frequency nondimensionalized by $k_0(gh_0)^{1/2}$, a and b are amplitudes, and $i = \sqrt{-1}$. Substituting (3.3) into (3.1) and (3.2) we obtain the linear dispersion relationship for the model:

$$\omega^2 = \frac{1 - \frac{1}{2}\left(B - \frac{1}{3}\right)\mu^2 + \frac{1}{4}\left(B^2 - \frac{B}{3} - \frac{D}{6} + \frac{1}{30}\right)\mu^4}{1 - \frac{1}{2}(B-1)\mu^2 + \frac{1}{4}\left(B^2 - B - \frac{D}{6} + \frac{1}{6}\right)\mu^4} \tag{3.4}$$

The expression (3.4) resembles the remarkably good (4,4) Padé approximant to the exact linear dispersion relationship $\omega^2 = \tanh\mu/\mu$ (Witting, 1984). For (3.4) to be the (4,4) Padé approximant, we set $B = 1/9$ and $D = 5/189$, and solve (2.16) and (2.18) for parameters β, z_a, and z_b. Since we have 3 unknowns and 2 equations, there are an infinite number of solutions that give the desired values of B and D. However, an arbitrary choice of β can give imaginary values of z_a or z_b or values lying outside of the fluid domain, causing these parameters to lack physical significance. The relationship between β, z_a, and z_b for a (4,4) Padé approximant is as follows:

$$\begin{aligned} z_a &= \left[\frac{1}{9} - \left\{\frac{8\beta}{567(1-\beta)}\right\}^{1/2} + \left\{\frac{8}{567\beta(1-\beta)}\right\}^{1/2}\right]^{1/2} - 1 \\ z_b &= \left[\frac{1}{9} - \left\{\frac{8\beta}{567(1-\beta)}\right\}^{1/2}\right]^{1/2} - 1 \end{aligned} \tag{3.5}$$

Figure 3.1 shows a plot of the real part of z_a and z_b as given by (3.5). Notice that values of β between 0.018 and 0.467 will give both z_a and z_b to be real values lying inside the water column. The remaining free parameter can be chosen to improve

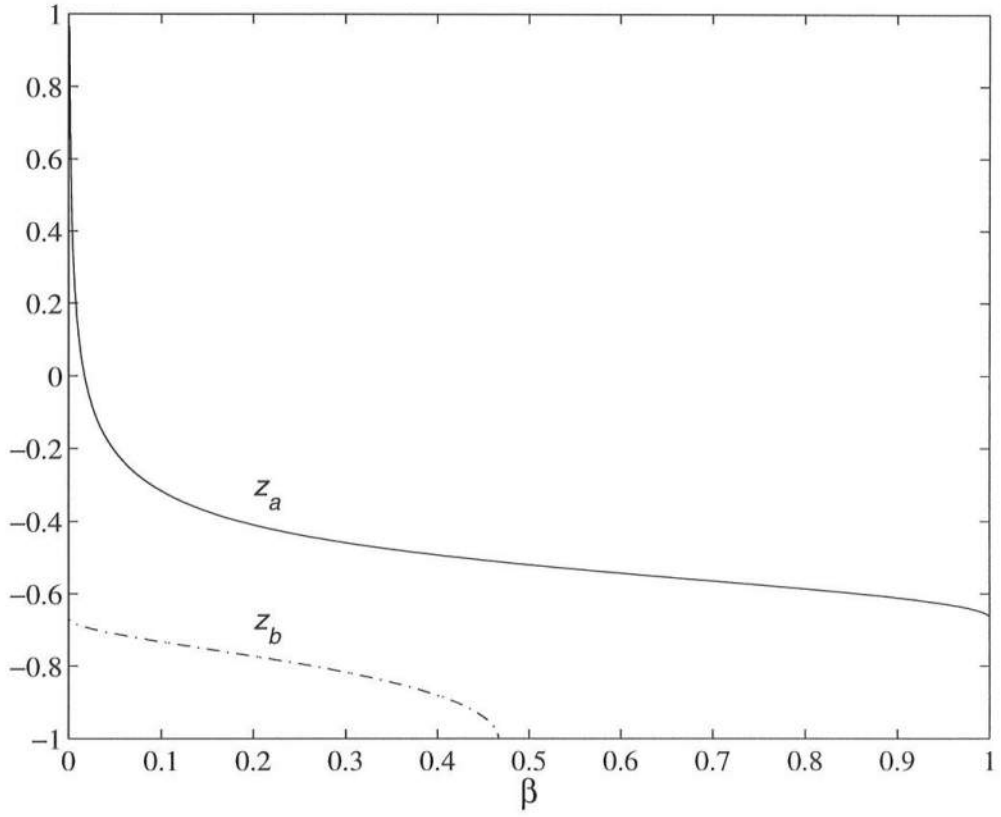

Figure 3.1: Values of $z_a(\beta)$ (solid), $z_b(\beta)$ (dash-dot) as a function of weighting factor β, corresponding to the (4,4) Padé approximant dispersion relation.

depth dependent properties such as linear shoaling. This has not been done in the present work, where we arbitrarily set $\beta = 0.2$, and substitute this value into (3.5) to obtain $z_a = -0.4095$ and $z_b = -0.7726$.

Figure 3.2 shows comparison between the standard Boussinesq theory (depth averaged velocity), Nwogu's formulation, and present model with (4,4) Padé approximant dispersion relationship, of the ratio of the phase speed with Airy's exact linear solution. It is clear that the present model has improved linear dispersion

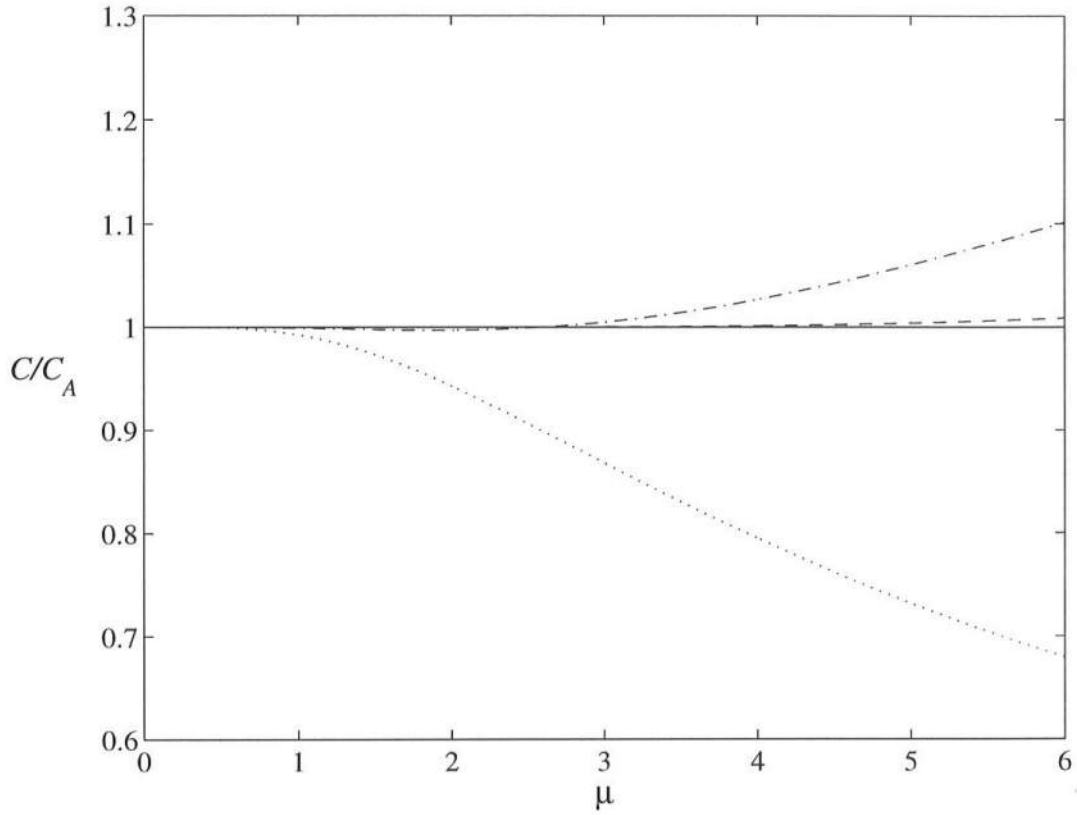

Figure 3.2: Ratio of phase speed with Airy's exact linear solution. Standard Boussinesq (dot), Nwogu's (2,2) Padé (dash-dot), Present (4,4) Padé (dash).

properties over the already accurate Nwogu's model and closely reproduces the exact solution through intermediate to deep water. Similarly, the linear group velocity, defined as $C_g = \partial\omega/\partial k$ is shown in Figure 3.3 and the improvement over Nwogu's model is even more evident.

Alternatively to the (4,4) Padé approximant, one could compute values for β, z_a, and z_b to minimize the errors in the linear phase speed and group velocity over some depth range. This was the procedure used by Nwogu to obtain his

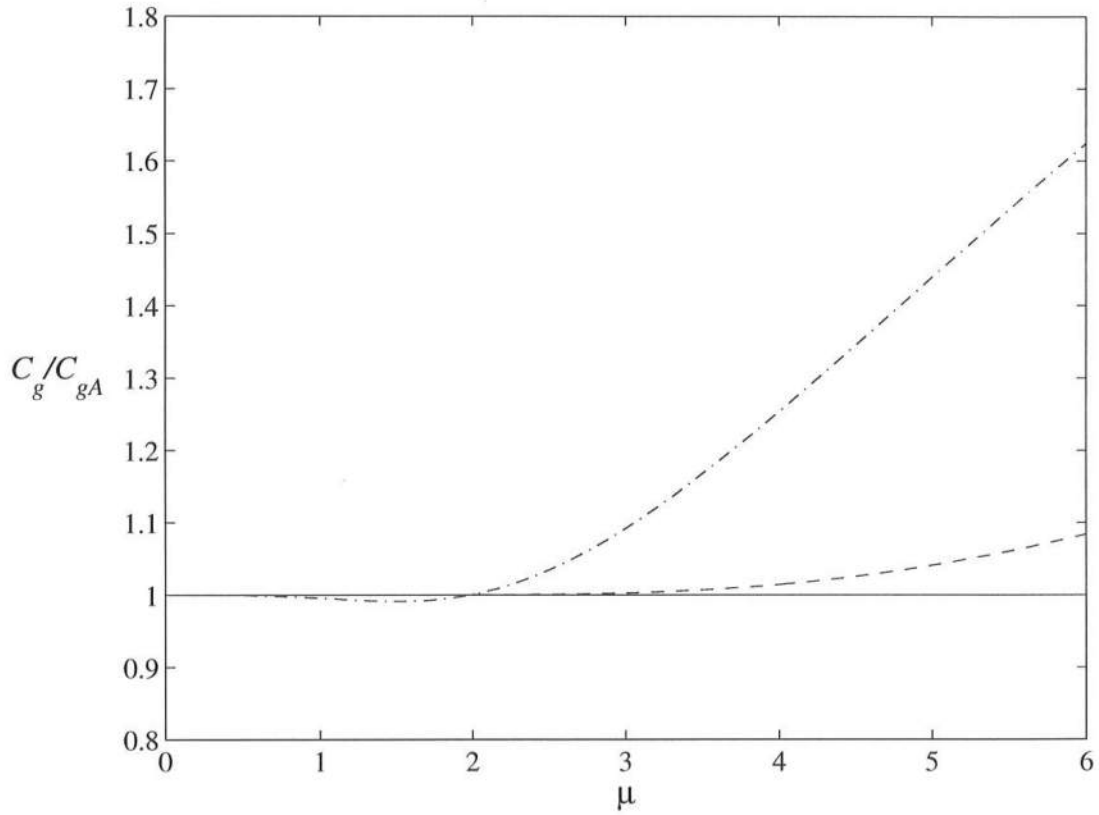

Figure 3.3: Ratio of linear group velocity to Airy's exact linear solution. Nwogu (dash-dot), Present (dash).

optimized parameter $\alpha = -0.39$. However, the authors found that the (4,4) Padé approximant is already sufficiently accurate for any practical purposes, and any parameter optimization over a normal water depth range would result in minor improvement.

3.1.2 Internal Kinematics

The internal kinematics of the present model can be obtained from (2.19). For the sake of comparison with the exact linear solution, we assume flat bottom with $h = 1$ and the linear theory solution $\tilde{\phi} = e^{x-\omega t}$. The flat bottom one-dimensional version of (2.19) is:

$$\begin{aligned} \phi &= \tilde{\phi} + \frac{1}{2}\mu^2 (B - \zeta)\, \tilde{\phi}_{xx} \\ &+ \frac{1}{4}\mu^2 \left(B^2 - B\zeta^2 - \frac{1}{6}D + \zeta^4 \right) \tilde{\phi}_{xxxx} \end{aligned} \tag{3.6}$$

We define a function $f_1(z)$ as the velocity potential given by (3.6) normalized by its value at position $z = 0$, which is used as a common reference:

$$f_1(z) = \frac{1 - \frac{\mu^2}{2}\left[B - (1+z)^2\right] + \frac{\mu^4}{4}\left[B^2 - B(1+z)^2 - \frac{D}{6} + \frac{(1+z)^4}{6}\right]}{1 - \frac{\mu^2}{2}\left[B - 1\right] + \frac{\mu^4}{4}\left[B^2 - B - \frac{D}{6} + \frac{1}{6}\right]} \tag{3.7}$$

The vertical velocity component w can be obtained by differentiating (3.6) with respect to z. Similarly to f_1, a vertical velocity profile function can be obtained by defining $f_2(z) = w(z)/w(0)$:

$$f_2(z) = \frac{\mu^2\left[(1+z)\right] + \frac{\mu^4}{2}\left[-B(1+z) + \frac{(1+z)^3}{3}\right]}{\mu^2 + \frac{\mu^4}{2}\left[-B + \frac{1}{3}\right]} \tag{3.8}$$

Figure 3.4 shows comparisons of $f_1(z)$ between the exact linear solution given by $\cosh[\mu(1+z)]/\cosh[\mu]$, Nwogu's model and the present model, for various values of

relative water depth μ. Notice that for moderately shallow water, the two models reproduce the exact solution quite well; as μ increases, Nwogu's model starts to deviate strongly, developing a reverse flow pattern near the bottom at $\mu \approx 3$, while the present model remains very accurate. Only at quite deep water the present model starts to deviate considerably from the exact solution developing an inflection point at $\mu \approx 4.24$ and a reverse flow at $\mu \approx 6.07$.

Figure 3.5 shows results similar to Figure 3.4 for $f_2(z)$. The equivalent exact linear solution is $\mu \sinh[\mu(1+z)]/\cosh[\mu]$. Notice that Nwogu's model has a linear vertical profile for w, a poor representation in intermediate to deep water. The present model stays close to the exact solution for a wide range of μ. A reverse vertical flow starts to appear at $\mu \approx 6.07$, where the horizontal flow develops the inflection point. Finally, Figure 3.6 shows the ratio to the exact linear solution $f_{3A} = \mu \tanh(\mu)$ of the ratio between vertical and horizontal velocities ϕ_z/ϕ_x at $z = 0$, $f_3(\mu)$, for the present model, and Nwogu's model. The expression for f_3 can be obtained by dividing the numerator of (3.8) by the numerator of (3.7):

$$f_3(\mu) = \frac{w(z=0)}{u(z=0)} = \frac{\mu^2 + \frac{\mu^4}{2}\left[-B + \frac{1}{3}\right]}{1 - \frac{\mu^2}{2}\left[B - 1\right] + \frac{\mu^4}{4}\left[B^2 - B - \frac{D}{6} + \frac{1}{6}\right]} \tag{3.9}$$

The present model agrees better with the exact linear solution than Nwogu's model for a wide depth range.

3.2 Nonlinear Properties

In the previous sections we have seen that the proposed model has excellent linear dispersion properties as well as greatly improved representation of the internal flow kinematics. It is useful to analyze some of the nonlinear properties of the model by using analytical tools such as Stokes' type asymptotic expansions

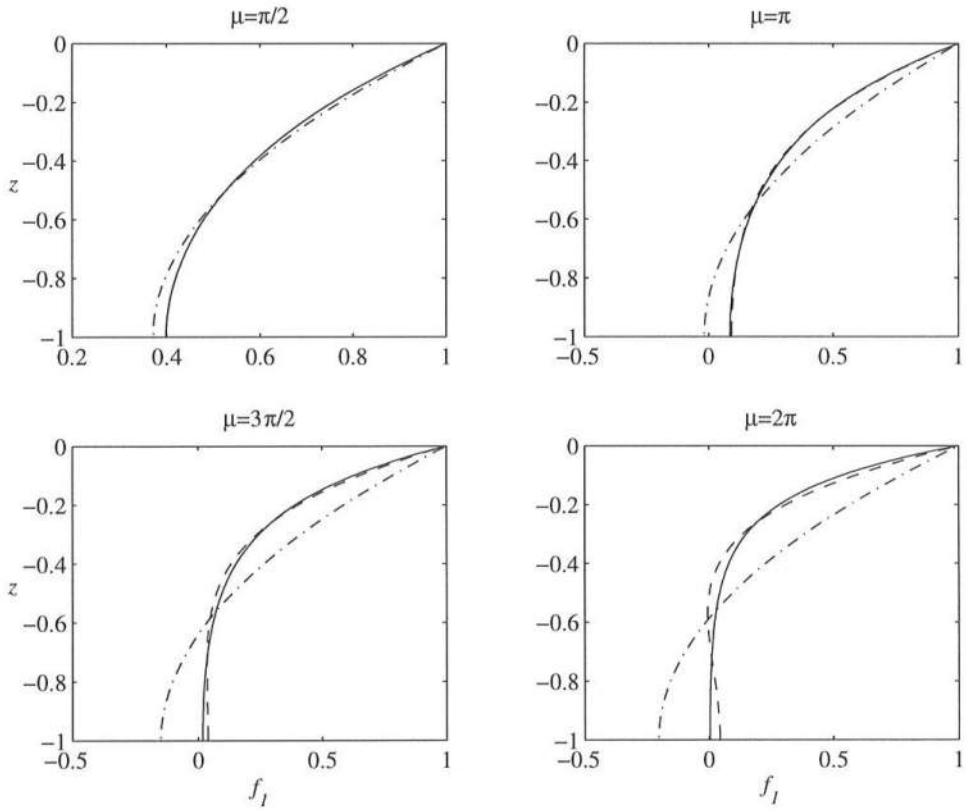

Figure 3.4: Normalized vertical profile of linear horizontal velocity for several values of μ. Exact (solid), Nwogu (dash-dot), Present (dash).

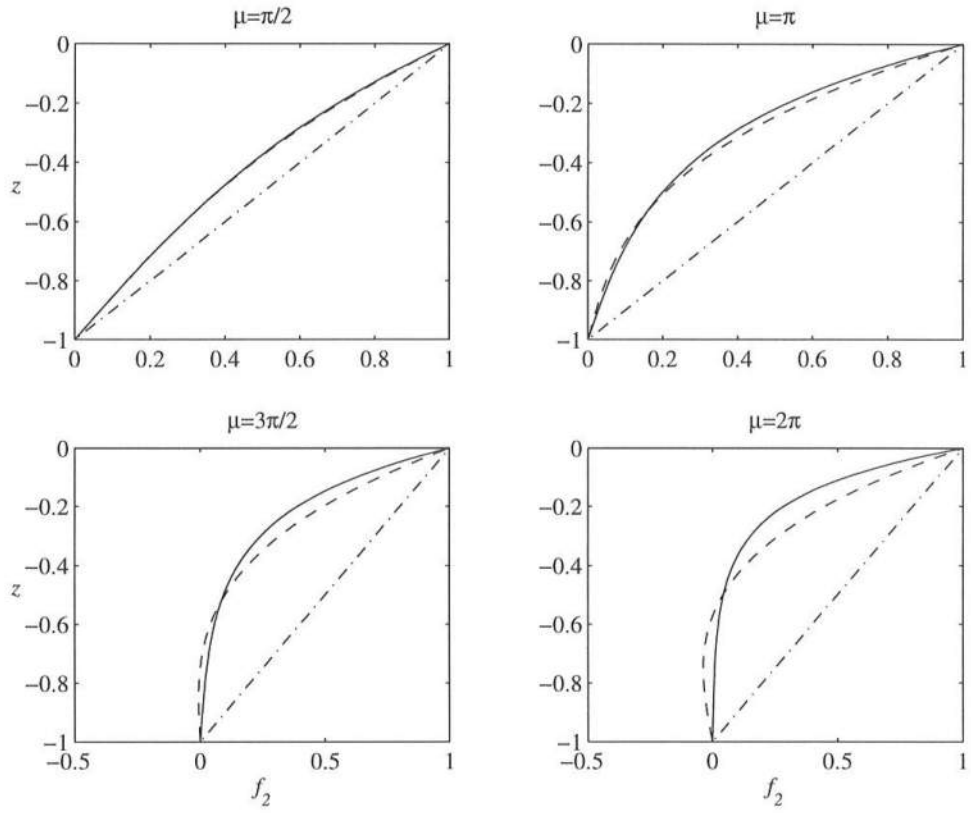

Figure 3.5: Normalized vertical profile of linear vertical velocity for several values of μ. Exact (solid), Nwogu (dash-dot), Present (dash).

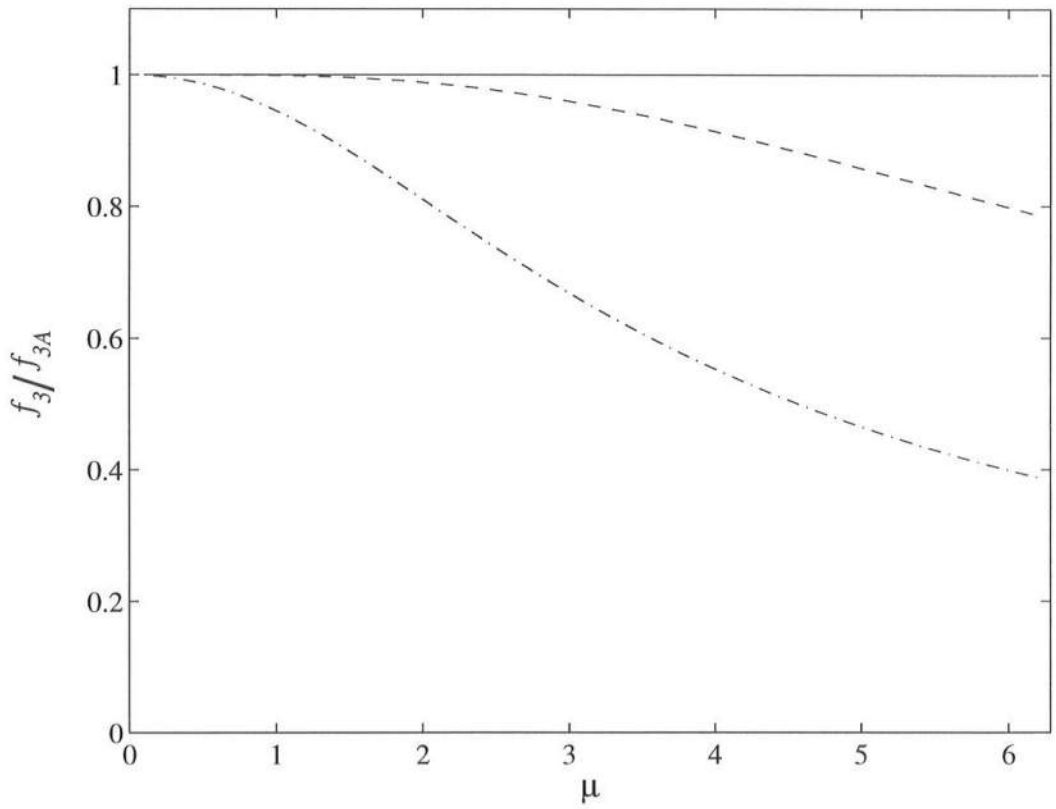

Figure 3.6: Ratio of approximate results for $w(0)/u(0)$ to the exact linear solution. Nwogu (dash-dot), Present solution (dash).

and multiple scales expansions, and, since these types of analysis have been extensively applied and studied for the full boundary value potential problem, we can have an idea of how well the nonlinear version of the present model would perform by comparing some of its nonlinear properties with those of the full problem, and also with WKGS and Nwogu's model, keeping in mind that a numerical implementation of WKGS model has already been tested with a good degree of success.

In the following sections we investigate $O(\delta)$ nonlinear interactions in a random sea, and $O(\delta^2)$ evolution of a narrow banded spectrum wave train, governed by Schrödinger equation.

The constant depth versions of the evolution equations for $\tilde{\phi}$ and η are:

$$\begin{aligned}
\eta_t &+ \nabla\cdot\left\{H\left[\nabla\tilde{\phi}+\frac{\mu^2}{2}\left(B-\frac{1}{3}H^2\right)\nabla\nabla^2\tilde{\phi}\right.\right.\\
&+ \left.\left.\frac{\mu^4}{4}\left(B^2-\frac{1}{6}D-\frac{1}{3}BH^2+\frac{1}{30}H^4\right)\nabla\nabla^2\nabla^2\tilde{\phi}\right]\right\}=0 \qquad (3.10)\\
\eta &+ \tilde{\phi}_t+\frac{1}{2}\left|\nabla\tilde{\phi}\right|^2+\frac{\mu^2}{2}\left(B-H^2\right)\nabla^2\tilde{\phi}_t\\
&+ \frac{\mu^4}{4}\left(B^2-\frac{1}{6}D-BH^2+\frac{1}{6}H^4\right)\nabla^2\nabla^2\tilde{\phi}_t\\
&+ \nabla\tilde{\phi}\cdot\nabla\left[\frac{\mu^2}{2}\left(B-H^2\right)\nabla^2\tilde{\phi}\right.\\
&+ \left.\frac{\mu^4}{4}\left(B^2-\frac{1}{6}D-BH^2+\frac{1}{6}H^4\right)\nabla^2\nabla^2\tilde{\phi}\right]\\
&+ \frac{\mu^4}{8}\nabla\left|\left(B-H^2\right)^2\left(\nabla^2\tilde{\phi}\right)\right|^2+\frac{\mu^2}{2}H^2\left(\nabla^2\tilde{\phi}\right)^2\\
&+ \frac{\mu^4}{4}\left(BH^2-\frac{1}{3}H^4\right)\nabla^2\tilde{\phi}\nabla^2\nabla^2\tilde{\phi}=0 \qquad (3.11)
\end{aligned}$$

3.2.1 Second Order Interactions in Random Sea

We will now look at generation of super and sub-harmonics by second order Stokes-type interactions. It is well known that in intermediate and deep water the first nonlinear correction of a linear wave solution is a set of bound waves (waves that are forced by the nonlinear interactions), also called the superharmonics (resulting from sum-wave interactions) and the corresponding subharmonics (resulting from difference-wave interactions) (Hasselmann, 1962). These bound waves are proportional to products of the amplitudes of solutions to the linear equations. The constants of proportionality (which are functions of the local depth) will be referred to as transfer coefficients. Nwogu (1993) has investigated the generation of these bound waves in his extended Boussinesq model and found qualitatively reasonable agreement with Stokes' theory. Madsen and Sørensen (1993) have found similar results. Kirby and Wei (1994) extended Nwogu's model to full nonlinearity and found that the retention of terms proportional to $\delta\mu^2$ (which are neglected in Nwogu's model and the standard Boussinesq model) is essential to a more accurate prediction of the transfer coefficients to the level of accuracy implied by the order of retained dispersive terms in the original model equations. Here, we derive the transfer coefficients for the present model and compare to results from previous models.

We proceed to investigate nonlinear properties of our model by introducing the perturbation expansion:

$$\begin{aligned} \eta &= \eta_0 + \delta\eta_1 + \delta^2\eta_2 \\ \tilde{\phi} &= \phi_0 + \delta\phi_1 + \delta^2\phi_2 \end{aligned} \tag{3.12}$$

into (3.10) and (3.11), and ordering the equations by powers of δ. At each order

$O(\delta^n)$ we obtain:

$$\begin{aligned} \eta_{nt} + L_1\phi_n &= F_n \\ \eta_n + L_2\phi_{nt} &= G_n \end{aligned} \tag{3.13}$$

where L_1 and L_2 are the linear operators:

$$\begin{aligned} L_1 &= \nabla^2 + \frac{\mu^2}{2}\left(B - \frac{1}{3}\right)\nabla^2\nabla^2 \\ &+ \frac{\mu^4}{4}\left(B^2 - \frac{B}{3} - \frac{D}{6} + \frac{1}{30}\right)\nabla^2\nabla^2\nabla^2 \end{aligned} \tag{3.14}$$

$$\begin{aligned} L_2 &= 1 + \frac{\mu^2}{2}(B-1)\nabla^2 \\ &+ \frac{\mu^4}{4}\left(B^2 - B - \frac{D}{6} + \frac{1}{6}\right)\nabla^2\nabla^2 \end{aligned} \tag{3.15}$$

and the forcing terms are given by:

$$\begin{aligned} F_0 &\equiv 0 \\ G_0 &\equiv 0 \\ F_1 &\equiv -\nabla\cdot(\eta_0\nabla\phi_0) - \frac{\mu^2}{2}(B-1)\nabla\cdot\left\{\eta_0\nabla\left(\nabla^2\phi_0\right)\right\} \\ &- \frac{\mu^4}{4}\left(B^2 - B - \frac{D}{6} + \frac{1}{6}\right)\nabla\cdot\left\{\eta_0\nabla\left(\nabla^2\nabla^2\phi_0\right)\right\} \\ G_1 &\equiv -\frac{1}{2}\left(\nabla\phi_0\right)^2 + \frac{\mu^2}{2}\left\{2\eta_0\nabla^2\phi_{0t} - (B-1)\nabla\phi_0\cdot\nabla\left(\nabla^2\phi_0\right) + \left(\nabla^2\phi_0\right)^2\right\} \\ &- \frac{\mu^4}{4}\left\{\left(\frac{2}{3} - 2B\right)\eta_0\nabla^2\nabla^2\eta_{0t} + \left(B^2 - B - \frac{D}{6} + \frac{1}{6}\right)\nabla\phi_0\cdot\nabla\left(\nabla^2\nabla^2\eta_0\right)\right. \\ &+ \left.\frac{1}{2}(B-1)^2\nabla\left(\nabla^2\phi_0\right)\cdot\nabla\left(\nabla^2\phi_0\right) + 2\left(B - \frac{1}{3}\right)\left(\nabla^2\phi_0\right)\left(\nabla^2\nabla^2\phi_0\right)\right\} \\ F_2 &\equiv -\nabla\cdot(\eta_1\nabla\phi_0) - \nabla\cdot(\eta_0\nabla\phi_1) \\ &- \frac{\mu^2}{2}\left[(B-1)\left[\nabla\cdot\left\{\eta_1\nabla\left(\nabla^2\phi_0\right)\right\} + \nabla\cdot\left\{\eta_0\nabla\left(\nabla^2\phi_1\right)\right\}\right]\right. \\ &+ \left.\nabla\cdot\left\{\eta_0^2\nabla\left(\nabla^2\phi_0\right)\right\}\right] \\ &- \frac{\mu^4}{4}\left[\left(B^2 - B - \frac{B}{6} + \frac{1}{6}\right)\left[\nabla\cdot\left\{\eta_1\nabla\left(\nabla^2\nabla^2\phi_0\right)\right\} + \nabla\cdot\left\{\eta_0\nabla\left(\nabla^2\nabla^2\phi_1\right)\right\}\right]\right. \\ &- \left.\left(B - \frac{1}{3}\right)\nabla^2\cdot\left\{\eta_0\nabla\left(\nabla^2\nabla^2\phi_1\right)\right\}\right] \end{aligned}$$

$$
\begin{aligned}
G_2 \equiv & -\nabla\phi_1\cdot\nabla\phi_0-\frac{\mu^2}{2}\left\{-2\left[\eta_1\nabla^2\phi_{0t}+\eta_0\nabla^2\phi_{1t}\right]\right.\\
+ & (B-1)\left[\nabla\phi_0\cdot\nabla\left(\nabla^2\phi_1\right)+\nabla\phi_1\cdot\nabla\left(\nabla^2\phi_0\right)\right]\\
+ & \left.2\nabla^2\phi_0\nabla^2\phi_1-\eta_0\nabla^2\phi_{0t}-2\eta_0\nabla\phi_0\cdot\nabla\left(\nabla^2\phi_0\right)+2\eta_0\left(\nabla^2\phi_0\right)^2\right\}\\
- & \frac{\mu^4}{4}\left\{-2\left(B-\frac{1}{3}\right)\left[\eta_1\nabla^2\nabla^2\phi_{0t}+\eta_0\nabla^2\nabla^2\phi_{1t}\right]\right.\\
+ & \left(B^2-B-\frac{B}{6}+\frac{1}{6}\right)\left[\nabla\phi_1\cdot\nabla\left(\nabla^2\nabla^2\phi_0\right)+\nabla\phi_0\cdot\nabla\left(\nabla^2\nabla^2\phi_1\right)\right]\\
+ & (B-1)^2\nabla\left(\nabla^2\phi_1\right)\cdot\nabla\left(\nabla^2\phi_0\right)\\
+ & 2\left(B-\frac{1}{3}\right)\left[\left(\nabla^2\phi_1\right)\left(\nabla^2\nabla^2\phi_0\right)+\left(\nabla^2\phi_0\right)\left(\nabla^2\nabla^2\phi_1\right)\right]\\
- & (B-1)\eta_0^2\nabla^2\nabla^2\phi_{0t}-2\left(B-\frac{1}{3}\right)\eta_0\nabla\phi_0\cdot\nabla\left(\nabla^2\nabla^2\phi_0\right)\\
- & \left.2(B-1)\eta_0\nabla\left(\nabla^2\phi_0\right)\cdot\nabla\left(\nabla^2\phi_0\right)+4\left(B-\frac{2}{3}\right)\left(\nabla^2\phi_0\right)\left(\nabla^2\nabla^2\phi_0\right)\right\}
\end{aligned}
$$

We now assume the following random sea as the solution to the $O(1)$ problem:

$$
\eta_0=\sum_n a_n\cos\psi_n;\qquad \phi_0=\sum_n b_n\sin\psi_n; \tag{3.16}
$$

where a_n and b_n are nondimensional amplitudes of the functions η_0 and ϕ_0, $\psi_n=\mathbf{k}_n\cdot\mathbf{x}-\omega_n t$, $\mathbf{k}_n$ is the n-component wavenumber vector nondimensionalized by k_0, $\mathbf{x}$ is the horizontal coordinates vector nondimensionalized by k_0, ω_n is the n-component angular frequency nondimensionalized by $k_0(gh_0)^{1/2}$. Substitution of (3.16) into the $O(1)$ set of equations gives a set of n relationships between ω_n and $k_n=|\mathbf{k}_n|$:

$$
\omega_n^2=\frac{1-\frac{1}{2}\left(B-\frac{1}{3}\right)\mu^2k_n^2+\frac{1}{4}\left(B^2-\frac{B}{3}-\frac{D}{6}+\frac{1}{30}\right)\mu^4k_n^4}{1-\frac{1}{2}(B-1)\mu^2k_n^2+\frac{1}{4}\left(B^2-B-\frac{D}{6}+\frac{1}{6}\right)\mu^4k_n^4} \tag{3.17}
$$

We also find a relationship between a_n and b_n given by:

$$
b_n=\frac{\omega_n}{k_nK_n}a_n; \tag{3.18}
$$

where

$$K_n \equiv k_n \left\{ 1 - \frac{\mu^2}{2} k_n^2 \left(B - \frac{1}{3} \right) + \frac{\mu^4}{4} k_n^4 \left(B^2 - \frac{B}{3} - \frac{D}{6} + \frac{1}{30} \right) \right\} \tag{3.19}$$

Following the standard perturbation technique, we substitute the $O(1)$ solution (3.16) into the right-hand-side of the $O(\delta)$ equations (3.13) to find the forcing of the $O(\delta)$ problem. The forcings F and G in the mass and dynamic equations respectively are:

$$\begin{aligned} F &= \frac{1}{4} \sum_l \sum_m a_m a_l \left\{ \mathcal{F}_{ml}^{+} \sin(\phi_l + \phi_m) + \mathcal{F}_{ml}^{-} \sin(\phi_l - \phi_m) \right\} \\ G &= \frac{1}{4} \sum_l \sum_m a_m a_l \left\{ \mathcal{G}_{ml}^{+} \cos(\phi_l + \phi_m) + \mathcal{G}_{ml}^{-} \cos(\phi_l - \phi_m) \right\} \end{aligned}$$

where

$$\mathcal{F}_{ml}^{\pm} = \frac{\omega_m k_l^2 \pm \omega_l k_m^2 + (\omega_l \pm \omega_m)(\mathbf{k}_l \cdot \mathbf{k}_m)}{\omega_l \omega_m} \tag{3.20}$$

$$\begin{aligned} \mathcal{G}_{ml}^{\pm} &= \frac{1}{k_l k_m K_l K_m} \Big[-\omega_l \omega_m (\mathbf{k}_l \cdot \mathbf{k}_m) + \mu^2 \left\{ \omega_m^2 k_m^2 k_l K_l \right. \\ &+ \left. \omega_l^2 k_l^2 k_m K_m + \frac{1}{2}(B-1)\omega_l \omega_m (k_l^2 + k_m^2)(\mathbf{k}_l \cdot \mathbf{k}_m) \pm \omega_l \omega_m k_l^2 k_m^2 \right\} \\ &+ \mu^4 \left\{ -\frac{1}{2} \left(B - \frac{1}{3} \right) \left(\omega_l^2 k_l^4 k_m K_m + \omega_m^2 k_m^4 k_l K_l \right) \right. \\ &- \frac{1}{4} \left(B^2 - B - \frac{D}{6} + \frac{1}{6} \right) (\mathbf{k}_l \cdot \mathbf{k}_m) \omega_l \omega_m (k_l^4 + k_m^4) \\ &- \frac{1}{4} (B-1)^2 \omega_l \omega_m k_l^2 k_m^2 (\mathbf{k}_l \cdot \mathbf{k}_m) \\ &\mp \left. \left. \frac{1}{2} \left(B - \frac{1}{3} \right) \omega_m \omega_l k_m^2 k_l^2 (k_m^2 + k_l^2) \right\} \right] \end{aligned} \tag{3.21}$$

Equation (3.20) is identical to the full Stokes' theory result, except for the approximate dispersion relationship. Assuming $O(\mu^2) << 1$, and using the dispersion relation and binomial expansions to eliminate K_l and K_n, equation (3.21) can be rearranged to:

$$\mathcal{G}_{ml}^{\pm} = \frac{-\mathbf{k}_l \cdot \mathbf{k}_m + \mu^2 \left\{ \omega_l \omega_m (\omega_l^2 + \omega_m^2) \pm \omega_l^2 \omega_m^2 \right\}}{\omega_l \omega_m} + O(\mu^6) \tag{3.22}$$

which is, again, formally the same as the full Stokes' theory result but with the approximate dispersion relationship.

The forced solution for η_1 can be obtained by solving (3.13) and is given by:

$$\eta_1 = \sum_l \sum_m a_m a_l \left\{ \mathcal{H}^+_{ml} \cos(\phi_l + \phi_m) + \mathcal{H}^-_{ml} \cos(\phi_l - \phi_m) \right\} \tag{3.23}$$

$$\mathcal{H}^{\pm}_{ml} = \frac{\omega^{\pm}_{ml} \mathcal{F}^{\pm}_{ml} - k^{\pm}_{ml} \mathcal{G}^{\pm}_{ml} T^{\pm}_{ml}}{4(\omega^{\pm}_{ml})^2 - k^{\pm}_{ml} T^{\pm}_{ml}}, \tag{3.24}$$

$$T^{\pm}_{ml} \equiv k^{\pm}_{ml} \frac{1 - \frac{\mu^2}{2}\left(B - \frac{1}{3}\right)(k^{\pm}_{ml})^2 + \frac{\mu^4}{4}\left(B^2 - \frac{B}{3} - \frac{D}{6} + \frac{1}{30}\right)(k^{\pm}_{ml})^4}{1 - \frac{\mu^2}{2}(B-1)(k^{\pm}_{ml})^2 + \frac{\mu^4}{4}\left(B^2 - B - \frac{D}{6} + \frac{1}{6}\right)(k^{\pm}_{ml})^4}, \tag{3.25}$$

$$k^{\pm}_{ml} = |\mathbf{k}_l \pm \mathbf{k}_m|, \quad \omega^{\pm}_{ml} = \omega_l \pm \omega_m \tag{3.26}$$

$\mathcal{H}^+_{ml}$, $\mathcal{H}^-_{ml}$ are respectively the super and subharmonics transfer coefficients of the interaction between the (l, m) pair of waves. Figures 3.7 and 3.8 show comparisons of the ratio of $\mathcal{H}^{\pm}_{ml}$ to Stokes' solution, for Nwogu's model, WKGS model, and the present model. Note that the poor representation of these coefficients at small μ in Nwogu's model is due to the assumption of weak nonlinearity, as discussed by Kirby and Wei (1994). The present model predicts superharmonic amplitudes very accurately over a wide range of water depths. The asymptotic representation of subharmonic amplitudes is also more accurate than in previous models, but the new solution deviates more rapidly from the exact solution than do the results of the previous models. Using the rearranged form of $\mathcal{G}^{\pm}_{ml}$, given by (3.22), a much better agreement is achieved. Plots of the rearranged form of $\mathcal{H}^{\pm}_{ml}$ using (3.22)

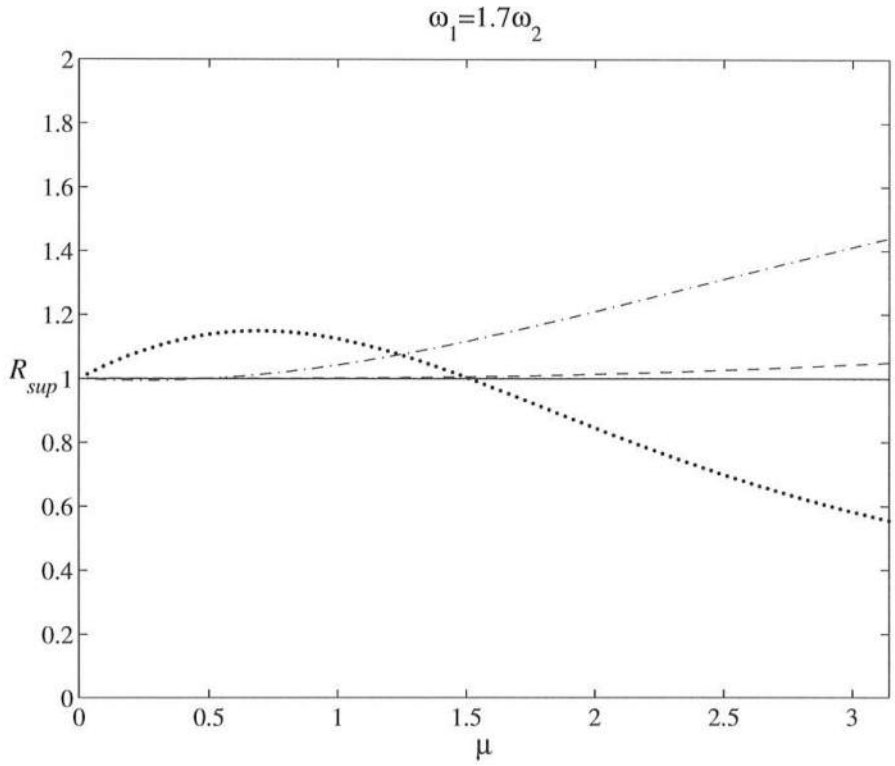

Figure 3.7: Ratio of approximate superharmonic transfer coefficients to Stokes' solution. Stokes' theory (solid), Nwogu (dot), WKGS (dash-dot), Present (dash), Present rearranged (thin dot, indistinguishable from exact).

can also be found in figures 3.7 and 3.8, and the lines are indistinguishable from the full Stokes' theory results.

3.2.2 Third Order Interactions in Narrow Banded Sea

We now extend our analysis to third order interactions by deriving a cubic Schrödinger equation, which governs the evolution of wave envelope resulting from the propagation of a narrow banded spectrum wave train, for the present model and comparing some of its property with the full boundary value problem, and also

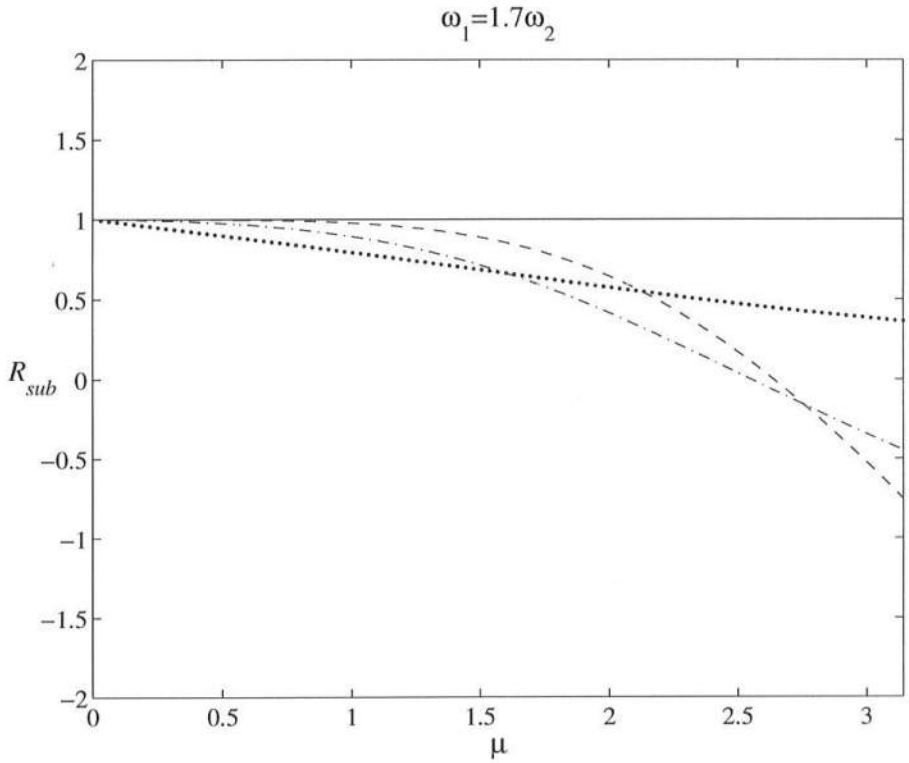

Figure 3.8: Ratio of approximate subharmonic transfer coefficients to Stokes' solution. Stokes' theory (solid), Nwogu (dot), WKGS (dash-dot), Present (dash), Present rearranged (thin dot, indistinguishable from exact).

with the WKGS fully nonlinear second order model. A more detailed derivation of the equation for the present model in given in Appendix B. The derivation is very similar to the derivation for the full boundary value problem, which can be found in Mei (1989) and is done using a standard WKB multiple scales approach. Here we outline the derivation.

A narrow banded wave train with carrier wave number k_0 and angular frequency ω is assumed to be propagating mainly in x direction. At third order, with the expansion (3.12) only, the perturbation is singular, since the forcings are resonant at that order. In order to avoid this problem, the independent variables need to be "stretched", so the time and space variables are split into "fast" and "slow" contributions:

$$\begin{aligned} t &= t' + \delta t' + \delta^2 t' = t' + T_1 + T_2 \\ x &= x' + \delta x' + \delta^2 x' = x' + X_1 + X_2 \\ y &= \delta y' + \delta^2 y' = Y_1 + Y_2 \end{aligned} \tag{3.27}$$

Notice that y has only slow scale contributions. We expand the dependent variables as:

$$\begin{aligned} \eta &= \delta\eta_1 + \delta^2\eta_2 + \delta^3\eta_3 \\ \tilde{\phi} &= \delta\phi_1 + \delta^2\phi_2 + \delta^3\phi_3 \end{aligned} \tag{3.28}$$

We then substitute (3.27) and (3.28) into (3.10) and (3.11), and order the equations in a manner analogous to what was done in the previous section. We assume the solution to each order to be of the form

$$\begin{aligned} \eta_n &= \sum_{m=-(n+1)}^{n+1} \eta_{nm}(X_1, X_2, Y_1, Y_2, T_1, T_2) e^{im(x'-\omega t')} \\ \phi_n &= \sum_{m=-n}^{n} \phi_{nm}(X_1, X_2, Y_1, Y_2, T_1, T_2) e^{im(x'-\omega t')} \end{aligned} \tag{3.29}$$

We then seek an equation for the wave envelope, the leading order wave amplitude, in X_1 and T_1 by relating the coefficients (amplitudes) in (3.29) of each order to the ones of the previous order. After some algebra, the following equation is found before the substitution of ϕ_{10X_1} and ϕ_{10T_1}:

$$\begin{aligned} & A_{T_2} + C_g A_{X_2} - \frac{i}{2}\omega'' A_{X_1X_1} - iC_g A_{Y_1Y_1} + i\sigma_1 |A|^2 A \\ + \; & i\delta\mu \left\{ \phi_{10X_1} + \frac{1 + C_3\mu^2 + C_4\mu^4 - \mu^2\omega^2 (1 + C_1\mu^2)}{2\omega (1 + C_3\mu^2 + C_4\mu^4)} \phi_{10T_1} \right\} = 0 \end{aligned} \tag{3.30}$$

Where $A = 2\eta_{01}$ is the envelope amplitude, $\omega'' = \partial^2\omega/\partial k^2$, and expressions for C_1, C_3, and C_4, are given in Appendix B. The coefficient σ_1 is also given in Appendix B for both the present model and the full potential problem. The final equation for the wave envelope A can be obtained after some more algebra and is given by

$$A_\tau - \frac{i}{2}\omega'' A_{\xi\xi} - \frac{i}{2} C_g A_{Y_1Y_1} + i\sigma\delta^2\mu^2 |A|^2 A + \gamma_1(\tau) A = 0 \tag{3.31}$$

Where $\tau = \delta T_1$, and $\xi = X_1 - C_g T_1$. Without the last term (see Appendix B) and neglecting Y_1 derivatives, equation (3.31) is the nonlinear cubic Schrödinger equation. The last term can be absorbed by defining the transformation $A' = Ae^{i\int \gamma_1 d\tau}$. The coefficient σ is the sum of contributions from the wave-wave interactions σ_1, and wave-current interactions σ_2, also given in Appendix B for the present model as well as for the full potential problem. If the current component (terms involving ϕ_{10}) of equation (3.30) is neglected, and we assume uniform unidirectional propagation (neglect all spatial derivatives), equation (3.30) can be integrated in T_2, and the solution for A is given by:

$$A = a_0 e^{-i(\sigma_1 a_0^2 T_2)} \tag{3.32}$$

where $a_0 = |A|$. The leading order solution of η is, then:

$$\eta_1 = a_0 \cos(kx - \omega_a t) \tag{3.33}$$

where

$$\omega_a = \omega + (\delta\mu)^2 \sigma_1 a_0^2 \tag{3.34}$$

The coefficient σ_1, therefore, characterizes the amplitude dispersion occurring at leading order due to third order wave-wave interactions. Figure 3.9 shows comparison of the ratio σ_1 from the present model and from WKGS model to the Stokes' solution to the full problem. Figure (3.10) shows a similar comparison for σ_2. In both cases, the present model appears to have a better asymptotic approximation to the full problem, with excellent agreement in shallower water and acceptable agreement in intermediate to deep water.

Another important result that can be derived from a linear stability analysis of (3.31) is that concerning the stability of a Stokes' wave train to sideband perturbations (see Mei, 1989). It is well known that, according to such analysis, a permanent form Stokes' wave is a stable solution of (3.31) only in the range where ω'' and $\sigma = \sigma_1 + \sigma_2$ have the same signs. A comparison of the ratio of ω'' to Stokes' solution between the present model and WKGS model is shown in Figure 3.11. Notice that the present model has much better agreement of ω'' with the full model, compared to WKGS model, in any depth up to deep water. Notice that the change in the sign of ω'' in WKGS model at around $\mu = 3.8$ will cause a change in the stability of the model, as long as the sign of σ remains correct, which is the case for both Boussinesq models. For the full boundary value problem, there is a change in the stability at $\mu \approx 1.36$, when σ becomes positive (ω'' remains negative at all depths). For water deeper than this value Stokes' waves are unstable and any sideband perturbation will grow and modulate the solution. A comparison of σ (around the zero crossing) between the present model, WKGS model and Stokes' solution to the full problem is shown in Figure 3.12. In the present model, σ changes sign in shallower water than in the full problem, the

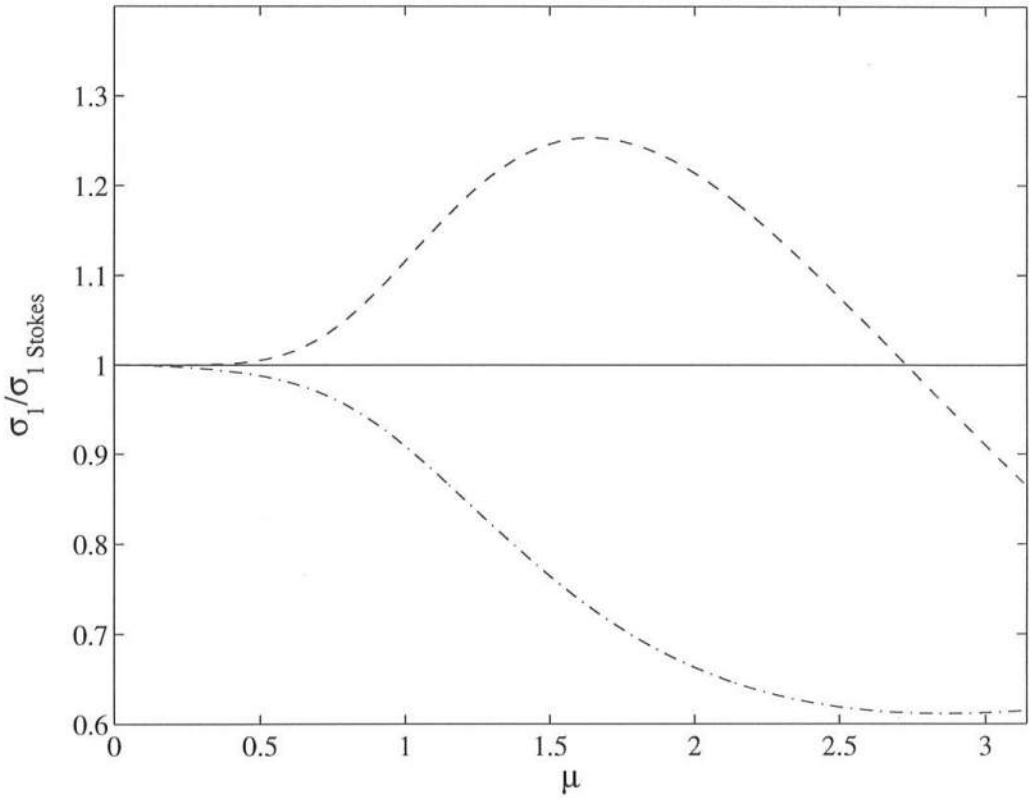

Figure 3.9: Ratio of Schrödinger equation's cubic term coefficient to full problem's solution. Wave-wave interaction contribution. Full boundary value problem (solid), WKGS (dash-dot), Present (dash).

reverse being true for WKGS model. However, this is hardly a problem since in shallow to intermediate water, the time and space scale in which these modulations take place are much longer than those associated with the effects of depth changes. Also, it is not clear whether or not the discrepancies at higher values of μ are only due to a bad behavior of the perturbation expansion.

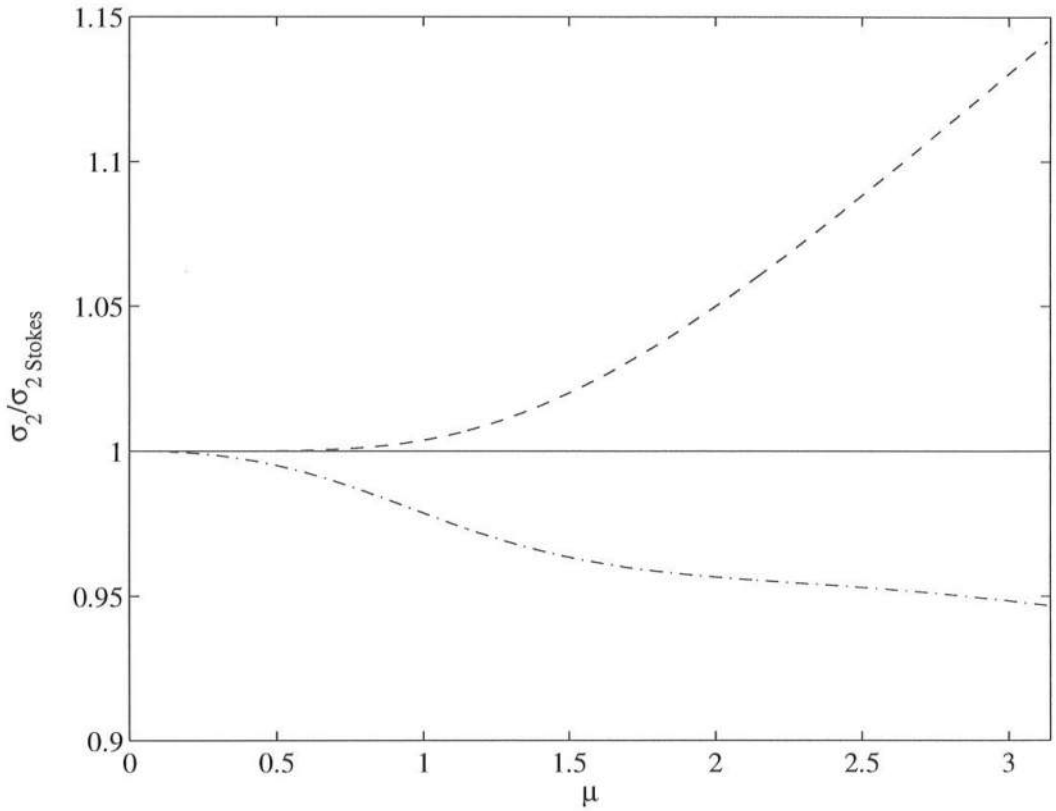

Figure 3.10: Ratio of Schrödinger equation's cubic term coefficient to full problem's solution. Wave-current interaction contribution. Full boundary value problem (solid), WKGS (dash-dot), Present (dash).

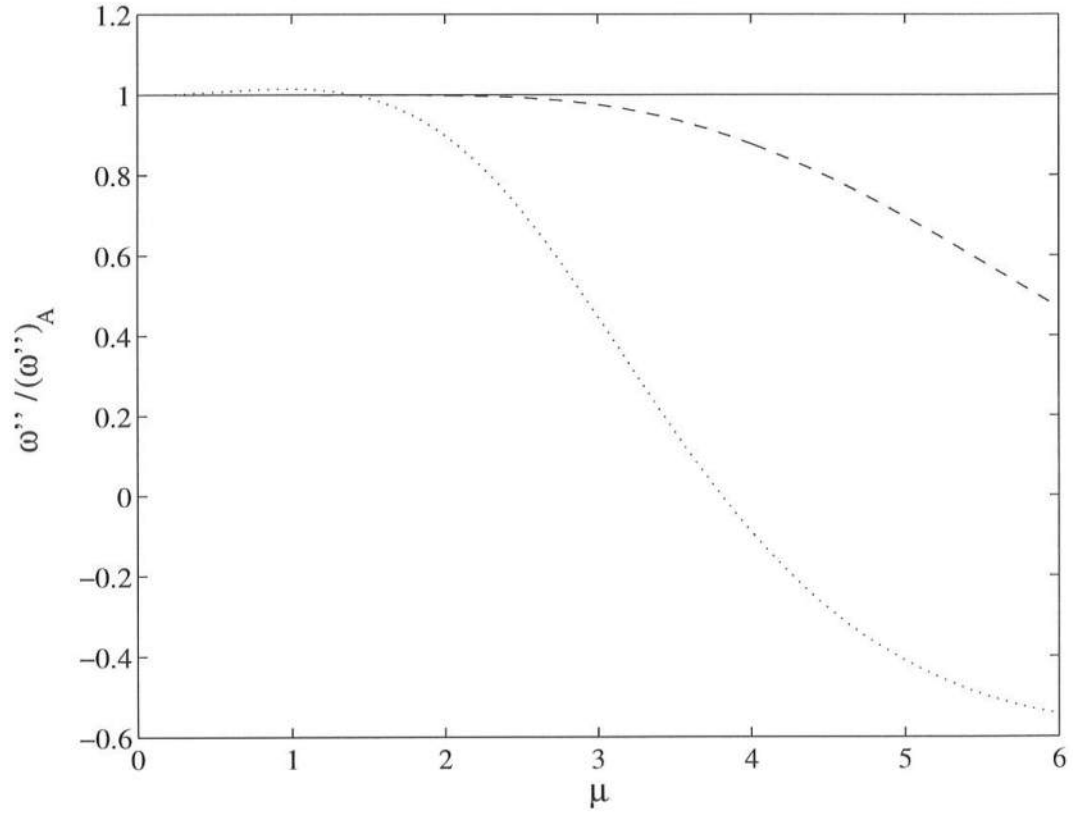

Figure 3.11: $\partial^2\omega/\partial k^2$ ratios to exact linear solution. Full boundary value problem (solid), WKGS (dot), Present (dash).

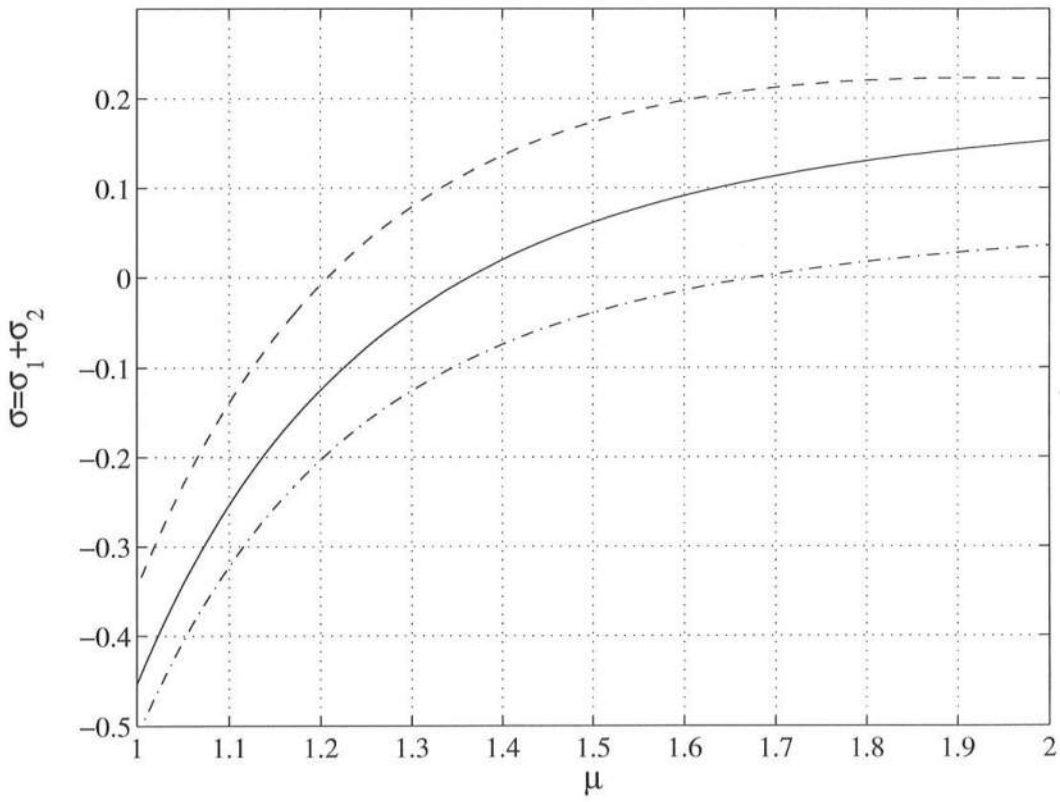

Figure 3.12: Schrödinger equation's cubic term coefficient. Full boundary value problem (solid), WKGS (dash-dot), Present (dash).

Chapter 4

NUMERICAL IMPLEMENTATION

In this chapter we present the numerical implementation of the FN4 (and WN4) model derived in Chapter 2. The philosophy behind this scheme follows very closely the one of WKGS, but extended to higher accuracy for consistency with the higher accuracy of the model itself. The time integration is done using a high order predictor-corrector scheme and the spatial derivatives are approximated with high order finite differencing. The order of accuracy in all the discretized terms in the equations is such that the truncation errors, which contain dispersive-type quantities, are always smaller than the highest-order dispersive term in the equations. This was done to assure that even when using relatively large grid spacing, the dispersion introduced by the error due to the discretization will not overwhelm the dispersive terms in the equations themselves. In WKGS, this is accomplished by making the truncation errors of $O(\mu^4)$ when combined with the term being discretized, assuming $k\Delta x = O(\mu)$. Since the present model contains $O(\mu^4)$ dispersion, more accuracy in the approximate derivatives is needed, so that the numerical truncation leads to errors of order higher than $O(\mu^4)$. Among the several ways to implement the boundary conditions, we choose to use fully reflective walls, with energy absorbing sponge layers used near the boundary, in order to implement a radiation condition. This choice was made due to the simplicity and efficiency of this type of boundary condition. With this kind of

formulation, however, it is necessary to include some kind of wave generation inside the domain. The wave generation is implemented by introducing a source function in the mass conservation equation acting on a limited "source region" conveniently placed in the domain.

We rewrite the one dimensional equations with the source function and the sponge layers as follows:

$$\eta_t = -M_x + f_s(x,t), \tag{4.1}$$

$$U_t = -\eta_x - \frac{\delta}{2}\left(\tilde{u}^2\right)_x + \Gamma_1\left(\eta, \tilde{u}_t\right) + \Gamma_2\left(\eta, \tilde{u}\right) - \tilde{u} f_d(x), \tag{4.2}$$

where M, U, Γ_1, Γ_2 are the one-dimensional (in x) versions of the quantities defined in (2.27), (2.29), (2.30), and (2.31). Later in this chapter we will discuss the introduction of the two new terms in the system: $f_s(x,t)$, the source function, and $\tilde{u} f_d(x)$, a dissipation term acting at the sponge layer(s). At this point, we present the finite difference formulae and solution method to the equations above.

4.1 Discretization and Solution Method

In this section we present the formulas used to approximate the partial derivatives and the solution method to the approximate equations. We discretize the spatial coordinate x by: $x_i = i\Delta x, \quad (i = 0, 1, 2, ..N)$ and time t by: $t^j = j\Delta t, \quad (j = 0, 1, 2, ..N_t)$. There are three basic steps in advancing the solution by Δt in time: (i) the right-hand-sides of (4.1) and (4.2) are evaluated, (ii) the equations are integrated in time to solved for η and U, (iii) $\tilde{u}$ is evaluated from U. Since we use a predictor-corrector integration method and we have nonlinear terms containing time derivatives on the right-hand-side of (4.2), starting at the corrector stage of step (i), steps (i) through (iii) are iterated until convergence is attained. We present each of these steps in the following subsections.

4.1.1 Evaluation of the Right-Hand-Sides

As we already stated, the finite-difference approximations to the spatial derivatives in the equations are done is such a way that the truncation error in each term of the equations should lead to errors of order higher than $O(\mu^4)$. Notice that the momentum equation (4.2) contains first order time derivatives of $\tilde{u}$ in Γ_1. These time derivatives are evaluated in conjunction with the predictor-corrector iterated scheme (presented later) by using a finite difference approximation with values of $\tilde{u}$ at times $(j, j-1, j-2, j-3, j-4)\Delta t$ in the predictor stage and $(j+1, j, j-1, j-2, j-3, j-4)\Delta t$ in the corrector stage. The formulas for the time derivatives at each of those j locations were obtained by expanding the variables in Taylor series around each j, multiplying each expansion by a coefficient and solving the system of equations resulting from setting the combination of coefficients of the higher derivatives of t to zero (this is the standard procedure to find finite difference formulas, and was used throughout this chapter). The formulas are:

$$\begin{aligned}
\tilde{u}_{t_i}^{j-4} &= \frac{1}{12\Delta t}\left(-3\tilde{u}_i^j + 16\tilde{u}_i^{j-1} - 36\tilde{u}_i^{j-2} + 48\tilde{u}_i^{j-3} - 25\tilde{u}_i^{j-4}\right) + O(\Delta t^4) \\
\tilde{u}_{t_i}^{j-3} &= \frac{1}{12\Delta t}\left(\tilde{u}_i^j - 6\tilde{u}_i^{j-1} + 18\tilde{u}_i^{j-2} - 10\tilde{u}_i^{j-3} - 3\tilde{u}_i^{j-4}\right) + O(\Delta t^4) \\
\tilde{u}_{t_i}^{j-2} &= \frac{1}{12\Delta t}\left(-\tilde{u}_i^j + 8\tilde{u}_i^{j-1} - 8\tilde{u}_i^{j-3} + \tilde{u}_i^{j-4}\right) + O(\Delta t^4) \\
\tilde{u}_{t_i}^{j-1} &= \frac{1}{12\Delta t}\left(3\tilde{u}_i^j + 10\tilde{u}_i^{j-1} - 18\tilde{u}_i^{j-2} + 6\tilde{u}_i^{j-3} - 1\tilde{u}_i^{j-4}\right) + O(\Delta t^4) \\
\tilde{u}_{t_i}^{j} &= \frac{1}{12\Delta t}\left(25\tilde{u}_i^j - 48\tilde{u}_i^{j-1} + 36\tilde{u}_i^{j-2} - 16\tilde{u}_i^{j-3} + 3\tilde{u}_i^{j-4}\right) + O(\Delta t^4)
\end{aligned}$$

for the predictor stage, and

$$\begin{aligned}
\tilde{u}_{t_i}^{j-4} &= \frac{1}{60\Delta t}\left(12\tilde{u}_i^{j+1} - 75\tilde{u}_i^j + 200\tilde{u}_i^{j-1} - 300\tilde{u}_i^{j-2}\right. \\
&+ \left. 300\tilde{u}_i^{j-3} - 137\tilde{u}_i^{j-4}\right) + O(\Delta t^5) \\
\tilde{u}_{t_i}^{j-3} &= \frac{1}{60\Delta t}\left(-3\tilde{u}_i^{j+1} + 20\tilde{u}_i^j - 60\tilde{u}_i^{j-1} + 120\tilde{u}_i^{j-2}\right. \\
&- \left. 65\tilde{u}_i^{j-3} - 12\tilde{u}_i^{j-4}\right) + O(\Delta t^5)
\end{aligned}$$

$$
\begin{aligned}
\tilde{u}_{t_i}^{j-2} &= \frac{1}{60\Delta t}\left(2\tilde{u}_i^{j+1} - 15\tilde{u}_i^{j} + 60\tilde{u}_i^{j-1} - 20\tilde{u}_i^{j-2}\right. \\
&- \left. 30\tilde{u}_i^{j-3} + 3\tilde{u}_i^{j-4}\right) + O(\Delta t^5) \\
\tilde{u}_{t_i}^{j-1} &= \frac{1}{60\Delta t}\left(-3\tilde{u}_i^{j+1} + 30\tilde{u}_i^{j} + 20\tilde{u}_i^{j-1} - 60\tilde{u}_i^{j-2}\right. \\
&+ \left. 15\tilde{u}_i^{j-3} - 2\tilde{u}_i^{j-4}\right) + O(\Delta t^5) \\
\tilde{u}_{t_i}^{j} &= \frac{1}{60\Delta t}\left(12\tilde{u}_i^{j+1} + 65\tilde{u}_i^{j} - 120\tilde{u}_i^{j-1} + 60\tilde{u}_i^{j-2}\right. \\
&- \left. 20\tilde{u}_i^{j-3} + 3\tilde{u}_i^{j-4}\right) + O(\Delta t^5) \\
\tilde{u}_{t_i}^{j+1} &= \frac{1}{60\Delta t}\left(137\tilde{u}_i^{j+1} - 300\tilde{u}_i^{j} + 300\tilde{u}_i^{j-1} - 200\tilde{u}_i^{j-2}\right. \\
&+ \left. 75\tilde{u}_i^{j-3} - 12\tilde{u}_i^{j-4}\right) + O(\Delta t^5)
\end{aligned}
$$

for the corrector stage.

The formulas for all spatial derivatives in (4.1) and (4.2) at location $i\Delta x$ and at time $j\Delta t$ are given below for centered and off-centered (near but excluding the boundaries, where boundary conditions are used) locations. We use the variable $\tilde{u}$ as an example.

For derivatives appearing in terms of $O(1)$ we have:

centered at i:

$$
\begin{aligned}
\tilde{u}_{x_i}^{j} &= \frac{1}{60\Delta x}\left[45\left(\tilde{u}_{i+1}^{j} - \tilde{u}_{i-1}^{j}\right) - 9\left(\tilde{u}_{i+2}^{j} - \tilde{u}_{i-2}^{j}\right)\right. \\
&+ \left. \tilde{u}_{i+3}^{j} - \tilde{u}_{i-3}^{j}\right] + O(\Delta x^6) \\
\tilde{u}_{xx_i}^{j} &= \frac{1}{180\Delta x^2}\left[270\left(\tilde{u}_{i+1}^{j} + \tilde{u}_{i-1}^{j}\right) - 27\left(\tilde{u}_{i+2}^{j} + \tilde{u}_{i-2}^{j}\right)\right. \\
&+ \left. 2\left(\tilde{u}_{i+3}^{j} + \tilde{u}_{i-3}^{j}\right) - 490\tilde{u}_i^{j}\right] + O(\Delta x^5)
\end{aligned}
$$

off-centered at $i = 1$ and $i = N - 1$:

$$
\tilde{u}_{x_{1,N-1}}^{j} = \pm\frac{1}{60\Delta x}\left[-10\tilde{u}_{0,N}^{j} - 77\tilde{u}_{1,N-1}^{j} + 150\tilde{u}_{2,N-2}^{j} - 100\tilde{u}_{3,N-3}^{j}\right.
$$

$$
\begin{aligned}
&+ \quad 50\tilde{u}^j_{4,N-4} - 15\tilde{u}^j_{5,N-5} + 2\tilde{u}^j_{6,N-6}\Big] + O(\Delta x^6) \\
\tilde{u}_{xx}{}^j_{1,N-1} &= \frac{1}{180\Delta x^2}\Big[137\tilde{u}^j_{0,N} - 147\tilde{u}^j_{1,N-1} - 255\tilde{u}^j_{2,N-2} + 470\tilde{u}^j_{3,N-3} \\
&- \quad 285\tilde{u}^j_{4,N-4} + 93\tilde{u}^j_{5,N-5} - 13\tilde{u}^j_{6,N-6}\Big] + O(\Delta x^5)
\end{aligned}
$$

off-centered at $i = 2$ and $i = N - 2$:

$$
\begin{aligned}
\tilde{u}_x{}^j_{1,N-1} &= \pm\frac{1}{60\Delta x}\Big[2\tilde{u}^j_{0,N} - 24\tilde{u}^j_{1,N-1} - 35\tilde{u}^j_{2,N-2} + 80\tilde{u}^j_{3,N-3} \\
&- \quad 30\tilde{u}^j_{4,N-4} + 8\tilde{u}^j_{5,N-5} - \tilde{u}^j_{6,N-6}\Big] + O(\Delta x^6) \\
\tilde{u}_{xx}{}^j_{1,N-1} &= \frac{1}{180\Delta x^2}\Big[-13\tilde{u}^j_{0,N} + 228\tilde{u}^j_{1,N-1} - 420\tilde{u}^j_{2,N-2} + 200\tilde{u}^j_{3,N-3} \\
&+ \quad 15\tilde{u}^j_{4,N-4} - 12\tilde{u}^j_{5,N-5} + 2\tilde{u}^j_{6,N-6}\Big] + O(\Delta x^5)
\end{aligned}
$$

The "$\pm$" indicates that the expression should be positive for the points near the left boundary ($i = 0$) and negative near the right boundary ($i = N$). This convention applies for the formulas below as well.

For terms of $O(\mu^2)$:

centered at i:

$$
\begin{aligned}
\tilde{u}_x{}^j_i &= \frac{1}{12\Delta x}\Big[8\left(\tilde{u}^j_{i+1} - \tilde{u}^j_{i-1}\right) - \tilde{u}^j_{i+2} + \tilde{u}^j_{i-2}\Big] + O(\Delta x^4) \\
\tilde{u}_{xx}{}^j_i &= \frac{1}{12\Delta x^2}\Big[16\left(\tilde{u}^j_{i+1} + \tilde{u}^j_{i-1}\right) - \tilde{u}^j_{i+2} - \tilde{u}^j_{i-2} - 30\tilde{u}^j_i\Big] + O(\Delta x^3) \\
\tilde{u}_{xxx}{}^j_i &= \frac{1}{8\Delta x^3}\Big[-13\left(\tilde{u}^j_{i+1} - \tilde{u}^j_{i-1}\right) + 8\left(\tilde{u}^j_{i+2} - \tilde{u}^j_{i-2}\right) \\
&- \quad \left(\tilde{u}^j_{i+3} - \tilde{u}^j_{i-3}\right) - 490\tilde{u}^j_i\Big] + O(\Delta x^4)
\end{aligned}
$$

off-centered at $i = 1$ and $i = N - 1$:

$$
\begin{aligned}
\tilde{u}_x{}^j_{1,N-1} &= \pm\frac{1}{12\Delta x}\Big[-3\tilde{u}^j_{0,N} - 10\tilde{u}^j_{1,N-1} + 18\tilde{u}^j_{2,N-2} \\
&- \quad 6\tilde{u}^j_{3,N-3} + \tilde{u}^j_{4,N-4}\Big] + O(\Delta x^4) \\
\tilde{u}_{xx}{}^j_{1,N-1} &= \frac{1}{12\Delta x^2}\Big[11\tilde{u}^j_{0,N} - 20\tilde{u}^j_{1,N-1} + 6\tilde{u}^j_{2,N-2}
\end{aligned}
$$

$$
\begin{aligned}
&+ \quad 4ut^{j}_{3,N-3} - \tilde{u}^{j}_{4,N-4}\Big] + O(\Delta x^3) \\
\tilde{u}_{xxx}{}^{j}_{1,N-1} &= \pm\frac{1}{8\Delta x^3}\Big[-15\tilde{u}^{j}_{0,N} + 56\tilde{u}^{j}_{1,N-1} - 83\tilde{u}^{j}_{2,N-2} + 64\tilde{u}^{j}_{3,N-3} \\
&- \quad 29\tilde{u}^{j}_{4,N-4} + 8\tilde{u}^{j}_{5,N-5} - \tilde{u}^{j}_{6,N-6}\Big] + O(\Delta x^4)
\end{aligned}
$$

off-centered at $i = 2$ and $i = N - 2$:

$$
\begin{aligned}
\tilde{u}_{xxx}{}^{j}_{1,N-1} &= \pm\frac{1}{8\Delta x^3}\Big[-\tilde{u}^{j}_{0,N} - 8\tilde{u}^{j}_{1,N-1} + 35\tilde{u}^{j}_{2,N-2} - 48\tilde{u}^{j}_{3,N-3} \\
&+ \quad 29\tilde{u}^{j}_{4,N-4} - 8\tilde{u}^{j}_{5,N-5} + \tilde{u}^{j}_{6,N-6}\Big] + O(\Delta x^4)
\end{aligned}
$$

For terms of $O(\mu^4)$:

centered at i:

$$
\begin{aligned}
\tilde{u}_{x}{}^{j}_{i} &= \frac{1}{2\Delta x}\left(\tilde{u}^{j}_{i+1} - \tilde{u}^{j}_{i-1}\right) + O(\Delta x^2) \\
\tilde{u}_{xx}{}^{j}_{i} &= \frac{1}{2\Delta x^2}\left(\tilde{u}^{j}_{i+1} - 2\tilde{u}^{j}_{i} + \tilde{u}^{j}_{i-1}\right) + O(\Delta x) \\
\tilde{u}_{xxx}{}^{j}_{i} &= \frac{1}{\Delta x^3}\left[-2\left(\tilde{u}^{j}_{i+1} - \tilde{u}^{j}_{i-1}\right) + \tilde{u}^{j}_{i+2} - \tilde{u}^{j}_{i-2}\right] + O(\Delta x^2) \\
\tilde{u}_{xxxx}{}^{j}_{i} &= \frac{1}{\Delta x^4}\left[-4\left(\tilde{u}^{j}_{i+1} + \tilde{u}^{j}_{i-1}\right) + \tilde{u}^{j}_{i+2} + \tilde{u}^{j}_{i-2} + 6\tilde{u}^{j}_{i}\right] + O(\Delta x)
\end{aligned}
$$

off-centered at $i = 1$ and $i = N - 1$:

$$
\begin{aligned}
\tilde{u}_{xxx}{}^{j}_{1,N-1} &= \pm\frac{1}{12\Delta x^3}\Big[-3\tilde{u}^{j}_{0,N} + 10\tilde{u}^{j}_{1,N-1} - 12\tilde{u}^{j}_{2,N-2} \\
&+ \quad 6\tilde{u}^{j}_{3,N-3} - \tilde{u}^{j}_{4,N-4}\Big] + O(\Delta x^2) \\
\tilde{u}_{xxxx}{}^{j}_{1,N-1} &= \frac{1}{12\Delta x^4}\Big[\tilde{u}^{j}_{0,N} - 4\tilde{u}^{j}_{1,N-1} + 6\tilde{u}^{j}_{2,N-2} \\
&- \quad 4\tilde{u}^{j}_{3,N-3} + \tilde{u}^{j}_{4,N-4}\Big] + O(\Delta x)
\end{aligned}
$$

For equation (4.1) all but the boundary points (that is, $i = 1, ..., N-1$) are evaluated. After the time integration is done (see next subsection), a boundary

condition $\eta_x = 0$ is applied at $i = 0$ and $i = N$. A 7-point off-centered derivative of η is used and η_0^{j+1} and η_N^{j+1} can be obtained as:

$$\begin{aligned}\eta_{0,N}^{j+1} &= \frac{1}{147}\left(360\eta_{1,N-1}^{j+1} - 450\eta_{2,N-2}^{j+1} + 400\eta_{3,N-3}^{j+1}\right. \\ &- \left. 225\eta_{4,N-4}^{j+1} + 72\eta_{5,N-5}^{j+1} - 10\eta_{6,N-6}^{j+1}\right) + O(\Delta x^7)\end{aligned}$$

For equation (4.2), we only evaluate the terms at points $i = 2, ..., N-2$. The remaining points do not need to be evaluated since at those points, the values of $\tilde{u}$ are determined by boundary conditions. This is done when we evaluate $\tilde{u}$ from U, defined in (2.29), and the procedure will be explained later.

4.1.2 Time Integration

The integration method used is a 5^{th} order predictor, 6^{th} order corrector, Adams-Bashforth-Moulton scheme. Once the dependent variables are known at times $(j-4, j-3, j-2, j-1, j)\Delta t$, and the right-hand-sides of the equations have been evaluated, estimates of both η and U at time $(j+1)\Delta t$ are made using the predictor stage:

$$\begin{aligned}{v_i^{j+1}}_p &= v_i^j + \frac{\Delta t}{720}\left(1901V_i^j - 2774V_i^{j-1}\right. \\ &+ \left. 2616V_i^{j-2} - 1274V_i^{j-3} + 251V_i^{j-4}\right) + O(\Delta t^6),\end{aligned}$$

where index p stands for predictor. v_i^j is either U or η, and V_i^j is the right-hand-side of the respective equation, at $x = i\Delta x$ and $t = j\Delta t$. With the estimate ${U^{j+1}}_p$, we evaluate ${\tilde{u}^{j+1}}_p$ (see next subsection) then estimate the right-hand-sides of the equations at t^{j+1}, ${V_i^{j+1}}_p$, and iterate the corrector stage:

$$\begin{aligned}v_i^{j+1} &= v_i^j + \frac{\Delta t}{1440}\left(475{V_i^{j+1}}_p + 1427V_i^j - 798V_i^{j-1}\right. \\ &+ \left. 482V_i^{j-2} - 173V_i^{j-3} + 27V_i^{j-4}\right) + O(\Delta t^7),\end{aligned}$$

until the error between v_i^{j+1} and $v_i^{j+1}{}_p$ (where, again, v applies here applies to both η and U) is small. We define an error estimate for the iteration process as:

$$E_{iter} = \left[\sum_{i=0}^{N} \frac{\left(\eta_i^{j+1}{}_p - \eta_i^{j+1}\right)^2}{\left(\eta_i^{j+1}\right)^2}\right]^{1/2} + \left[\sum_{i=0}^{N} \frac{\left(\tilde{u}_i^{j+1}{}_p - \tilde{u}_i^{j+1}\right)^2}{\left(\tilde{u}_i^{j+1}\right)^2}\right]^{1/2}, \tag{4.3}$$

and require that E_{iter} be smaller than an arbitrary tolerance T_{err}. In all our computations we used $10^{-9} < T_{err} < 10^{-12}$.

4.1.3 Evaluation of $\tilde{u}$ from U

Once U has been evaluated at $t = (j+1)\Delta t$ for $x = i\Delta x, i = 2, 3, ..., N-3, N-2$, a system of algebraic equations can be written as

$$A_{m\times m}\tilde{u}_m = U_m, \quad m = N-3 \tag{4.4}$$

where

$$A_{m\times m} = \begin{pmatrix} c_2 & d_2 & e_2 & 0 & ... & 0 & 0 \\ b_3 & c_3 & d_3 & e_3 & ... & 0 & 0 \\ a_4 & b_4 & c_4 & d_4 & e_4 & 0 & 0 \\ 0 & ... & ... & ... & ... & ... & 0 \\ 0 & ... & a_{N-4} & b_{N-4} & c_{N-4} & d_{N-4} & e_{N-4} \\ 0 & ... & 0 & a_{N-3} & b_{N-3} & c_{N-3} & d_{N-3} \\ 0 & ... & 0 & 0 & a_{N-2} & b_{N-2} & c_{N-2} \end{pmatrix} \tag{4.5}$$

$\tilde{u}_m$ and U_m are the vectors containing the unknowns $\tilde{u}$ and U at $i = 2, ..., N-2$. Each row of the system represents the finite difference approximation for the definition of $U(\tilde{u})$ (2.29). a_i, b_i, c_i, d_i, e_i are the coefficients appearing in front of $\tilde{u}$ after the 5-point derivatives are substituted into (2.29), except for rows 2, 3, N-3, N-2, where these coefficients are modified to accommodate the boundary conditions given by $\tilde{u}_{xx} = \tilde{u} = 0$. After solving the system for $\tilde{u}$ at $i = 2, .., N-2$, we

use these conditions (with an off-centered 5-point finite-difference approximation) to obtain

$$\begin{aligned} \tilde{u}_{0,N}^{j+1} &= 0 \\ \tilde{u}_{1,N-1}^{j+1} &= \frac{1}{104}\left(114\tilde{u}_{2,N-2}^{j+1} - 56\tilde{u}_{3,N-3}^{j+1} + 11\tilde{u}_{4,N-4}^{j+1}\right). \end{aligned}$$

The justification for using the boundary conditions $\tilde{u}_{xx} = \tilde{u} = \eta_x = 0$ is to guarantee that the mass flux

$$M = h\left[\tilde{u} + \frac{1}{2}\left(B - \frac{1}{3}\right)h^2\tilde{u}_{xx} + \frac{1}{4}\left(B^2 - \frac{B}{3} - \frac{D}{6} + \frac{1}{30}\right)h^4\tilde{u}_{xxxx}\right] \tag{4.6}$$

vanishes at the walls, which can be verified exactly by substituting $\tilde{u}_{xx} = \tilde{u} = \eta_x = 0$ into the linearized flat bottom momentum equation:

$$\begin{aligned} g\eta_x &+ \left[\tilde{u} + \frac{1}{2}(B-1)h^2\tilde{u}_{xx}\right. \\ &+ \left.\frac{1}{4}\left(B^2 - B - \frac{D}{6} + \frac{1}{6}\right)h^4\tilde{u}_{xxxx}\right]_t = 0 \end{aligned}$$

and obtaining that $\tilde{u}_{xxxx} = 0$, and therefore that $M = 0$ at the boundary.

4.1.4 Convergence and Stability

No stability analysis for the present numerical formulation of the FN4 model was done, due to the complexity of the model as well as the numerical scheme. To attain the desired accuracy in the model with relatively fast convergence, the Courant number (in a linear shallow water theory sense) used in all cases was never larger than 0.3. The numerical implementation for the linearized model proved to be stable for all cases tested. For some cases, it was necessary to filter the solution as high frequency oscillations growth appeared near the points where the bottom slope was discontinuous. This is due to the fact that the FN4

model contains terms proportional to high (up to fourth) derivatives of h with respect to x, and, for discontinuous bottom slopes, these factors become singular and can introduce spurious high frequency waves to the solution. When necessary we used a Shapiro (1970) filter with either 8 or 16-point average, and the filter was applied every N_f time steps where $50 < N_f < 500$, depending on the case.

In most cases where nonlinear effects become important (very steep, high waves), the iteration process tend to become slow, or even diverge. To correct this problem we adopted a relaxation technique in the iteration process, as follows: if with two iterations the error tolerance is not met, we assume that the corrector is overshooting the desired solution and apply the formula to both $\tilde{u}$ and η:

$$f_i^{j+1}{}_r = (1-R) f_i^{j+1}{}_p + R f_i^{j+1} \tag{4.7}$$

where the relaxation coefficient, R ranges from 0 to 1. $f_i^{j+1}{}_p$ is the estimate in the previous iteration, and f_i^{j+1} is the estimate in the current iteration, which is replaced by the relaxed vector $f_i^{j+1}{}_r$. The optimal value of R strongly depends the type of problem. For most cases, we used $0.2 < R < 1$. For very highly nonlinear (near breaking) solitary waves it was necessary to use R as small as 0.08 to keep the solution from diverging. The number of iterations necessary for convergence within the desired accuracy was typically less than 6, but for some very near-breaking solitary waves it was as high as 20.

4.2 The Sponge Layer

The last term in (4.2) is a linear friction-type term and is referred to as a "Newtonian cooling" by Israeli and Orszag (1989). Other types of dissipation terms such as viscous-type dissipation (analogous to dissipation due to viscosity in the Navier-Stokes equations), and "sponge-filter" (Israeli and Orszag, 1989)

are also possible, but it was found that the Newtonian cooling was sufficient to damp the waves with efficiency and emulate well the radiation condition. In principle, the only required rule for the sponge layer function f_d is that it must vanish everywhere except near the boundaries, where the dissipation takes place. In practice, a smooth transition between the sponge layer and the interior of the domain is necessary to minimize reflection from the sponge layer back into the domain, which is highly undesirable. We choose the same form for the sponge layer coefficient $f_d(x)$ as did Wei (1997):

$$f_d(x) = \begin{cases} \frac{S \exp[(x_P)^N - 1]}{\exp(1) - 1} & x_S < x < x_L \\ 0 & 0 < x < x_S \end{cases} \tag{4.8}$$

where x_P is a transformed coordinate defined by

$$x_P = \frac{x - x_S}{x_L - x_S}, \tag{4.9}$$

and S is a dissipation strength constant. In all our computations, $N = 2$ gave satisfactory results. Reasonable width of the sponge layer $(x_L - x_S)$ and values of S depend on the wave conditions. Values of $20 < S < 40$ combined with the sponge layer width of about three to four times the characteristic wavelength gave satisfactory results for all cases considered. For deeper water (shorter waves), the velocity variable $\tilde{u}$ can be quite small, and the dissipation term may not be able to damp the waves very efficiently. For such cases, S or $x_L - x_S$ (or both) should be increased.

4.3 Wave Generation Inside the Domain: Source Function

It should be clear that using sponge layers near the boundaries rules out the possibility of any type of wave generation at the boundary. It is therefore

necessary to introduce a source term inside the domain to generate the desired waves, which will be allowed to propagate towards the boundaries, where these waves are damped by virtue of the sponge layers. This is the role of the last term in (4.1), $f_s(x,t)$. The first attempt to include such terms in Boussinesq models was made by Larsen and Dancy (1983), in which mass is added and subtracted from the domain along a single line (point, in the case of a one-dimensional model). Wei (1997) found that this approach, which worked well with the staggered grid of Larsen and Dancy (1983), did not work well in his non-staggered grid, where spurious noise appeared around the source point. It was necessary therefore to distribute the source function around a certain neighborhood of the source. In the present formulation, we closely follow the approach of Wei (1997), in which the source function is assumed to be distributed as a Gaussian shape, making the appropriate modifications to account for the added complexity of the model. The formulation for the source function presented next is one-dimensional, but can be extended to two dimensions is a straightforward manner.

If the local water depth at the source region is constant, h, and we want to generate regular waves with angular frequency ω, the source function can be written as:

$$f_s(x,t) = D_s \exp[-\beta_s(x - x_s)^2] \sin(\omega t), \tag{4.10}$$

where x_s is the center of source function, β_s determines how focused the source function is, and D_s is the magnitude of the source function. Assuming that the generated wave have small amplitude, we can use the linearized version of the FN4 model and derive an exact analytical expression for D_s by using Green's function theory (see Appendix C), to obtain:

$$D_s = \frac{\eta_0}{\omega \alpha_s I_1 \left[1 + C_3 (kh)^2 + C_4 (kh)^4\right]}, \tag{4.11}$$

where k is the wave number computed from the linear dispersion relationship for the present model (see chapter 3), of the wave generated at the source function when it is away from the source region, C_3 and C_4 are constants given in chapter 3, α_s and I_1 are given in appendix C.

Although the gaussian shape parameter β_s is arbitrary, in practice its value has great influence on how well the source function can generate the desired waves. Ideally, β should be as large as possible, so that the source function would be more localized. However, it turns out that if the source region is too narrow (large β_s), the waves generated can be quite distorted and noise may also appear when the waves not are small amplitude (see next subsection). Defining the width of the source region W_s to be the distance between two coordinates (equidistant from the source center) where $\exp[-\beta_s(x - x_s)^2]$ is equal to e^{-5}, we can write:

$$W_s = 2\sqrt{5/\beta_s}. \tag{4.12}$$

By trial and error, it was found that, for regular waves, a source with width W_s approximately equal to the wave length, gives satisfactory results for waves within a wide range of amplitudes and wavenumber. Sensitivity tests for W_s were performed and are shown next.

4.3.1 Tests

Tests of the source function and sponge layers are now presented. Figure 4.1 shows schematically the location of the source and the sponge layers. In all the cases a wave with period $T = 1.5s$, and wavelength $L = 3.35m$ was used. The water depth is $h = 1m$, sponge layers widths are $3L$, and sponge layer strength $S = 30$. Six cases were considered: amplitudes $a_0 = 0.01m$, $a_0 = 0.05m$, and $a_0 = 0.1m$, each for source region with $W_s = 0.25L$ and $W_s = L$. Figure 4.2

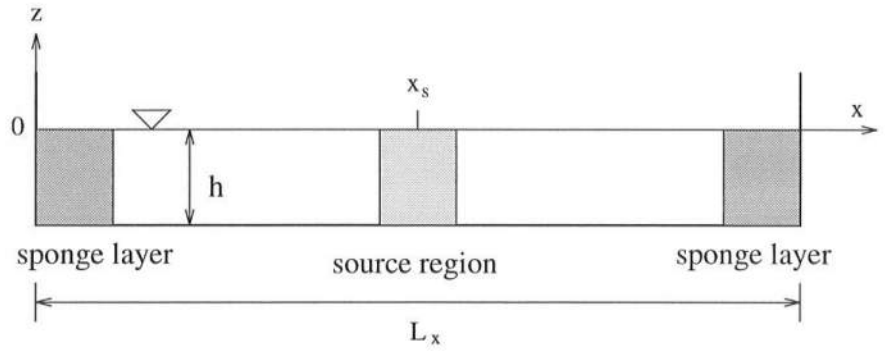

Figure 4.1: Sketch of the domain for source function and sponge layers tests. Domain length $L_x = 80m$ was used throughout.

shows results at various times prior to "steady-state", for $a_0 = 0.01m$, and both source widths. Notice that for this particular case of very small amplitude waves, the source function worked quite well in generating the desired waves, regardless of the width W_s. With $a_0 = 0.05m$, a more "nonlinear wave", 4.3 shows that the narrower source region was not able to generate clean waves, and it can be seen that higher frequencies contaminate the solution. Notice that these higher frequencies are not necessarily near the Nyquist (instability-type) frequency. It seems that the higher harmonics generated by the model are not behaving as we desire as they are generated in the source function (which is derived from linear theory). Using $W_s = L$, however, this problem is corrected for this amplitude. It seems that a good resolution of the source function, that is a larger W_s, is necessary to keep undesirable higher frequencies from appearing in the solution. 4.3 shows similar results for even higher waves $a_0 = 0.1m$. With $W_s = 0.25L$, the solution became unstable right after $t = 4T$, whereas for $W_s = L$, the resulting waves are still quite clean.

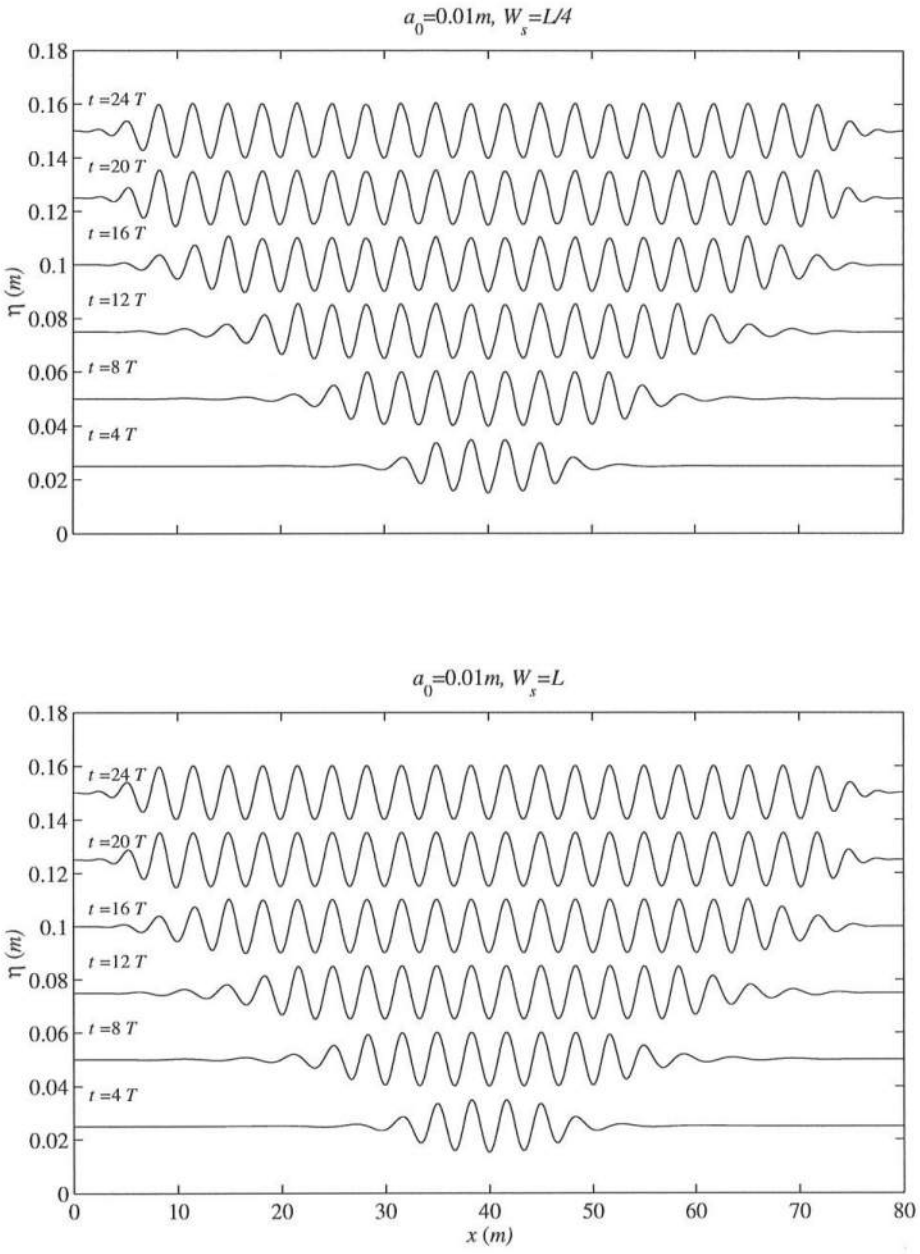

Figure 4.2: Waves with $a_0 = 0.01m$ generated by a source function at $x = 40m$ with $W_s = 0.25L$ (upper panel), and $W_s = L$ (lower panel). $h = 1m$, $T = 1.5s$, $x_L - x_S = 3L$, $S = 30$.

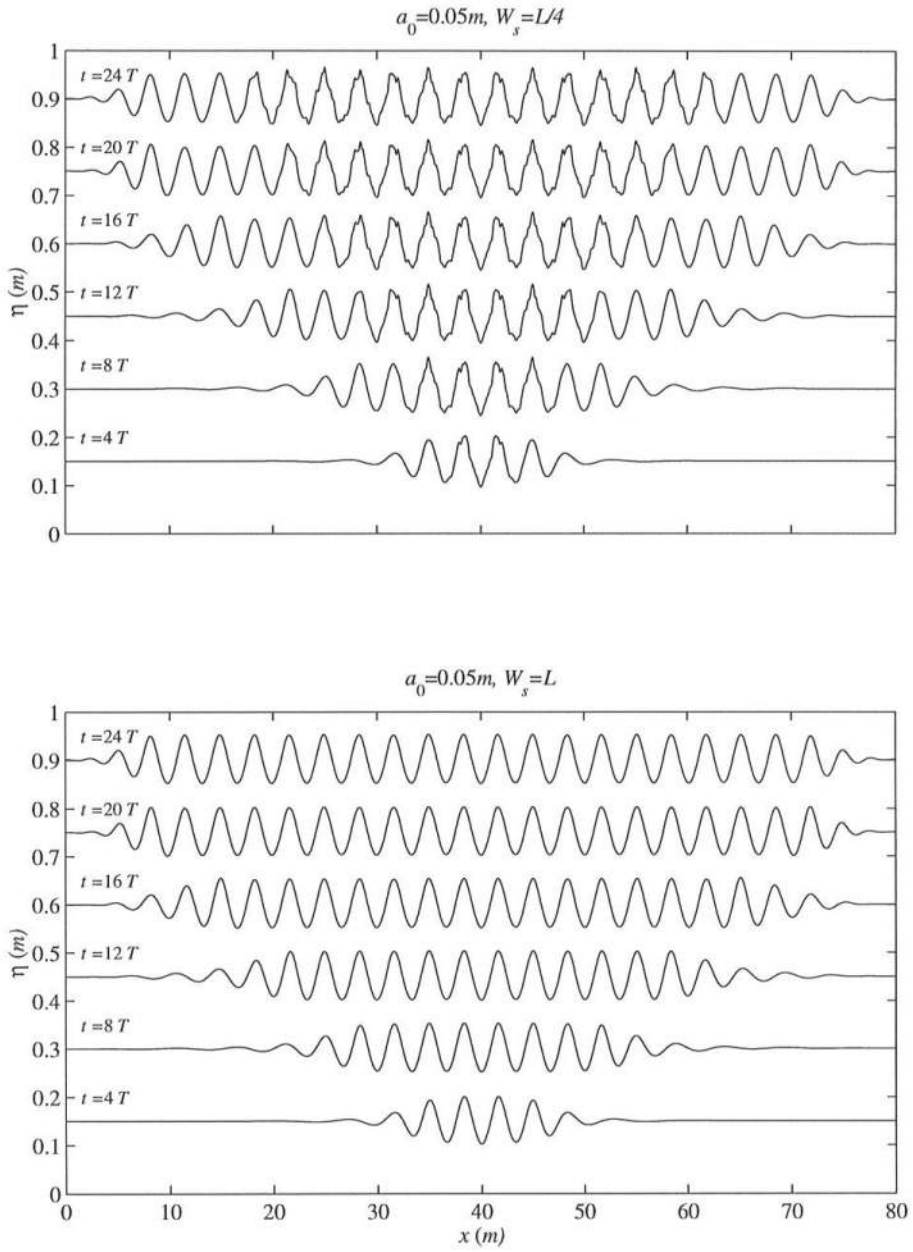

Figure 4.3: Waves with $a_0 = 0.05m$ generated by a source function at $x = 40m$ with $W_s = 0.25L$ (upper panel), and $W_s = L$ (lower panel). $h = 1m$, $T = 1.5s$, $x_L - x_S = 3L$, $S = 30$.

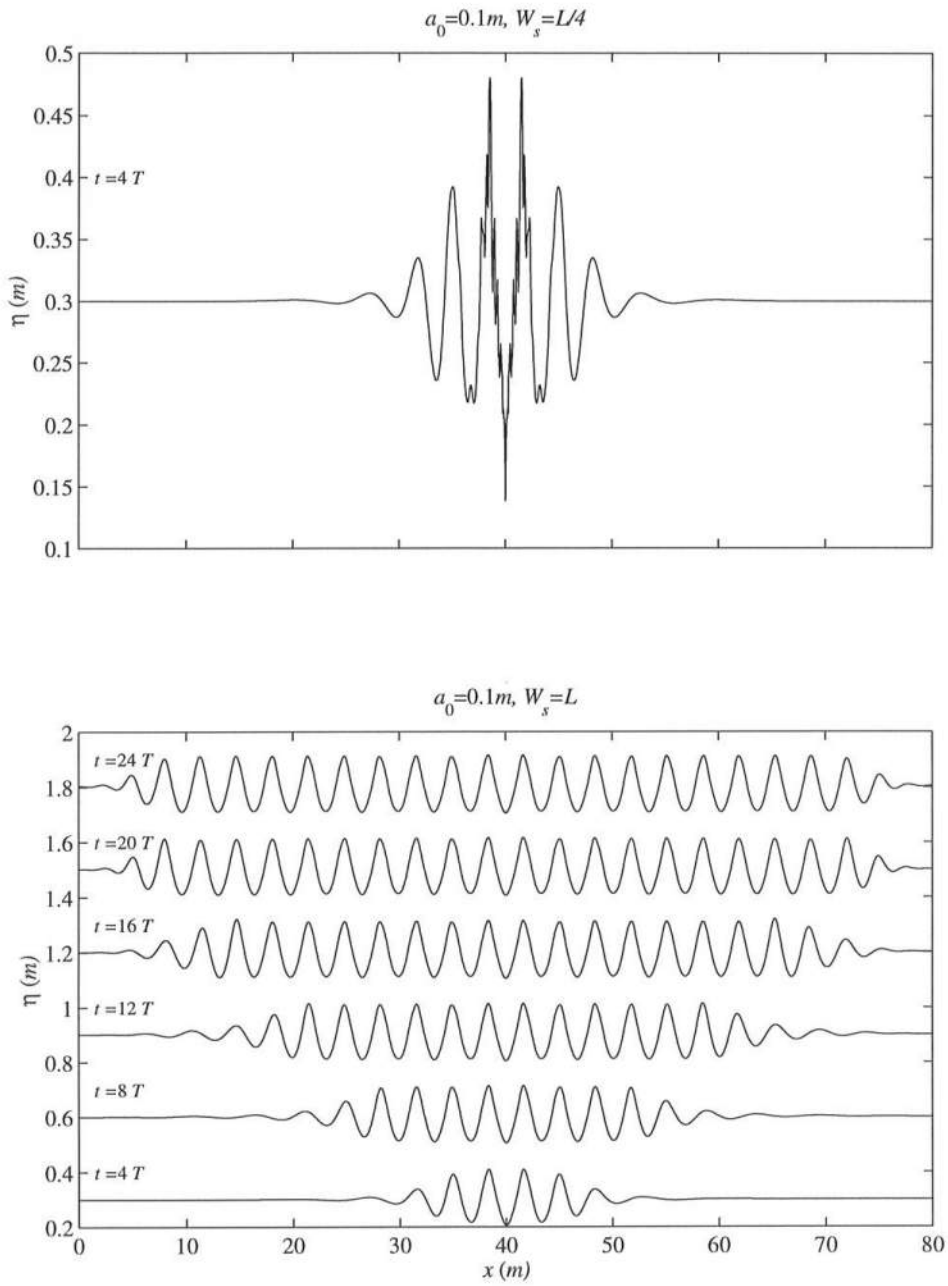

Figure 4.4: Waves with $a_0 = 0.1m$ generated by a source function at $x = 40m$ with $W_s = 0.25L$ (upper panel), and $W_s = L$ (lower panel). $h = 1m$, $T = 1.5s$, $x_L - x_S = 3L$, $S = 30$.

Chapter 5

THE SOLITARY WAVE

The phenomenon known as the solitary wave consists of a limiting wave form with a single crest which propagates in fairly shallow water of constant depth, and where the nonlinear and dispersive effects counterbalance each other yielding a permanent form solution. In this chapter we study solitary waves solutions of the FN4 model, and compare it to other models including extremely accurate solutions of the full boundary value problem (Tanaka, 1986), Green and Naghdi (1976) (GN) type models, and the WKGS model.

Many authors have found approximate solutions for the solitary wave, including the early works of Boussinesq (1871) and Korteweg and deVries (1895). Fenton (1972) developed a model based on a perturbation expansion around the basic shallow water wave theory. His expansion includes terms up 9^{th} order and, at the first three orders, recover the models of Boussinesq (1871), Laitone (1960), and Grimshaw (1971). Longuet-Higgins and Fenton (1974) used conservation of integral quantities such as mass and energy to arrive at extremely accurate relationships between several solitary wave properties, such as the wave height, energy, mass, wave Froude number F_r (nondimensional wave speed), etc. They also proved that the solitary wave with maximum wave height does not correspond to the one with maximum fluid velocity at the crest, or maximum mass.

More recently, in a study of the stability of solitary waves, Tanaka (1986) developed an accurate solution scheme to the full boundary value problem for solitary waves. Throughout this chapter we will use this solution as the "exact" solution in our comparisons. Shields and Webster (1988) studied the accuracy of solitary wave properties of the first 3 levels of the GN models (referred hereafter as GN1, GN2, and GN3). An n^{th} level GN model approximates the horizontal velocity by an $(n-1)^{th}$ polynomial, and the vertical velocity by an n^{th} order polynomial. GN1 recovers the model by Serre (1953), as shown by Kirby (1997). Shields and Webster (1988) derived a GN2 set of equations for unsteady flow over an uneven bottom, and a GN3 model, for one-dimensional steady flow over a flat bottom.

In the next sections, we compare several properties of the solitary wave solution of the FN4 model with the exact solution, numerical WKGS solutions, and also with GN solutions given by Shields and Webster (1988).

5.1 Linear Analytical Asymptotic Solution

At the tail of the solitary wave (away from the crest) the free surface elevation η is very small, and we expect that the linearized set of equations should describe the shape of the wave with good accuracy. In a reference frame moving with the wave at nondimensional wave at speed $F_r = c/\sqrt{gh}$, we can write the following boundary value problem for the wave field far from the crest (located at $x = 0$) in (x, z):

$$\nabla^2\phi = 0 \tag{5.1}$$

$$\phi_x = -F_r \quad x \to \infty \tag{5.2}$$

$$\phi_z = 0 \quad z = -1 \tag{5.3}$$

$$\phi_z = -F_r^2\phi_{xx} \quad z = 0 \tag{5.4}$$

The solution to the system above is

$$\phi = K_1 e^{2\gamma x} \cos 2\gamma z - F_r x \tag{5.5}$$

Substituting (5.5) into (5.4) gives

$$\frac{\tan 2\gamma}{2\gamma} = F_r^2. \tag{5.6}$$

The exact solution for the free surface elevation η far from the crest is of the form

$$\eta = K_2 e^{2\gamma x} \tag{5.7}$$

The parameter γ is referred to as the straining parameter, and (5.6) is directly related to the exact dispersion relationship in linear wave theory.

For the present model, the 2 equations corresponding to the system (5.1-5.4), in terms of the modified velocity variable $\tilde{u}$ are:

$$\eta = F_r \left(\tilde{u} - \mu^2 C_3 \tilde{u}_{xx} + \mu^4 C_4 \tilde{u}_{xxxx} \right) \tag{5.8}$$

$$F_r \eta = \left(\tilde{u} - \mu^2 C_1 \tilde{u}_{xx} + \mu^4 C_2 \tilde{u}_{xxxx} \right) \tag{5.9}$$

where C_1, C_2, C_3, C_4 are defined in Appendix B. We now assume the solution

$$\tilde{u} = e^{-\lambda x}. \tag{5.10}$$

Substituting (5.10) into (5.8,5.9), solving for $\mu^2\lambda^2$ and keeping the relevant root, we obtain

$$\mu^2\lambda^2 = \frac{\left(C_3 {F_r}^2 - C_1\right) - \left[\left(C_3 {F_r}^2 - C_1\right)^2 + 4\left((1 - {F_r}^2\right)\left(C_4 {F_r}^2 - C_2\right)\right]^{1/2}}{2\left(C_4 {F_r}^2 - C_1\right)}. \tag{5.11}$$

To recover Nwogu (1993), refer to chapter 3. The straining parameter γ is related to λ as $2\gamma = -\lambda$.

The expressions for the relation between the straining parameter and the Froude number for GN2, and GN3 (Shields, 1986 and Shields and Webster, 1988) are:

$$2\gamma^2 = \frac{1}{3}\left(52 - 12F_r^{-2} - 4\sqrt{9F_r^{-4} - 33F_r^{-2} + 124}\right) \tag{5.12}$$

and

$$16F_r^2\gamma^6 + 60\left(1 - 9F_r^2\right)\gamma^4 - 20\left(39 - 144F_r^2\right)\gamma^2 + 1575\left(1 - F_r^2\right) = 0 \tag{5.13}$$

respectively.

Figure 5.1 shows comparison between the percentage error to the exact solution of the transcendental equation (5.6) for γ, between the present model, Nwogu's model, GN2, and GN3. Although all models have relatively small errors, the present model is much more accurate than all the others by at least an order of magnitude. Notice that compared to GN2 and Nwogu's model, the difference in the errors is of at least five order of magnitude.

5.2 Solitary Waves with Permanent Form

In this section, the numerical scheme described in chapter 4 is used to compute several approximate solitary wave solutions to the fully nonlinear models FN4 and WKGS. The initial condition used for the model was constructed from the computer program by Tanaka (1986) in the following manner: for the smallest computed wave with amplitude $\eta_{max} \approx 0.2$, η and $\tilde{u}$ (u_α in the case of WKGS) were obtained from Tanaka's exact solution and used as initial condition for FN4

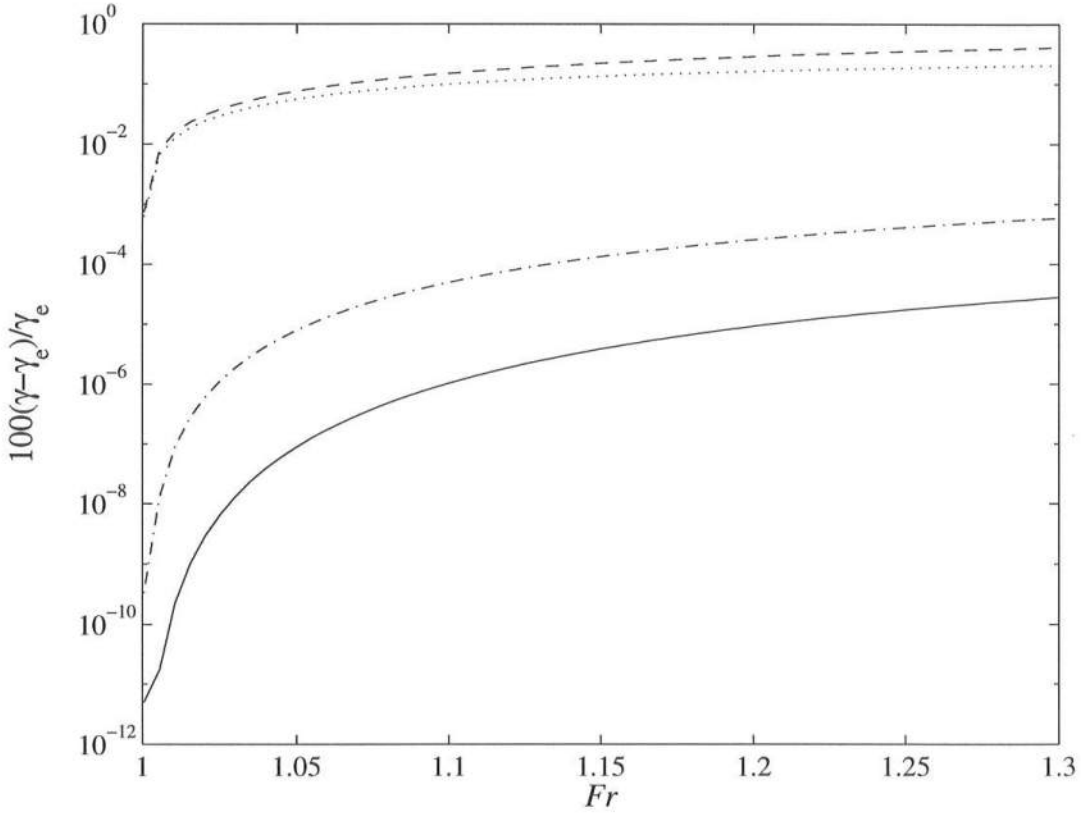

Figure 5.1: Percentage error to exact solution in straining parameter. Present model (full), Nwogu (dash), GN2 (dot), GN3 (dash-dot)

and WKGS. After the solution reached permanent form, it was multiplied by a factor slightly larger than one (typically 1.05) and this re-scaled wave was used as the initial condition for the next case. This procedure was repeated until the desired range of solitary waves was covered, and proved to be more efficient than using Tanaka's solution as the initial condition for all amplitudes. Since Tanaka's and each consecutive re-scaled initial condition do not satisfy the approximate equations, there is a transient period while the solution is not a permanent form solitary wave, but has a dispersive tail of shorter waves left behind. Since these shorter waves travel with phase speeds which are smaller than the "main wave", eventually the tail is left far behind and does not interfere with the solitary wave, which, at this point, can propagate with permanent form. The time required for the solution to achieve a permanent form solitary wave depends on the initial condition. High amplitude initial conditions will reach permanent form more quickly, since the primary wave moves much faster than the tail. Smaller amplitude waves will have less amplitude dispersion and it will take longer for the permanent form solitary wave to separate from the tail. After each solution reaches permanent form it is straightforward to obtain properties such as the Froude number, velocity profiles, mass, energy, etc. No filtering was necessary during these computations, although for higher waves the under-relaxation parameter had to be as small as $r = 0.08$ for the solution to converge with error tolerance in the iteration typically $10^{-12} \leq T_{err} \leq 10^{-9}$. For the permanent form solitary waves we used grid spacing $\Delta x = 0.1h$ for waves with amplitude $0 < \eta_{max} < 0.4h$, $\Delta x = 0.05h$ for $0.4h < \eta_{max} < 0.7h$, and $\Delta x = 0.05h$ for $\eta_{max} > 0.7h$, where $h = 1$. We used Δt such that the Courant number was always below 0.2 (for accuracy purposes).

We now present the following nondimensional quantities for the FN4 model, where the scales for the basic variables are $x = x'h$, $z = z'h$, $t = t'/\sqrt{g/h}$, $u = u'\sqrt{gh}$, and the primes denote nondimensional quantities. The primes in the

formulas below are dropped for the sake of notation clarity. The total mass of the solitary wave above the still water level is given by:

$$M = \int_{-\infty}^{+\infty} \eta dx. \tag{5.14}$$

The potential energy is:

$$V = \int_{-\infty}^{+\infty} \frac{1}{2}\eta^2 dx. \tag{5.15}$$

The kinetic energy is:

$$K = \frac{1}{2}\int_{-\infty}^{+\infty}\int_{0}^{H}\left(u^2 + w^2\right) d\zeta dx \tag{5.16}$$

where $\zeta = (1+z)$, $H = 1+\eta$,

$$u(\zeta) = \tilde{u} + \frac{1}{2}\mu^2\left(B - \zeta^2\right)\tilde{u}_{xx} + \frac{1}{4}\mu^4\left(B - \zeta^2 - \frac{D}{6} + \frac{\zeta^4}{6}\right)\tilde{u}_{xxxx}. \tag{5.17}$$

and

$$w(\zeta) = \mu^2\zeta\tilde{u}_x + \mu^4\left[\left(\frac{1}{2}B\zeta + \frac{1}{6}\zeta^3\right)\tilde{u}_{xxx}\right]. \tag{5.18}$$

After substitution of (5.17) and (5.18) into (5.16) and retaining terms of up to $O(\mu^4)$, we obtain

$$\begin{aligned} K &= \frac{1}{2}\int_{-\infty}^{+\infty}\int_{0}^{H}\left\{\mu^2\left[\tilde{u}^2 + \left(B - \zeta^2\right)\tilde{u}_x\tilde{u}_{xx}\right]\right. \\ &+ \frac{1}{2}\mu^4\left[\left(B - \zeta^2\right)B - \frac{1}{6}\left(D - \zeta^4\right)\right]\tilde{u}_x\tilde{u}_{xxxx} \\ &+ \frac{1}{4}\left[\left(B - \zeta^2\right)\tilde{u}_{xx}\right]^2 \\ &+ \left.(\zeta\tilde{u}_x)^2 + \zeta^2\left(B - \frac{1}{3}\zeta^2\right)\tilde{u}_x\tilde{u}_{xxx}\right\} d\zeta dx. \end{aligned} \tag{5.19}$$

The integral in ζ can be evaluated analytically, and the integrals in x are computed using Bode's rule, which is accurate to $O(\Delta x^6)$, within a range containing the solitary wave and where the free surface at the extremes is negligibly small.

We define the quantity

$$\omega_s = 1 - (u_c - F_r)^2, \tag{5.20}$$

where u_c is the particle velocity at the crest, computed from (5.17) by locating the position of the crest in x and computing $u(\zeta = H)$ at that x location. As the wave amplitude varies from 0 to its limiting value, in which $u_c = F_r$, the parameter ω_s goes from 0 to 1.

The speed of each wave was computed by letting an already permanent form solution propagate over a distance of around 500 times the water depth, recording the difference between the crest location x_c before and after this interval dt and computing

$$F_r = \frac{dx_c}{dt} \tag{5.21}$$

The exact location of the wave crest could not be obtained directly from the computations, since only by virtue of luck the crest was located exactly at one of the grid points. The location of the crest was determined by fitting a 4^{th} order polynomial to the free surface around the crest. The peak value and x location were then computed using the fitted polynomial. We used this same approach to compute $\tilde{u}$ and its x derivatives at and underneath the crest.

Figure 5.2 shows computations of the free surface elevation of half of a solitary with $F_r = 1.266$ for FN4, WKGS, GN1, GN2, GN3, and the exact solution. The three GN models are plotted with dotted lines, with GN1 and GN2 marked with labels. Notice that, of all models, GN3 has the best match with the exact solution. FN4 is also fairly close to the exact solution, but WKGS strongly overpredicts the wave height, and slightly underpredicts the tail. GN models tend to underpredict the height and overpredict the tail. Figure 5.3 shows the same model comparisons as in Figure 5.2, except for GN1 and GN2 whose solutions were not available. In

this case the maximum wave height is kept constant for all models. Again, GN3 has the best shape compared to the exact solution. WKGS solution compares better with the exact solution than in the previous case (F_r kept constant), but FN4 still compares better with the exact solution than does WKGS. Notice also the difference in wave speed F_r for each model. In Figure 5.4 the vertical profiles of the horizontal velocity are shown for the exact solution, FN4, and WKGS, for the waves shown in Figure 5.2, and it can be seen that the $O(\mu^4)$ model has a more accurate kinematics representation than the $O(\mu^2)$ model, confirming what we have already shown for linear theory. Unfortunately it was not possible to obtain GN vertical profiles, but it can be speculated that it would not be able to predict this property as accurately as the FN4, since it assumes the horizontal velocity to be only a 2^{nd} order polynomial.

Figure 5.5 shows the relationship between the speed and amplitude of a wide range of solitary waves for several models. Notice that once again GN3 has the closest solution to the exact one. FN4 slightly underpredicts the wave speed for a given amplitude, whereas the deviation in WKGS is of an order of magnitude higher. GN2 and especially GN1 overpredict the wave speed throughout the range tested. It is important to keep in mind that as the wave approach the limiting value, the crest becomes extremely sharp (with the limiting wave having a crest forming an angle of 120°), which makes it difficult for the finite difference scheme of FN4 to resolve the wave well near the crest, since the model has up to 5^{th} order derivatives in x.

Figure 5.6 shows computations of the parameter ω_s as a function of the wave speed. In this case, the FN4 model is the closest to the exact solution. This is not surprising if one recalls that ω_s is directly related to the horizontal fluid velocity at the crest, and that the FN4 has a 4^{th} order polynomial representation

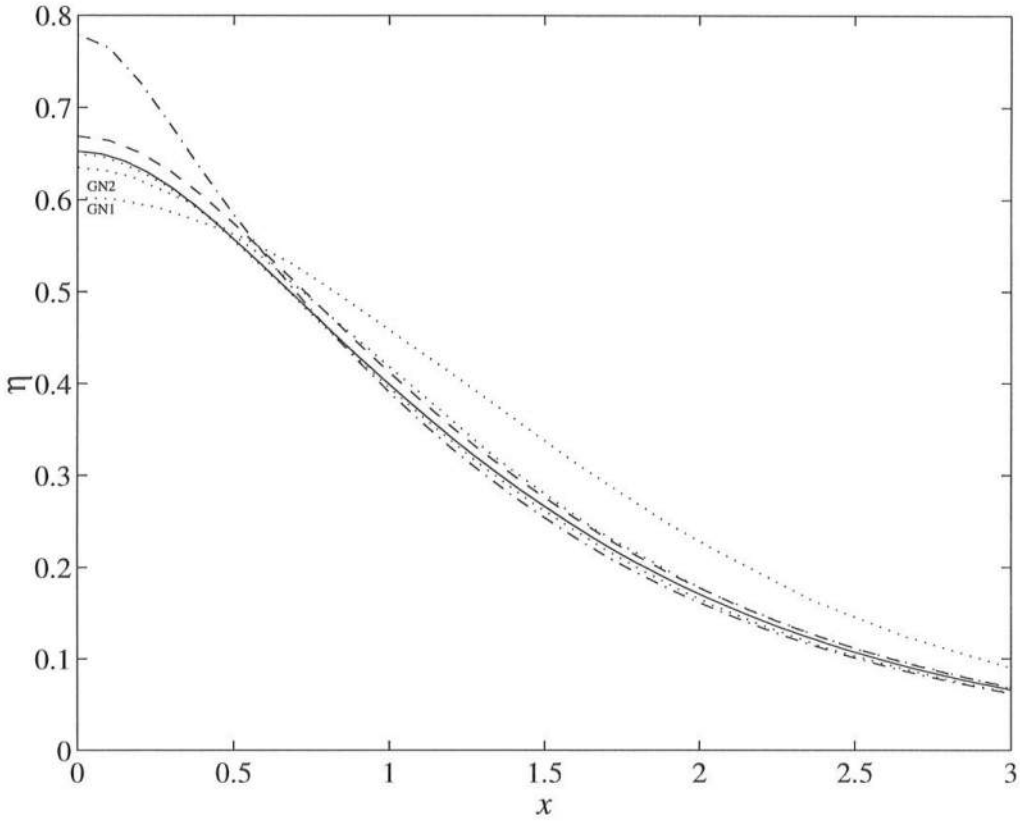

Figure 5.2: Shape of solitary waves with fixed $F_r = 1.266$. Exact (full), FN4 (dash), WKGS (dash-dot), GN1, GN2, GN3 (dot)

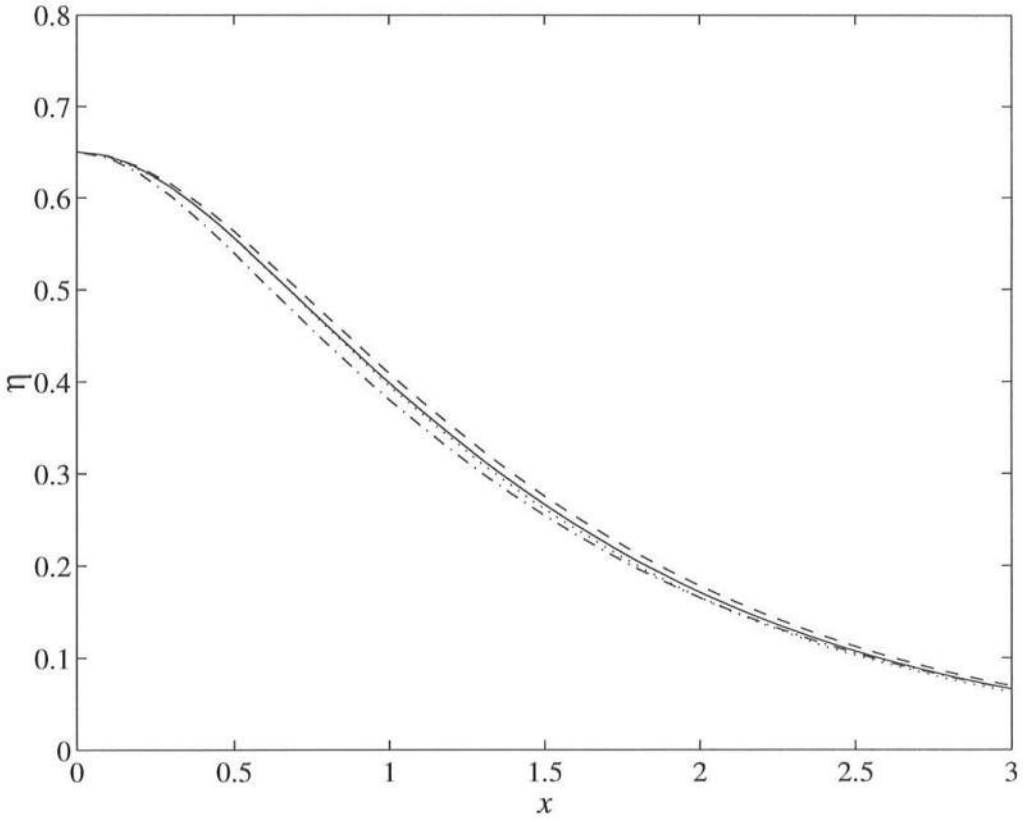

Figure 5.3: Shape of solitary waves with fixed amplitude $\eta_{max} = 0.65$. Exact: $F_r = 1.265$ (full), FN4: $F_r = 1.262$ (dash), WKGS: $F_r = 1.245$ (dash-dot), GN3: $F_r = 1.266$ (dot)

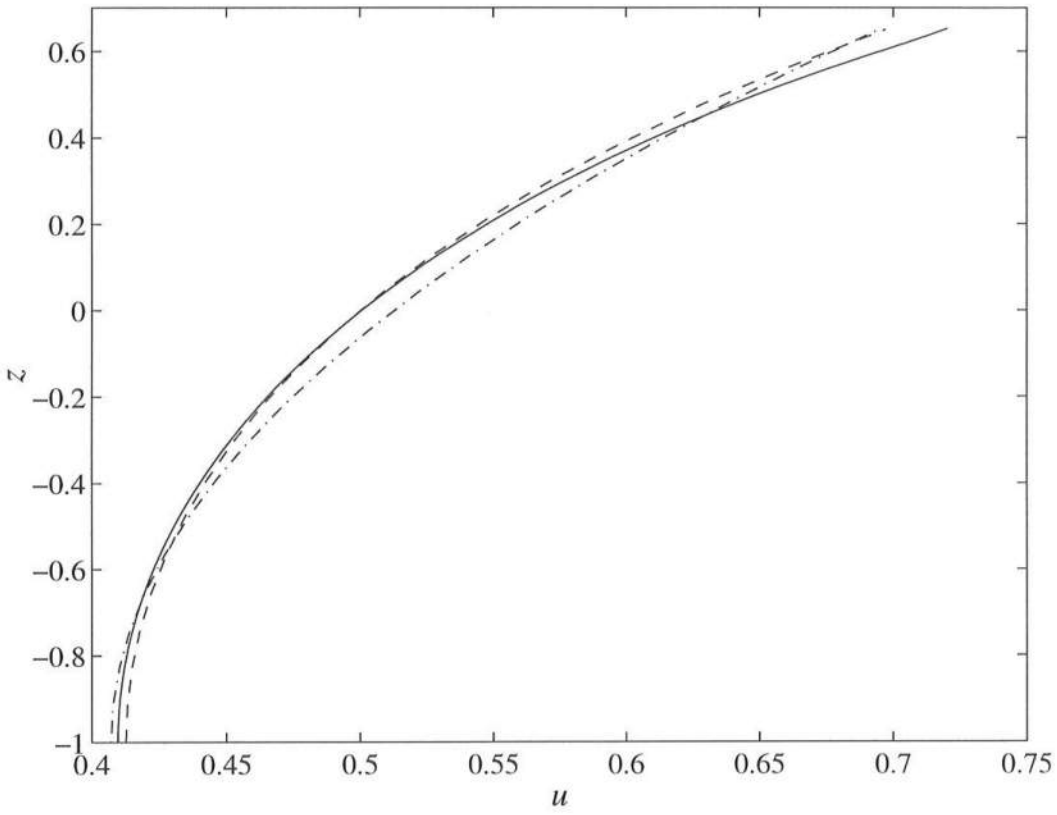

Figure 5.4: Vertical profile of horizontal velocity for solitary waves with amplitude $\eta_{max} = 0.65$. Exact (full), FN4 (dash-dot), WKGS (dash)

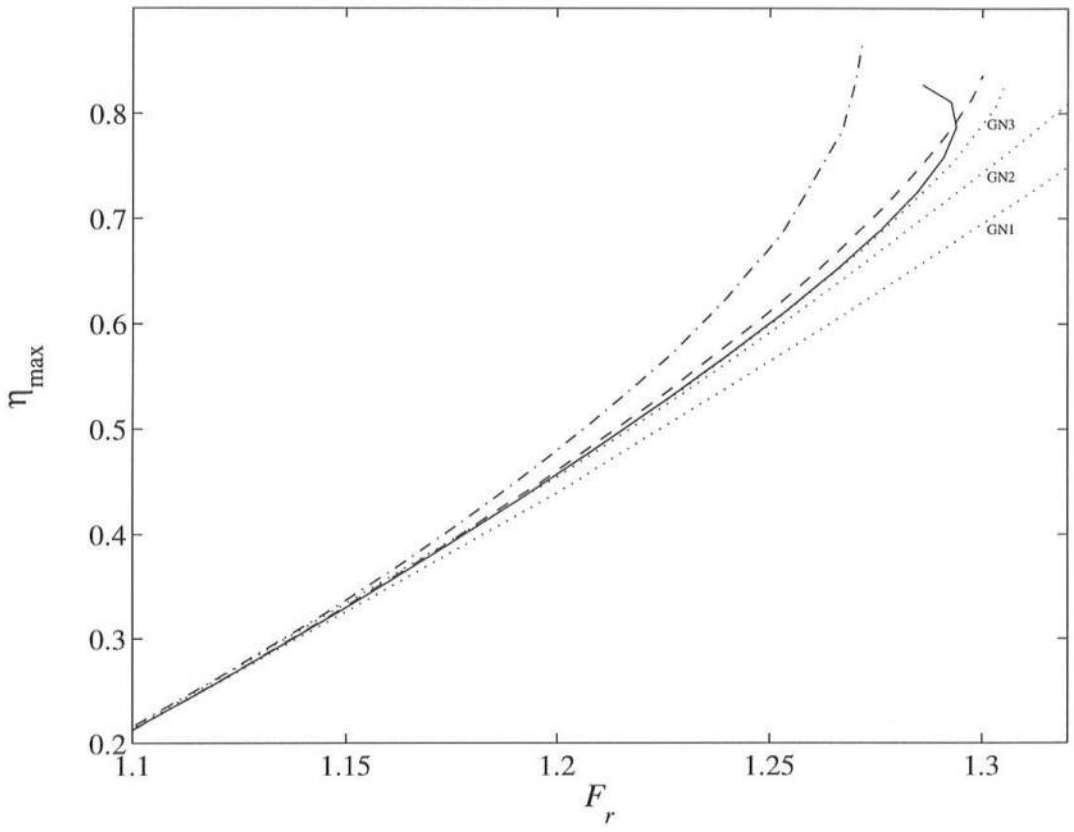

Figure 5.5: Solitary wave amplitude vs. phase speed. Exact (full), FN4 (dash), WKGS (dash-dot), GN1, GN2, GN3 (dot)

of the vertical profile of the horizontal velocity, whereas, as already observed, only a 2^{nd} order polynomial is assumed in both GN3 and WKGS. In the next figures, GN solutions were not available. Figures 5.7, 5.8, and 5.9 show plots of the mass, kinetic energy, and potential energy of solitary waves against the wave speed, for the exact solution, FN4, and WKGS. All three properties show a similar behavior to the wave amplitude (Figure 5.5) when plotted against F_r. In Figure 5.7, WKGS agrees with the exact solution better than FN4, but this is only a coincidence, as the overprediction of the wave crest counterbalance the underprediction of the

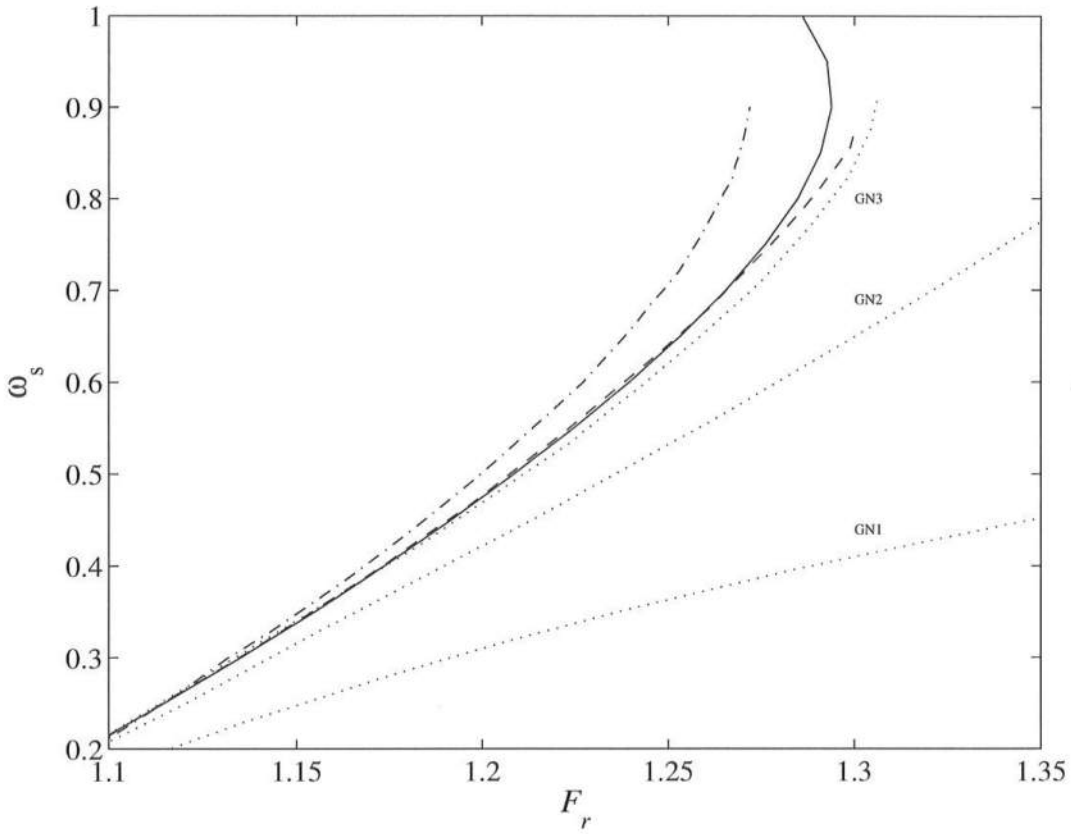

Figure 5.6: ω_s vs. phase speed for solitary waves. Exact (full), FN4 (dash), WKGS (dash-dot), GN1, GN2, GN3 (dot)

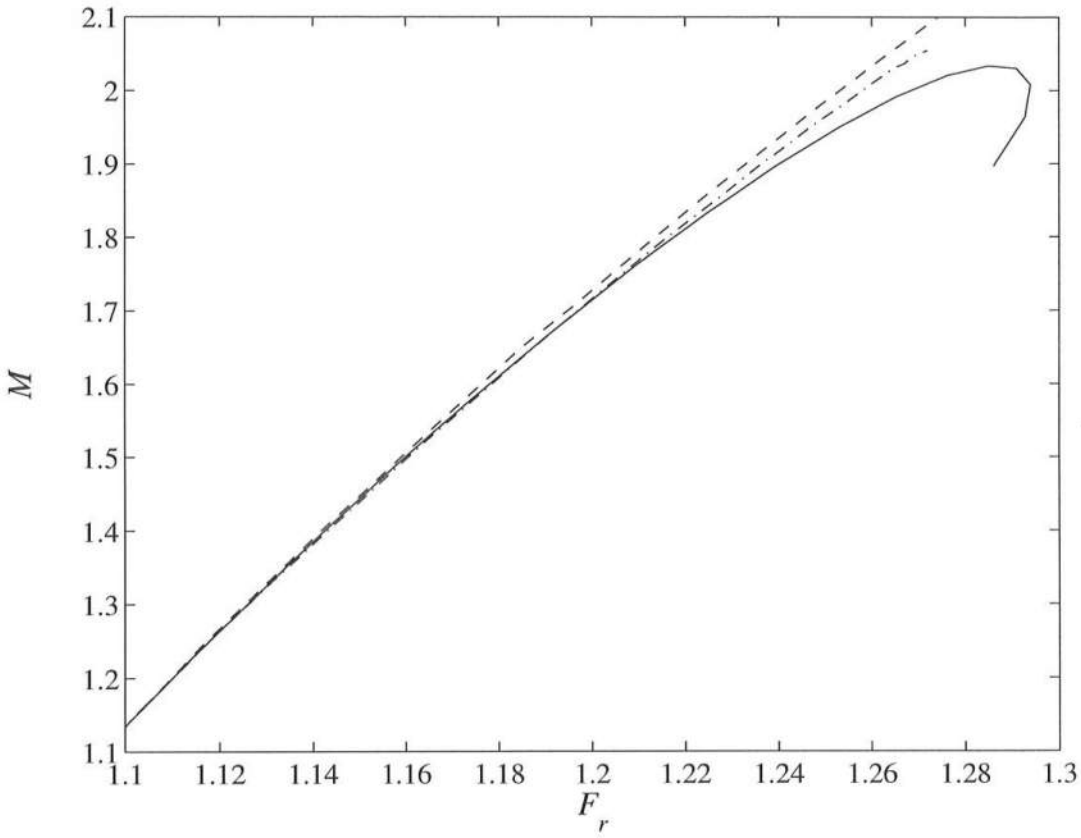

Figure 5.7: Mass vs. phase speed for solitary waves. Exact (full), FN4 (dash), WKGS (dash-dot)

wave tail. A similar effect happens with the kinetic energy (Figure 5.8), where the plots of the 2 models coincidently are on top of each other. The potential energy (Figure 5.9) calculations for model FN4 has better agreement to the exact solution than it has for the WKGS model, which confirms that the good agreement of WKGS in Figure 5.5 was by virtue of luck, since both the mass and the potential energy are only dependent of the free surface elevation.

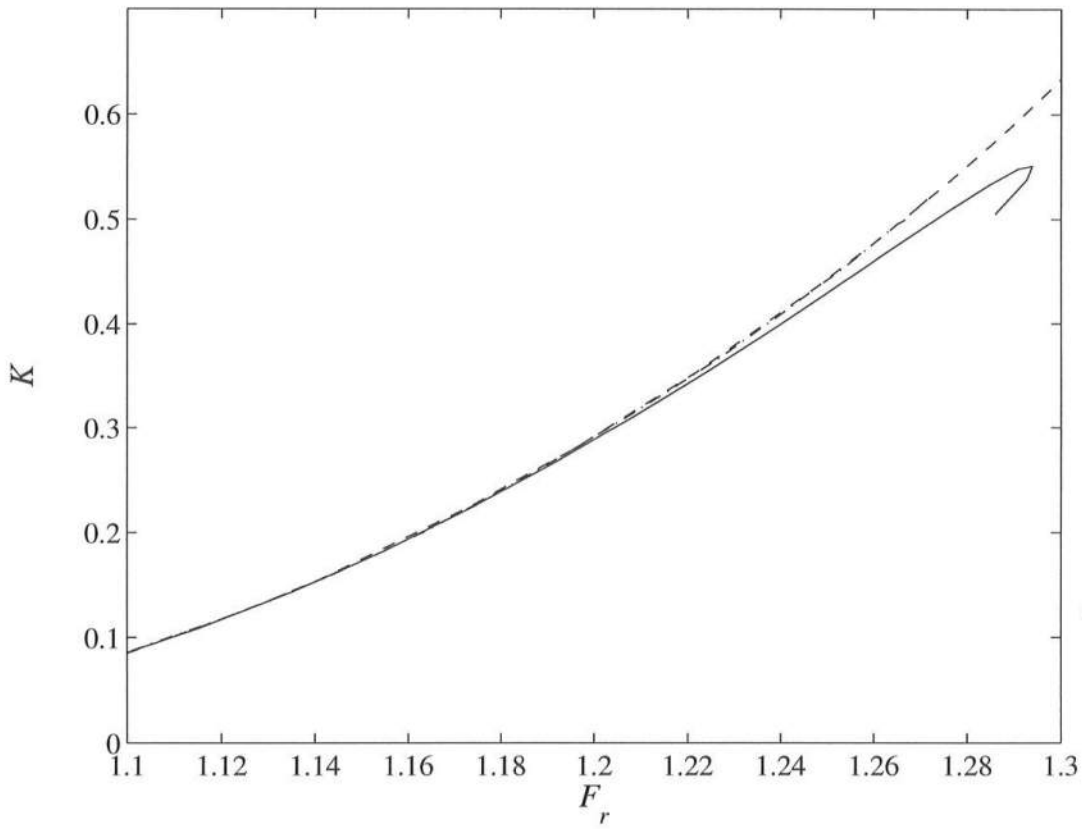

Figure 5.8: Kinetic energy vs. phase speed for solitary waves. Exact (full), FN4 (dash), WKGS (dash-dot)

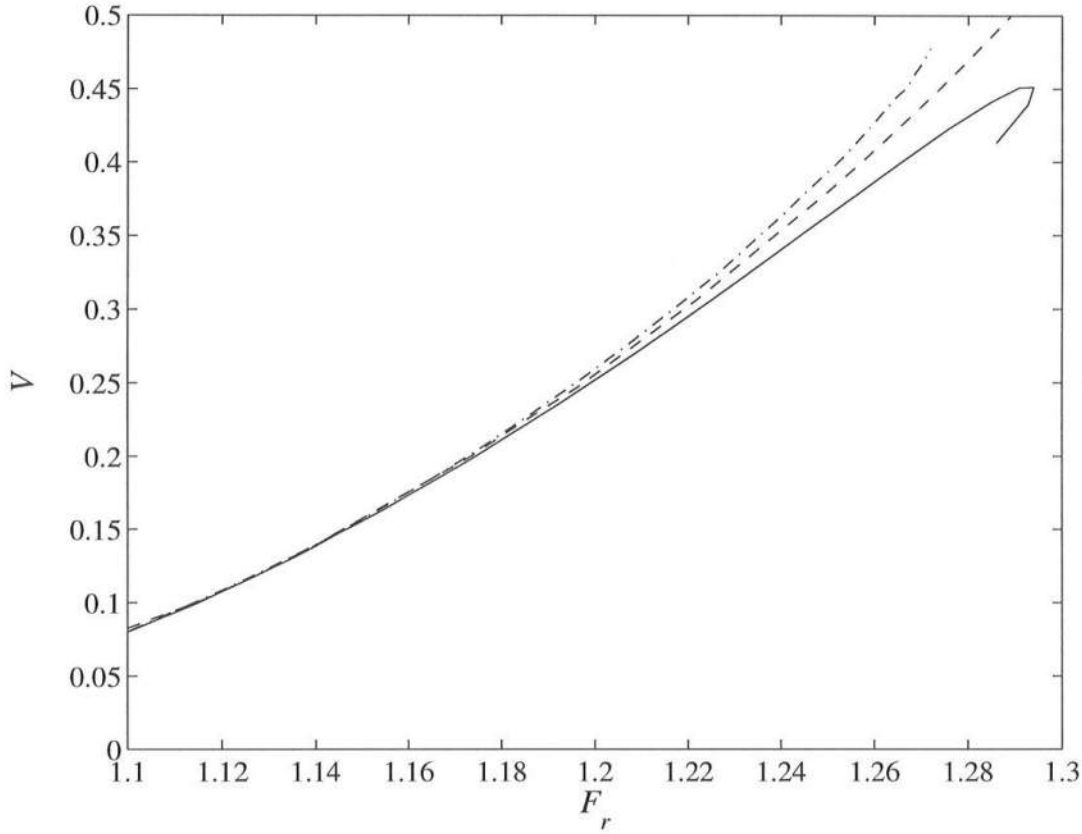

Figure 5.9: Potential energy vs. phase speed for solitary waves. Exact (full), FN4 (dash), WKGS (dash-dot)

5.2.1 Discussion

From Figures 5.1, 5.2, 5.3, 5.5, 5.6, it is clear that the FN4 model has a better asymptote (linear) agreement with the exact solution than does GN3, but, with the exception of the parameter ω_s (related to the velocity at the crest of the wave), in all other nonlinear properties, GN3 has a better agreement than FN4. This may seem somewhat surprising since GN3 approximates the horizontal velocity by a second order polynomial (two orders lower than the FN4 model) and the vertical velocity by a third order polynomial (same as the FN4 model), and a more careful study is needed to explain these discrepancies. Nevertheless, we make the following conjectures: FN4 satisfies mass conservation and all boundary conditions in an approximate sense, consistent with the level of approximation of the velocity field. GN3 satisfies mass conservation and the kinematic boundary conditions exactly. The coefficients for the velocity variable in FN4 are derived such that the linear dispersion relationship is extremely accurate, and no optimization is done considering that the free surface displacement is finite or including nonlinear terms. The advantage of this approach is that the model is simple in the sense that there is only one dependent variable describing the internal kinematics. For small amplitude waves the FN4 model is capable of extremely accurate results for a wide range of water depths, but as the nonlinear terms become more important, and the actual free surface deviates considerably from the still water level (for which the model was derived to perform its best), errors start to increase. On the other hand, GN3 is derived without any assumption, and no optimization is made "a priori". Rather, the coefficients for the velocity polynomial are derived by a minimization of the errors in the momentum equation over the entire actual water depth, which is changing with time. As a consequence, GN3 has three dependent variables describing each component of the velocity field, besides the free surface elevation. For a 2-dimensional problem, GN3 would have seven coupled evolution

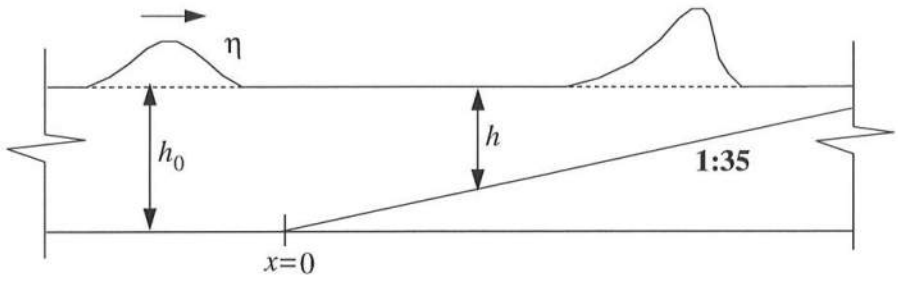

Figure 5.10: Sketch of shoaling solitary wave.

equations, whereas FN4 would have three.

5.3 Shoaling Solitary Wave

In this section we use permanent form solitary wave solutions for the FN4 and WKGS models as initial conditions for a more complex domain which includes a slope where the waves shoal and eventually break. The two Boussinesq models are compared to the Boundary Element Method (BEM) results using Grilli *et al.* (1989) formulation, which is a solution to the full boundary value problem, and can be regarded as an "exact solution" for the sake of comparison with Boussinesq models. Comparisons between WKGS, Nwogu (1993), and BEM for several cases can be found in Wei *et al.* (1995). Here, we concentrate in a single case of a wave with nondimensional amplitude $\eta_{max}/h_0 = 0.2$, where h_0 is the water depth before the slope $s = 1/35$. A sketch of the problem is illustrated in Figure 5.10.

Figure 5.11a shows the free surface elevation at 4 different times as the wave shoals on the slope. The nondimensional $x' = x/h_0$ has its origin at the toe of the slope, and the nondimensional time $t' = t(h_0/g)^{-1/2}$ has its origin at the instant the wave crest passes through $x' = 0$. This definition was used to synchronize the 3 models' results. Although the differences are subtle, it is possible to see that

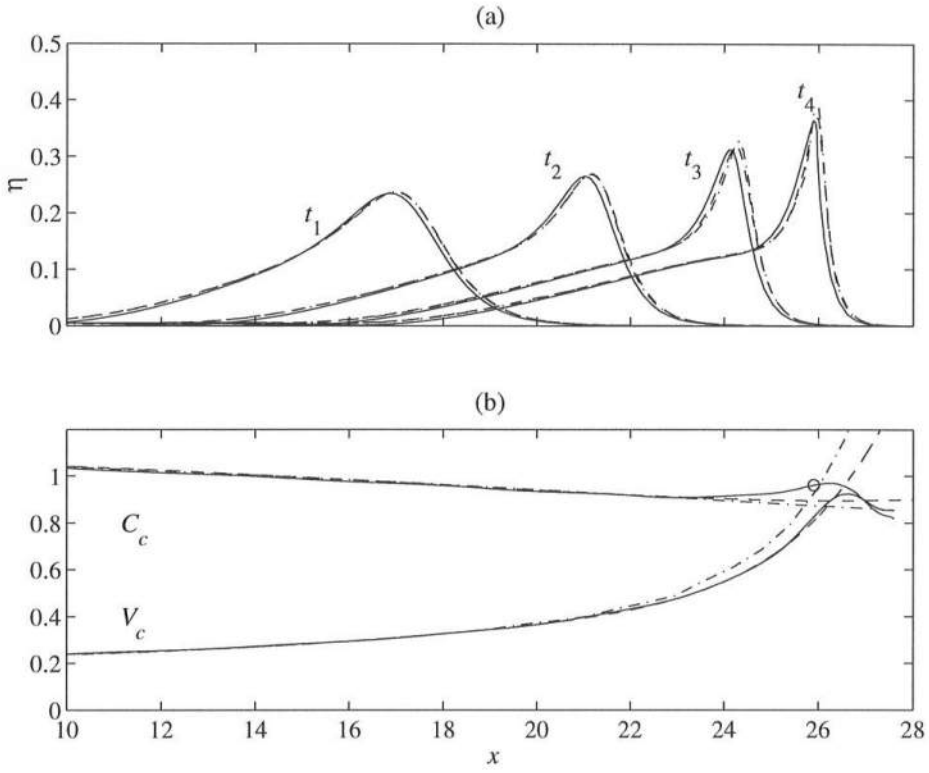

Figure 5.11: (a) Solitary wave shape at $t' = t_1 = 39.98$, $t_2 = 53.19$, $t_3 = 61.13$, $t_4 = 66.89$. (b) Crest speed (top curves) and fluid velocity (bottom curves). Circle denotes breaking point. BEM (full), FN4 (dash), WKGS (dash-dot)

the FN4 wave is closer to the BEM than the WKGS solution, in particular near the wave crest at t_3 and t_4 (shown in finer detail in Figure 5.12). Figure 5.11b shows computations of the crest speed and the fluid velocity at the crest. The location of breaking, defined as the point where a vertical tangent is formed at the face of the wave from the BEM, is also shown. The crest speed was computed by locating and recording the wave crest position x_c at every time step t, in a similar manner to what was done in the previous section, then computing the speed by

$$C_c = \frac{dx_c}{dt} \tag{5.22}$$

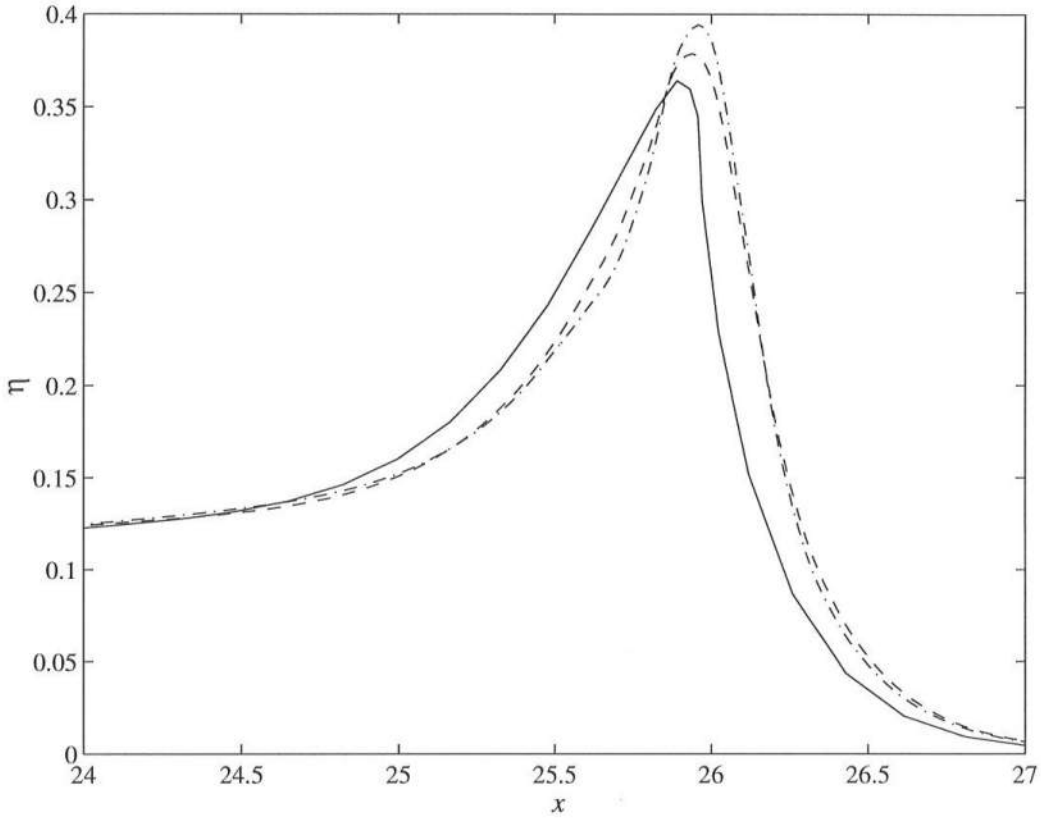

Figure 5.12: (a) Solitary wave shape at $t' = t_4 = 66.89$. BEM (full), FN4 (dash), WKGS (dash-dot)

Near breaking, the computations of C_c and V_c were smoothed with a 12^{th} order polynomial, since the estimations given by (5.22) exhibited some jitter. The model ran only up to the point where $C_c = V_c$, and the values beyond that point on Figure 5.11b are due to the polynomial extrapolation. The fluid velocity at the crest which, due to the presence of the slope, has both horizontal and vertical components, is given by:

$$V_c = \sqrt{u_c^2 + w_c^2}, \tag{5.23}$$

where u_c and w_c can be evaluated from the formula for the velocity profiles given below:

$$\begin{aligned}
u &= \tilde{u} + \mu^2 \left[(Ah - \zeta) f_{21_x} + 2h_x (Ah - \zeta) f_{22} + (Bh^2 - \zeta^2) f_{22_x} \right] \\
&+ \mu^4 \left[(Ah - \zeta) f_{41_x} + 2h_x (Ah - \zeta) f_{42} + (Bh^2 - \zeta^2) f_{42_x} \right. \\
&+ (Ah - \zeta) f_{43_x} + 2h_x (Ah - \zeta) f_{44} + (Bh^2 - \zeta^2) f_{44_x} \\
&+ 3h_x (Bh^2 - \zeta^2) f_{45} + (Ch^3 - \zeta^3) f_{45_x} \\
&+ \left. 4h_x (Ch^3 - \zeta^3) f_{46} + (Dh^4 - \zeta^4) f_{46_x} \right], \qquad (5.24) \\
w &= -\left[\mu^2 (f_{21} + 2\zeta f_{22}) + \mu^4 (f_{41} + 2\zeta f_{42} \right. \\
&+ \left. f_{43} + 2\zeta f_{44} + 3\zeta^2 f_{45} + 4\zeta^3 f_{46} \right) \Big]. \qquad (5.25)
\end{aligned}$$

where, again, nondimensional quantities are implied but primes have been omitted for notation simplicity. Model FN4 performs better than WKGS in predicting both the phase speed and the crest fluid velocity. Finally, vertical profiles of the horizontal velocity under the crest are shown in Figure 5.13 at three different locations, including one near the breaking point as predicted by BEM. As expected, the FN4 model performs better than the WKGS due to its better representation of the internal kinematics.

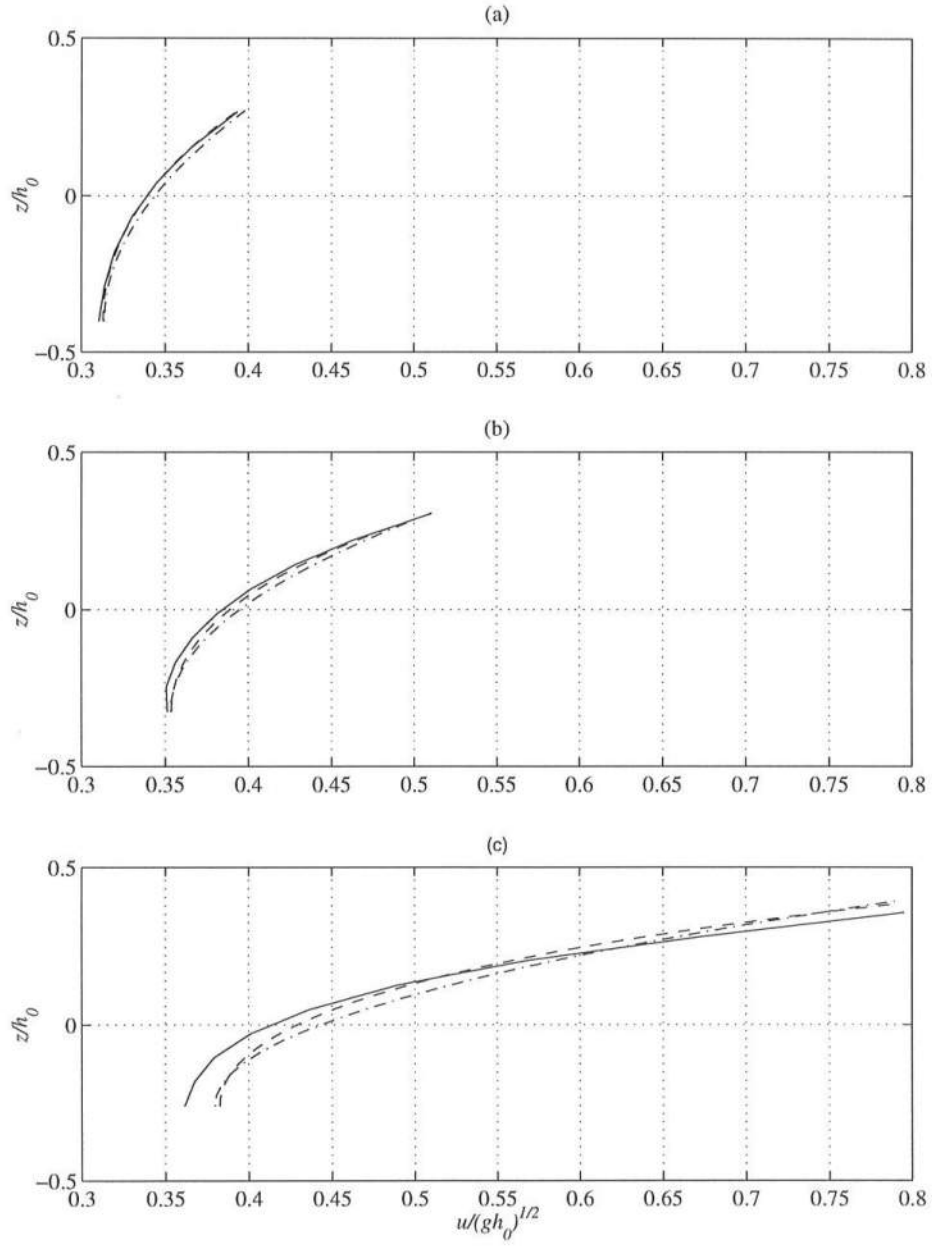

Figure 5.13: Vertical profile of horizontal velocity under the crest as it passes through (a) x'=20.96, (b) x'=23.63, (c) x'=25.91. BEM (full), FN4 (dash), WKGS (dash-dot)

Chapter 6

COMPARISONS WITH LABORATORY MEASUREMENTS

It is well known that regular waves decompose into higher frequency free waves as they propagate past a submerged bar, as shown in experimental work by Beji and Battjes (1993), Luth *et al.* (1994), and Ohyama *et al.* (1994). The basic mechanism is as follows: as the waves propagate onto the front slope of the bar, nonlinear interactions transfer energy from the leading wave component (primary wave) to higher harmonics, causing the wave to become steeper and also asymmetric (pitched forward). After the peak of the bar is reached (say no breaking occurs), and the bottom slope becomes negative (depth increases), the nonlinear coupling (forcing) of the higher harmonics with the fundamental wave becomes progressively weaker, and, from higher to lower harmonics, each of the Fourier components are released as free waves with their own bound higher harmonics. Of course, since the waves after the bar travel with different speeds, the process can be fairly complicated with some waves overtaking others, and involving nonlinear interactions. It is clear therefore that wave propagation over a submerged bar is a quite demanding test for Boussinesq-type models, as it requires that the model predict the nonlinear harmonic generation well, and also that the released shorter waves (behind the bar) have an accurate speed, which

may not happen even if the model predicts well the speed of the primary waves before they reach the bar.

Comparisons between several weakly nonlinear Boussinesq-type models and experimental data by Beji and Battjes (1993) and Luth *et al.* (1994) of waves propagating over a submerged bar were presented by Dingemans (1994). In general, the models performed relatively well for the longer, lower amplitude waves, but all were fairly inaccurate for the shorter, more nonlinear waves, especially behind the bar.

Comparisons between the extended Boussinesq model by Nwogu (1993), among other types of models, and experimental data, also for waves passing over a submerged bar, were presented by Ohyama *et al.* (1994), and the results were similar to the comparisons made by Dingemans (1994), that is, the model poorly predicted waves behind the shoal for the shorter, higher wave cases.

In this chapter we compare the FN4 model with three laboratory experimental data sets of regular waves propagating in a one-dimensional wave flume and over a submerged bar: Beji and Battjes (1993), Luth *et al.* (1994), and Ohyama *et al.* (1994). We also show comparisons of the WKGS model with the same data sets. The models' comparisons with the data are done in three different manners: plots of free surface time series at fixed locations, spatial plots of Fourier components of the time series, and a quantitative estimation of accuracy defined by:

$$d_i = 1 - \frac{\sum_{j=n_1}^{n_2} [y(j) - y_d(j)]^2}{\sum_{j=n_1}^{n_2} [|y(j) - \bar{y}_d| + |y_d(j) - \bar{y}_d|]^2} \tag{6.1}$$

where d_i is an index of agreement proposed by Wilmott (1981) for the i^{th} wave

gauge, and where n_1 and n_2 cover a full wave period in the time series.

$y_d(j)$ are the measured data to be compared with, $y(j)$ are the predicted values from the model, and $\bar{y_d}$ is the mean value of $y_d(j)$. A perfect agreement between data and model corresponds to $d_i = 1$, while a complete disagreement results in $d_i = 0$. In all the numerical simulations we used $\Delta x = 0.025m$ and kept the Courant number below 0.3. The sponge layer strength and width used were $S = 30$ and $x_L - x_S = 3L$, respectively. The width of the source function used was $W_s = L$, where L is the incident wave length. The details of the experiments and comparisons with the models are presented in the sections below.

6.1 The Delft Hydraulics Experiments

The experiments performed by Beji and Battjes (1993) and Luth *et al.* (1994) have the same geometric characteristics, except for the length scale in Luth *et al.* (1994), which is twice as large as in Beji and Battjes (1993). In Luth *et al.* (1994) all gauge locations used in Beji and Battjes (1993) were repeated, and another run of measurements was performed with the gauges at different locations. For the sake of consistency with the study by Dingemans (1994), we re-scale all measurements to the scales used in Beji and Battjes (1993). The layout of the experimental set-up with the locations of the measurement stations (to which we refer by their location, e.g. gauge $2.0m$, gauge $15.7m$, etc) and the geometry of the flume are illustrated in Figure 6.1. In the present work we use the data from Luth *et al.* (1994), since in that experiment active wave absorption was used at the end of the flume and both reflection and bound long waves were monitored during the experiment.

Three sets of data were collected using different incident wave conditions. We refer to these data sets as cases (a), (b), and (c). In case (b), wave breaking

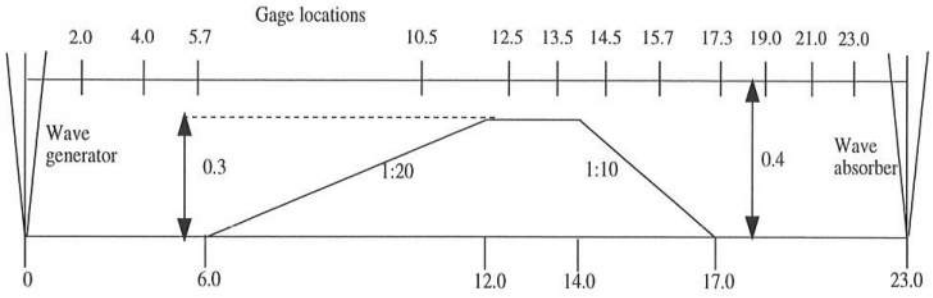

Figure 6.1: Sketch of wave flume of Delft experiments. All dimensions in (m)

Table 6.1: Incident wave characteristics for the Delft experiments.

	Case (a)	Case (c)
Wave amplitude (m)	0.01	0.0205
Wave period (s)	2.02	1.01
$\mu \equiv k_0 h_0$	0.67	1.69
$\delta \equiv a_0/h_0$	0.025	0.051

occurred on the crest of the shoal, and therefore these data were disregarded, since the present model does not include any breaking mechanism. The incident wave characteristics for cases (a) and (c) are given in Table 6.1. In all the cases, the data from gauges at $2.0m$ or $4.0m$ (remember these are 2 experiments combined) were used to synchronize the data with the models.

Figures 6.2 and 6.3 show comparisons with data from the Delft experiments for case (a) of the models WKGS and FN4. Notice that at the station $5.7m$ there is a phase mismatch in the data. This systematic error appears in all the cases for this gauge. Also, no data was available for the station $23.0m$. Both the FN4 and WKGS models perform quite well for all the gauges up to the crest of the bar, but as the waves pass the back slope of the bar, the WKGS model shows some discrepancies with the data. This is due to the aforementioned decoupling of the

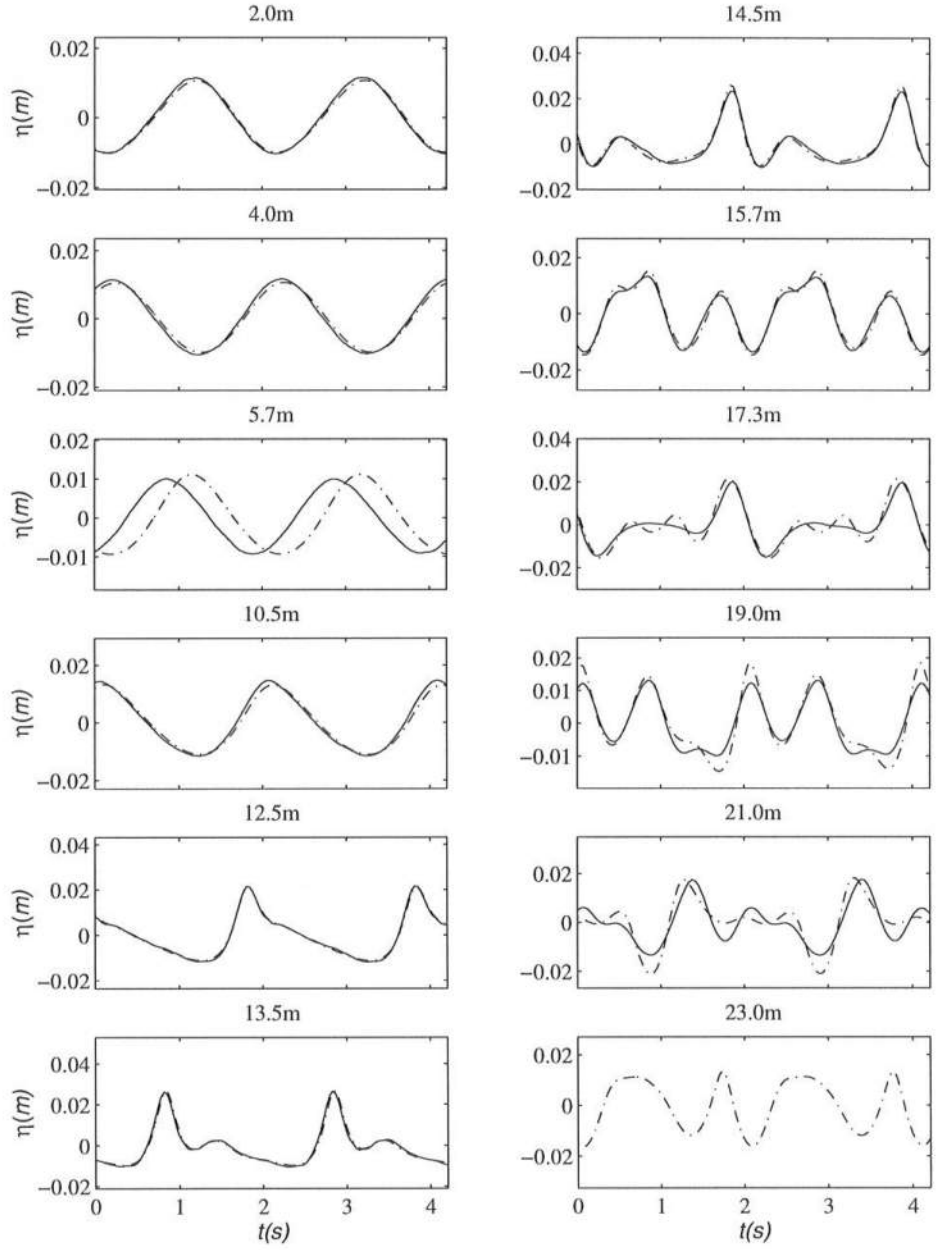

Figure 6.2: Comparisons of free surface displacement with case (a) of Delft experimental data at several gauge locations. WKGS (dash-dot), data (solid).

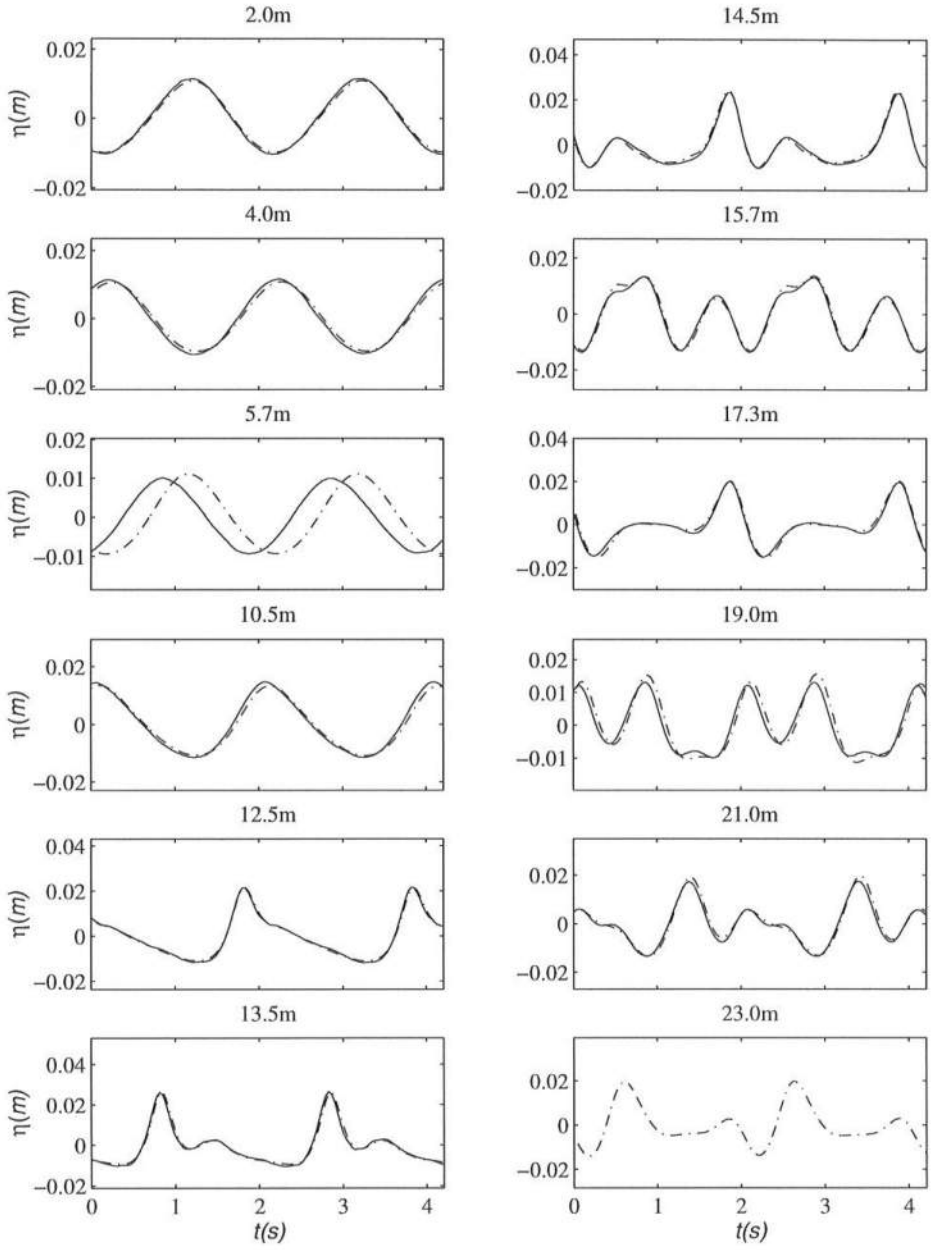

Figure 6.3: Comparisons of free surface displacement with case (a) of Delft experimental data at several gauge locations. FN4 (dash-dot), data (solid).

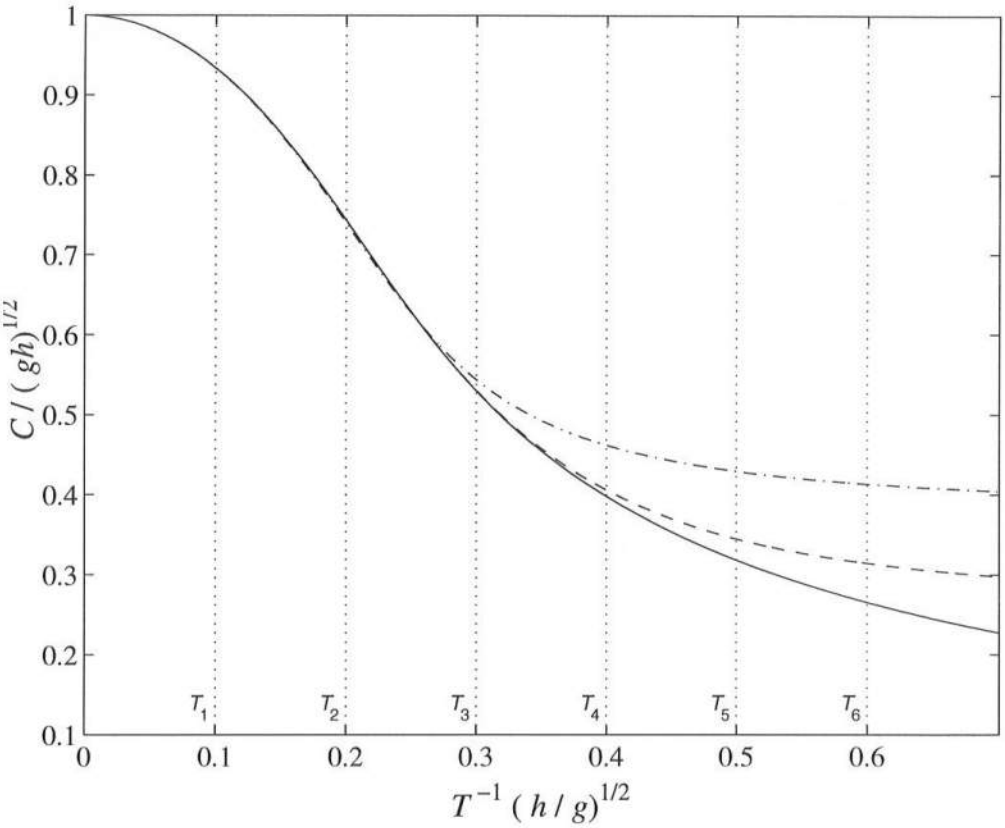

Figure 6.4: Linear dispersion relationship as (nondimensional) wave speed vs. wave frequency. Present Model (dash), WKGS (dash-dot), exact (solid). Dotted vertical lines are waves with periods $T_n = (2.02/n)s$.

higher harmonics from the primary longer wave which are released as free waves propagating with a larger value of μ which are more susceptible to inaccuracies. The FN4 model remains quite accurate even for the gauges located after the bar. To illustrate the inaccuracies due to higher harmonic decoupling, Figure 6.4 shows an alternative representation of the linear dispersion relationship where the nondimensional wave speed is plotted against the wave frequency. The vertical dotted lines indicate the location of the frequency of the fundamental wave in case (a), of which the period is $T_1 = 2.02s$, and its harmonics with periods $T_2 = T_1/2$,

$T_3 = T_1/3$, etc. Notice that the phase speed error in the primary wave (T_1) is small for both the FN4 and WKGS models. As the bound waves are released as free waves they travel with their own speed, which, in the linear limit, are represented by the intersection of the vertical lines T_2, T_3, etc. with each model's dispersion curve. Notice that the errors in the speed of the released higher harmonics starting from T_3 for WKGS are considerably larger than for the FN4 model.

Similarly to Figures 6.2 and 6.3, Figure 6.5 shows plots for the WN4 model (this is the present model, but with the assumption $O(\delta) = O(\mu^2)$ and neglecting terms of $O(\delta^2\mu^2, \delta\mu^4, ...)$. Apart from slight phase differences, the comparison is about as good as the FN4 model, which indicates that for this case, the improvement in the dispersion effects of the FN4 and WN4 models over the WKGS model is more important than the fully nonlinear effects accounted for in WKGS and FN4, but not in WN4.

Figures 6.6, 6.7 and 6.8 are analogous to Figures 6.2, 6.3 and 6.5, but for case (c) (see Table 6.1). Notice that in this case the incident wave has twice the amplitude and about 2/5 of the wavelength of case (a). Before the waves reach the back slope of the bar, FN4 and WKGS perform quite similarly, although some phase differences are apparent. Model WN4 does not perform as well in this case due to its weak nonlinearity assumption. As the waves pass over the bar, the higher harmonic decomposition combined with nonlinear effects are strong enough in this case to make the three models give very different results, with FN4 being the most accurate, giving very good agreement except for slight phase differences. Notice that for this case, WN4 does not perform nearly as well as FN4, and also qualitatively worse than the WKGS (accurate to $O(\mu^2)$, but fully nonlinear) for all gauges up $15.7m$. This result is a strong indication that the improvement in linear dispersion is not always more important than the fully nonlinear effects,

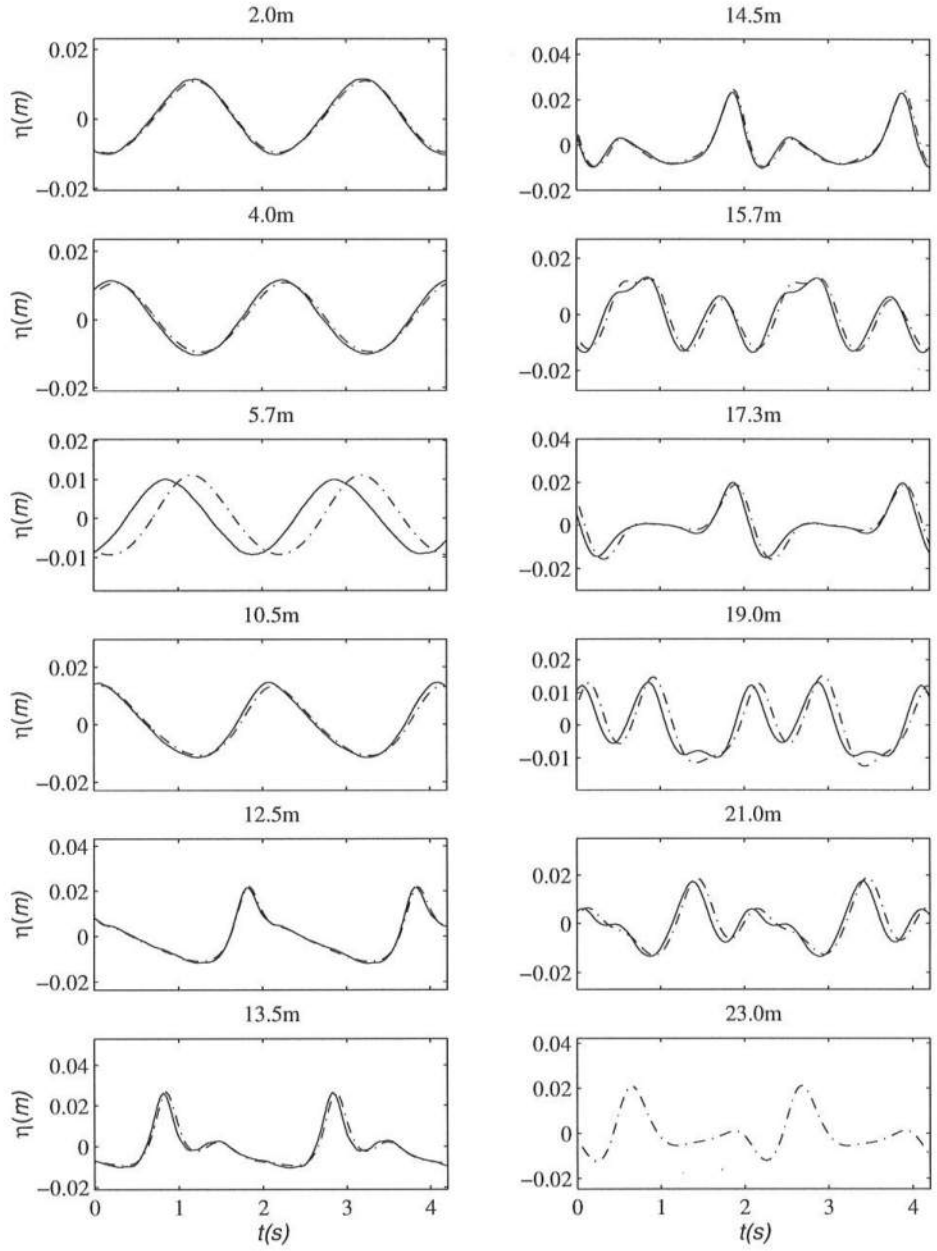

Figure 6.5: Comparisons of free surface displacement with case (a) of Delft experimental data at several gauge locations. WN4 (dash-dot), data (solid).

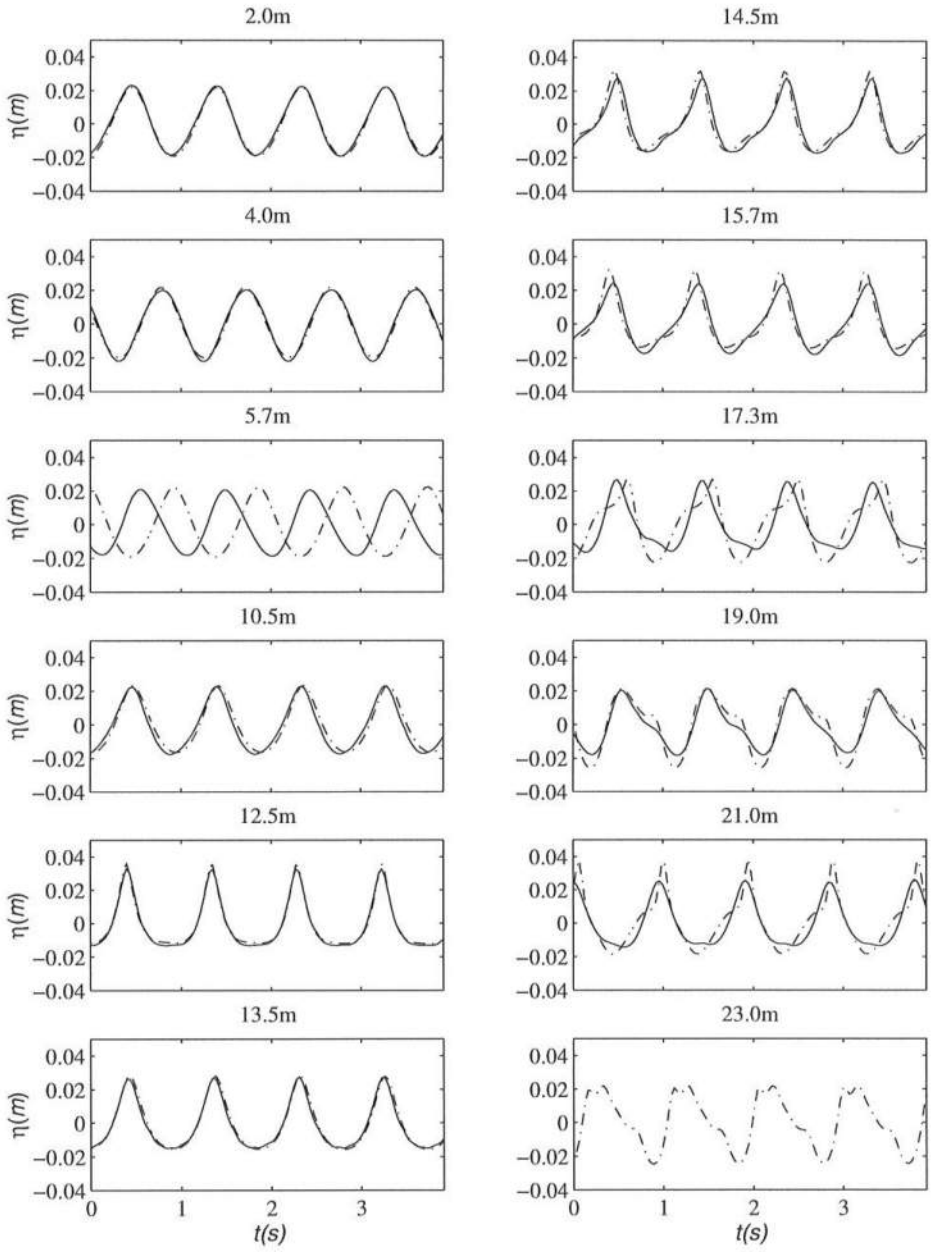

Figure 6.6: Comparisons of free surface displacement with case (c) of Delft experimental data at several gauge locations. WKGS (dash-dot), data (solid).

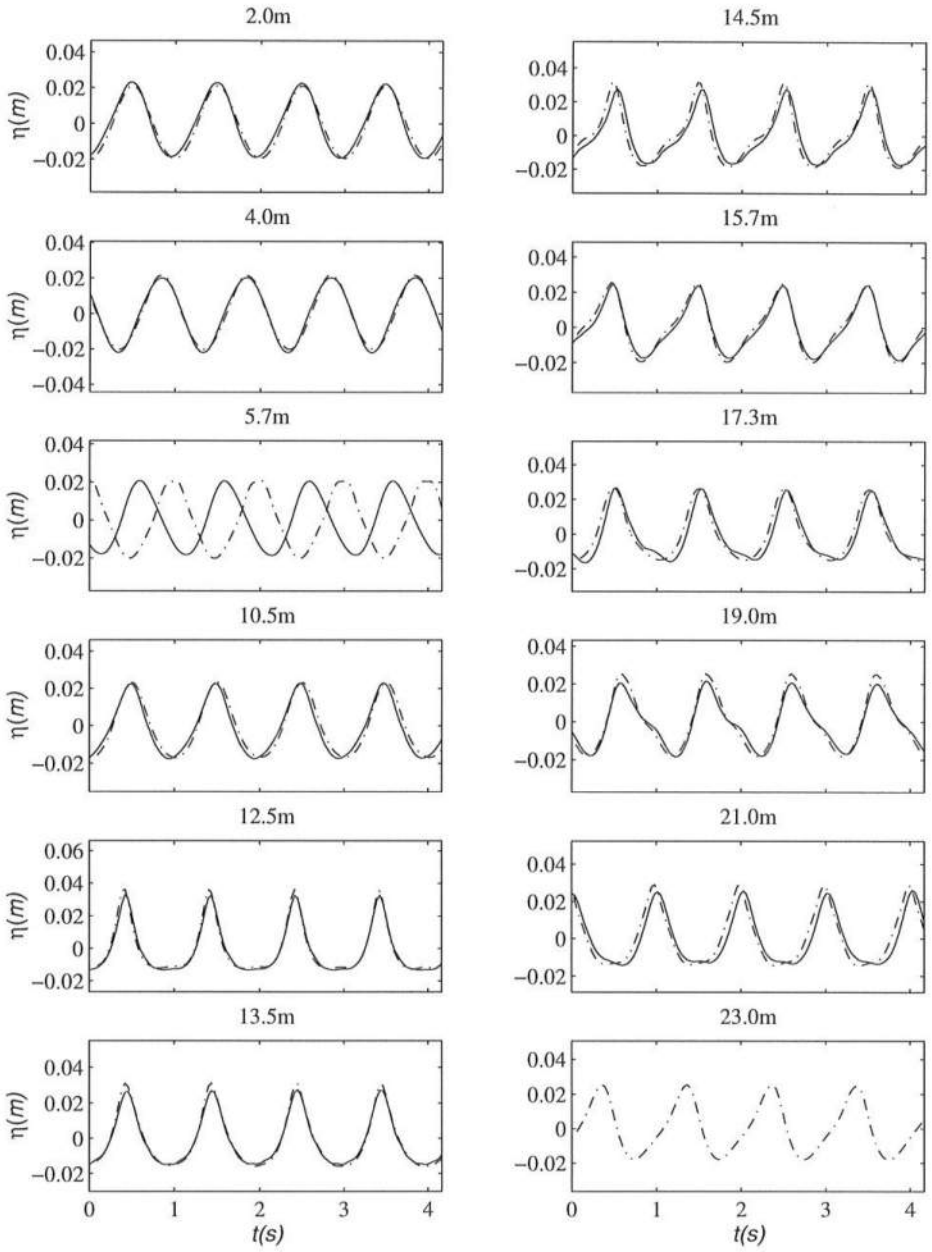

Figure 6.7: Comparisons of free surface displacement with case (c) of Delft experimental data at several gauge locations. FN4 (dash-dot), data (solid).

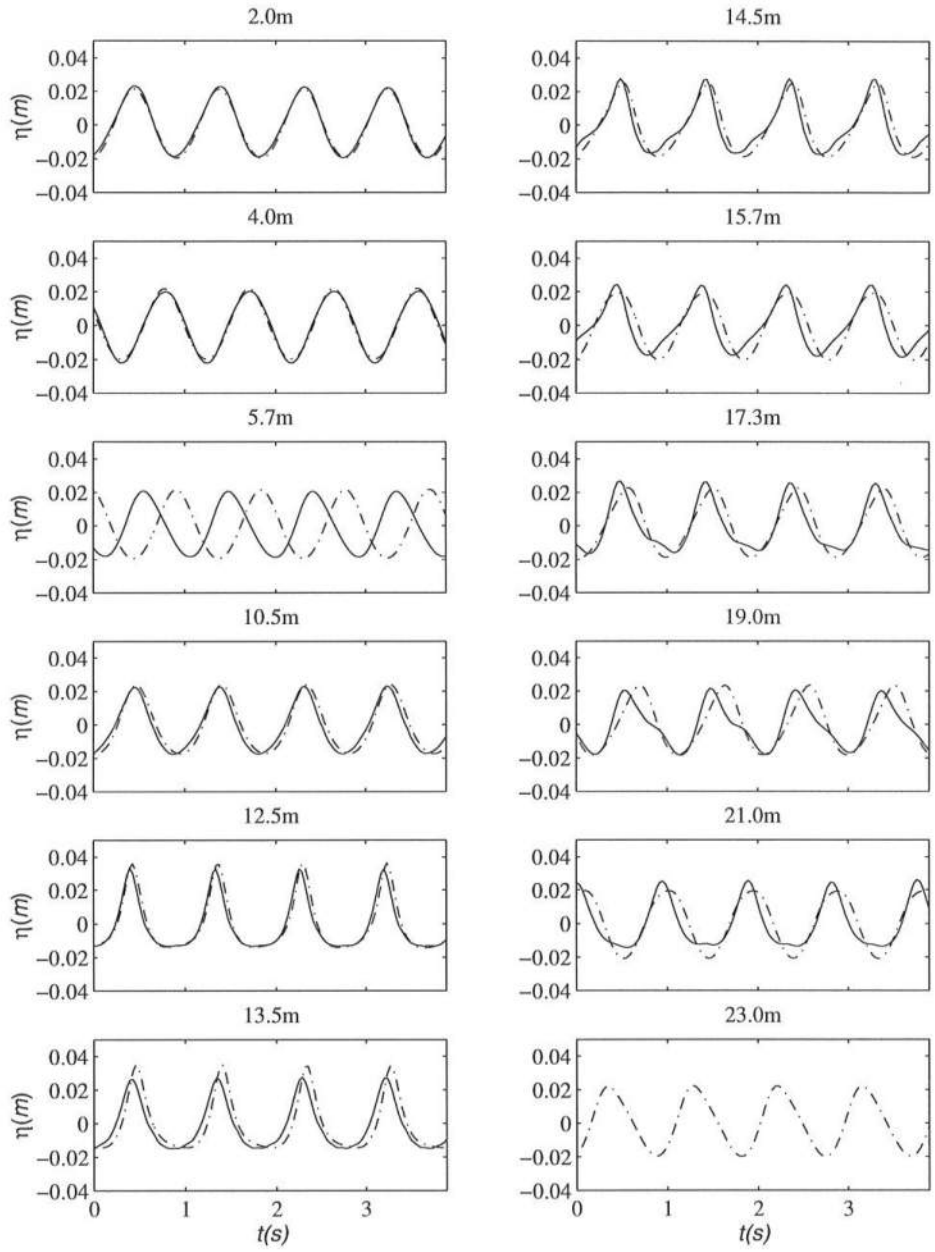

Figure 6.8: Comparisons of free surface displacement with case (c) of Delft experimental data at several gauge locations. WN4 (dash-dot), data (solid).

contrary to the generalizing conclusion of Dingemans (1994). Referring back to Figure 6.4, again, after the waves pass the bar, the higher harmonics are released as free waves. For case (c) the primary (incident) wave is indicated by the vertical dotted line labeled T_2, and its second and third harmonics are represented by the even indexes, that is, T_4 and T_6 respectively. Notice that the error in the speed of the primary wave is negligible for the WKGS model. In the second harmonic (T_4) the error for WKGS is fairly high, and for FN4, although not negligible, is considerably smaller, and the same being the case of the released third harmonic (T_6).

Figure 6.9 shows comparisons of the absolute value of the amplitudes of the Fourier transform of one wave period of the time series, between both FN4 and WKGS, and the data points at each gauge location for both cases (a) and (c). Figure 6.10 shows similar plots for FN4 and WN4, where FN4 results are identical to those in Figure 6.9. Also shown are snapshots of the free surface elevation and the position of the bar (out of scale). In both cases (a) and (c), the WKGS model tends to overpredict the higher harmonics after the crest of the bar. For case (a) the FN4 and WN4 models give very similar results, with some slight underpredictions by WN4 of the amplitudes of the released third and fourth harmonics after the bar crest. In case (c) WN4's inability to generate higher harmonics accurately due to the weak nonlinearity assumption is evident in the underprediction of the decomposed higher harmonics. Notice the modulation present in the fundamental wave before the bar, shown by all three models, caused by partial wave reflection from the front of the bar. Notice also that for case (c) the FN4 model slightly overpredicts the third and fourth modes around the toe of the front face of the bar. This is due to numerical error introduced by the high order derivative terms, which are undefined functions at that location. When necessary, the solution was filtered (see Chapter 4) to avoid high frequency contamination

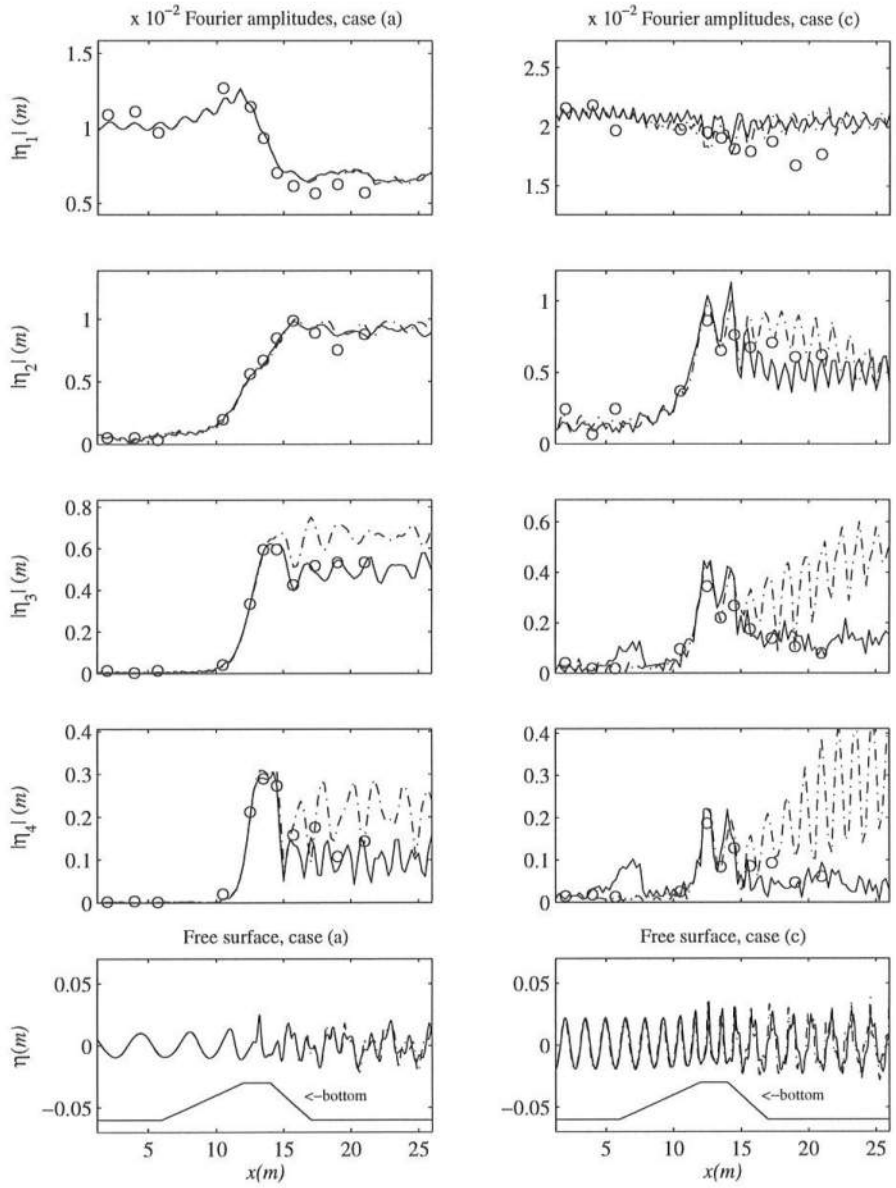

Figure 6.9: Comparisons of the spatial variation of the Fourier components of the free surface displacement with cases (a) and (c) of Delft experimental data. Bottom panels show the free surface elevation. FN4 (solid), WKGS (dash-dot), data (circles).

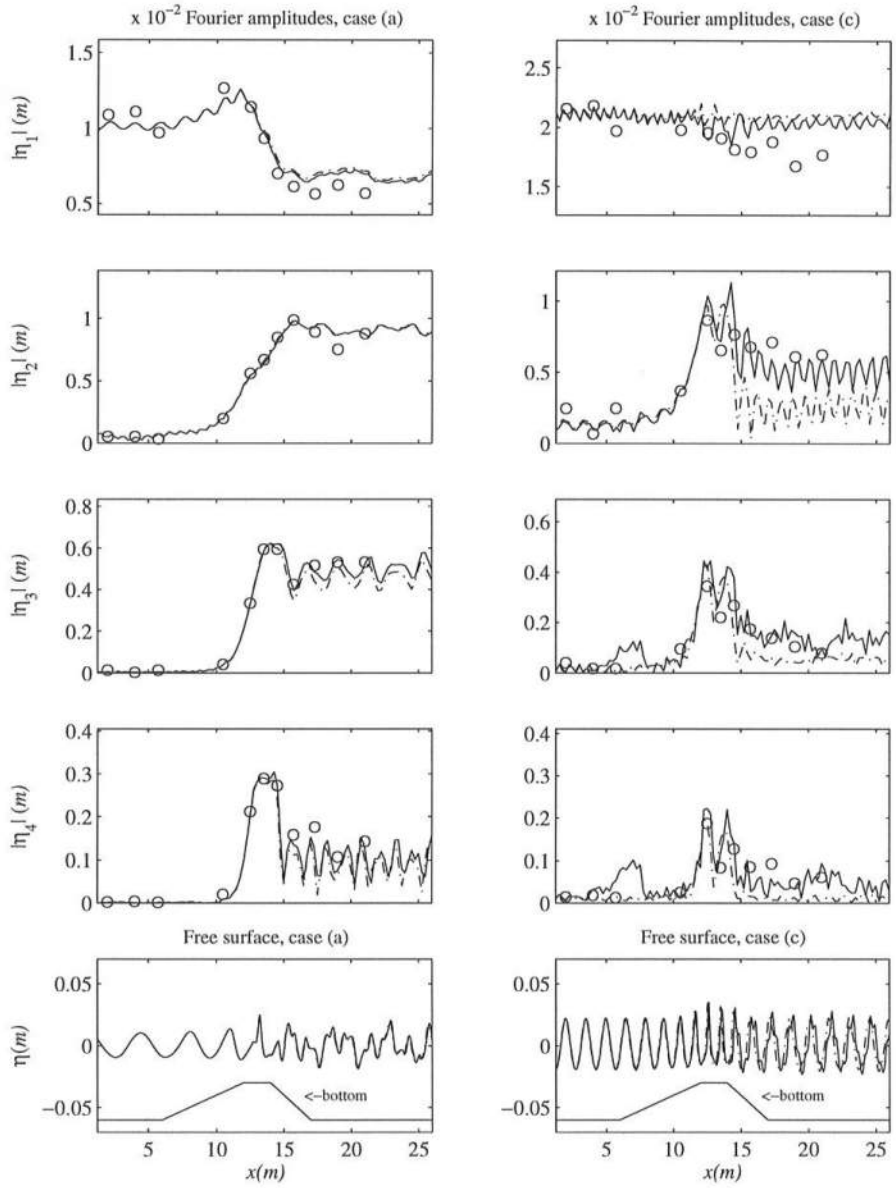

Figure 6.10: Comparisons of the spatial variation of the Fourier components of the free surface displacement with cases (a) and (c) of Delft experimental data. Bottom panels show the free surface elevation. FN4 (solid), WN4 (dash-dot), data (circles).

Table 6.2: Index of agreement d_i.

Gauge Location (m)	case (a)			case (c)		
	WKGS	FN4	WN4	WKGS	FN4	WN4
2.0	0.998	0.998	0.998	0.997	0.996	0.998
4.0	0.996	0.996	0.996	0.997	0.997	0.984
10.5	0.995	0.995	0.995	0.982	0.986	0.997
12.5	0.999	0.999	0.998	0.997	0.995	0.927
13.5	0.996	0.995	0.987	0.996	0.996	0.990
14.5	0.995	0.997	0.993	0.979	0.971	0.883
15.7	0.995	0.996	0.980	0.973	0.993	0.977
17.3	0.975	0.995	0.972	0.880	0.973	0.934
19.0	0.973	0.982	0.943	0.968	0.987	0.970
21.0	0.927	0.993	0.962	0.948	0.965	0.931

problems. In general, as in the case of the time series plots, the FN4 agrees with the data much better than WKGS and than WN4 for case (c).

Table 6.2 shows the index of agreement d_i defined by (6.1) of the models FN4, WN4, and WKGS, with both cases (a) and (c) of the Delft experiments for all gauges except $5.7m$ and $23.0m$. Of course, the differences in d_i between the models should only have significance when they are larger than d_i for the incident wave (gauges $2.0m$ and $4.0m$). The results confirm that the best performance is from the FN4 model, with only one case where WKGS gave a slightly better result (case (c), gauge $14.5m$) due to a slightly larger phase mismatch in FN4. It is clear that the WKGS model outperforms the WN4 model around the bar crest (gauges $12.5m$ through $14.5m$), but as the waves reach deeper water (importance of nonlinearity and dispersion switch), WKGS loses accuracy. Although WN4 has much more accurate dispersion relationship in deeper water than WKGS, since it was not capable of generating higher harmonics properly while the waves were shoaling, the overall solution becomes inaccurate after the bar. This confirms the

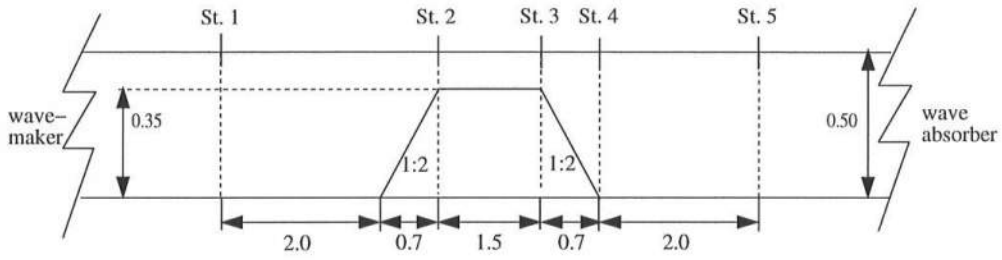

Figure 6.11: Sketch of wave flume of the Ohyama experiment. All dimensions in (m)

importance of the full-nonlinearity assumption made in the WKGS derivation but not in the WN4.

6.2 The Ohyama Experiment

In this section we show comparisons of the models FN4 and WKGS model with the experiment by Ohyama *et al.* (1994) (referred here as simply the Ohyama experiment). Computations with the WN4 model were not performed for this case. A sketch of the wave flume with the gauge locations is shown in Figure 6.11. We now summarize the experimental setup. The wave flume is $65m$ long and $1.0m$ wide. The total depth of the flume is $1.6m$. The location of the center of the bar was $28.3m$ from the piston-type wavemaker. All other relevant dimensions can be seen in Figure 6.11. The measurements were performed before the point when waves reflected from the bar reached the wavemaker. At the right end of the flume, waves were absorbed by the presence of coarse materials to dissipate the energy. A total of six tests were performed with three different incident wave periods $(1.34s,2.01s,2.68s)$ each for two different wave amplitudes $(0.0125m,0.025m)$. No wave breaking occurred in any of the tests. The data was obtained by digitization of the plots (performed by Andrew Kennedy) from the original article. The only

Table 6.3: Incident wave characteristics for the Ohyama experiment.

	Case (2)	Case (4)	Case (6)
Wave amplitude (m)	0.025	0.025	0.025
Wave period (s)	1.341	2.012	2.683
$\mu \equiv kh$	1.299	0.769	0.555
$\delta \equiv a_0/h_0$	0.050	0.050	0.050

time series available for comparisons were the ones at station 3 and 5, for all three wave periods, and the highest of the two amplitudes ($0.025m$). Fourier amplitudes were available for the same wave conditions but at all measurement stations. Time series were synchronized at station 3. We refer to the three tests as cases (2), (4), and (6), as in Ohyama *et al.* (1994). The incident wave conditions are summarized in Table 6.3. The incident wave conditions are similar in the Ohyama and Delft experiments. The major difference between the two experiments is that the bar in the Ohyama experiment is much shorter and with much steeper slopes than the one in the Delft experiments, more reminiscent of a submerged rubble mound structure. The steep slopes add extra difficulty for the models' performance, since: (i) the models' dispersion properties are optimized assuming constant depth; (ii) the assumption that the vertical velocity is $O(\mu^2)$ times the horizontal velocity is violated at steep slopes. Smoothing of the corners of the bar, besides filtering every 100 time steps was necessary to prevent spurious high frequency noise to contaminate the solutions. To smooth the corners of the bar we applied a 3-point average by Shapiro (1970) five times. Since the waves are progressively longer from case (2) through (6), we expect that the Boussinesq models will perform best in case (6), and worst in case (2). We also expect higher mismatches between models and data at station 5 than at station 3, due to increasing errors in the phase of the decomposed higher frequency bound waves as they reach the deeper water behind the bar.

Figures 6.12, 6.13, and 6.14 show comparisons of the FN4 and WKGS models with data for cases (2), (4), and (6), respectively. Notice that for cases (2) and (4) the FN4 model shows a mismatch in the phase speed at station 5, and an underprediction of the wave crests and troughs, an indication that even the fully nonlinear, $O(\mu^4)$ model has limited ability to predict waves past a submerged bar with very steep slopes, if the waves are short enough. For case (6) the FN4 model agrees very well with the data. For all three cases, the WKGS model has poor qualitative agreement with the data at station 5, mostly due to phase errors and overprediction of higher harmonics behind the bar.

Figures 6.15, 6.16, and 6.17 show comparisons of the Fourier amplitudes along the flume between both FN4 and WKGS, and the data points at each station for cases (2), (4), and (6) respectively. In all cases, the models predict well the Fourier amplitudes before the back face of the bar. For case (2), WKGS gives slightly better prediction of the second harmonic at stations 4 and 5 than FN4, but once again strongly overpredicts the third and fourth harmonics at those stations. For case (4), the FN4 model gives better prediction than WKGS for all but the third harmonic, which WKGS agrees slightly better with the data. For case (6), both models agree reasonably well with the data, with FN4 having a better prediction of the third harmonic at station 5 and the WKGS model matching the fourth fourth harmonic slightly better at that same station. For this case, the deviations from the data in the time series computed by WKGS at station 5 are probably due to phase errors, which is not detected by the Fourier amplitudes comparisons.

Similarly to the case of the Delft experiment, table 6.4 shows the index of agreement between the models WKGS and FN4, and the data from the Ohyama experiment for cases (2), (4), and (6), stations 3 and 5. Notice that for cases (2)

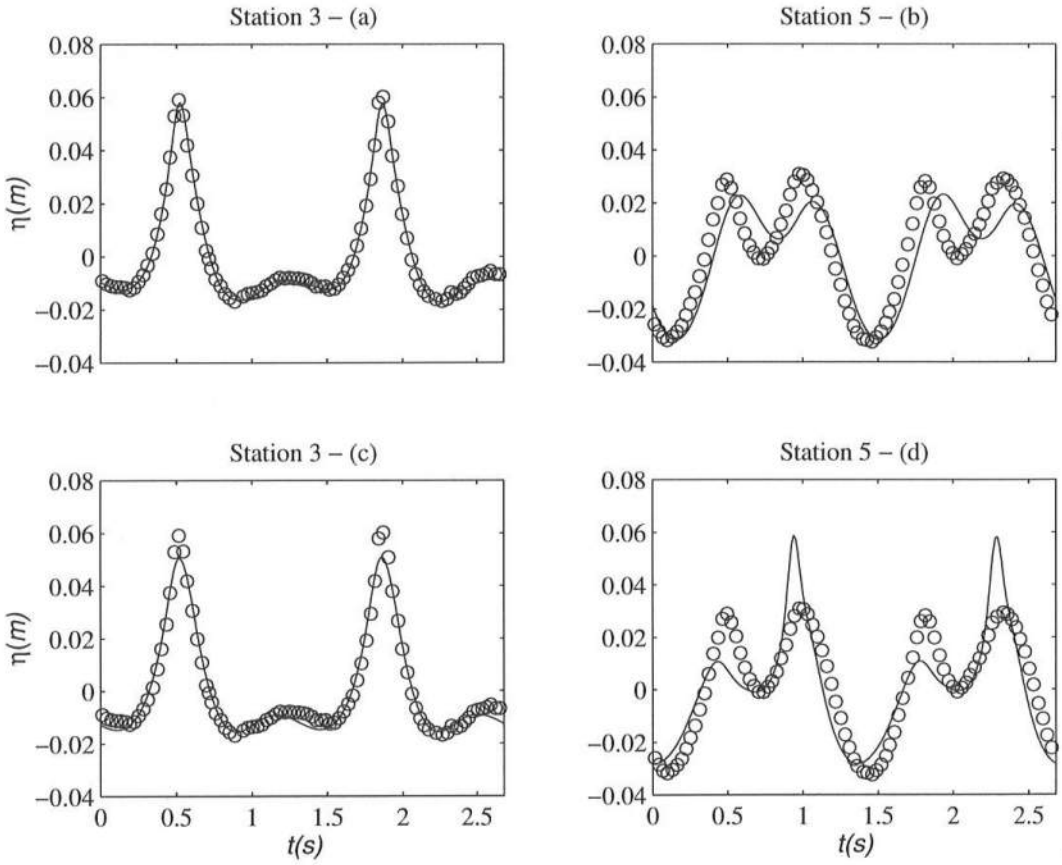

Figure 6.12: Comparisons of free surface displacement with case (2) of the Ohyama experimental data at stations 3 and 5. FN4 (upper panels - a,b), WKGS (lower panels c,d), data (circles).

Table 6.4: Index of agreement d_i.

Station	case (2)		case (4)		case (6)	
	WKGS	FN4	WKGS	FN4	WKGS	FN4
3	0.994	0.998	0.991	0.994	0.991	0.991
5	0.921	0.914	0.927	0.880	0.945	0.976

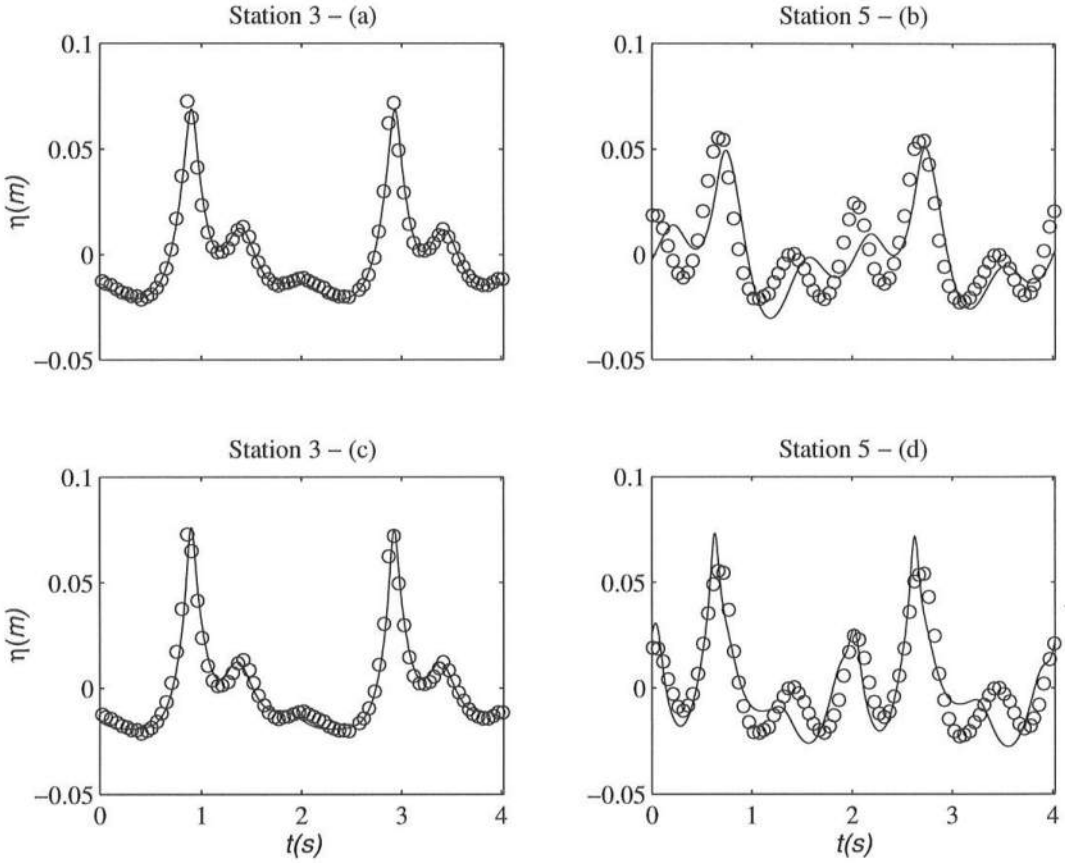

Figure 6.13: Comparisons of free surface displacement with case (4) of the Ohyama experimental data at stations 3 and 5. FN4 (upper panels - a,b), WKGS (lower panels c,d), data (circles).

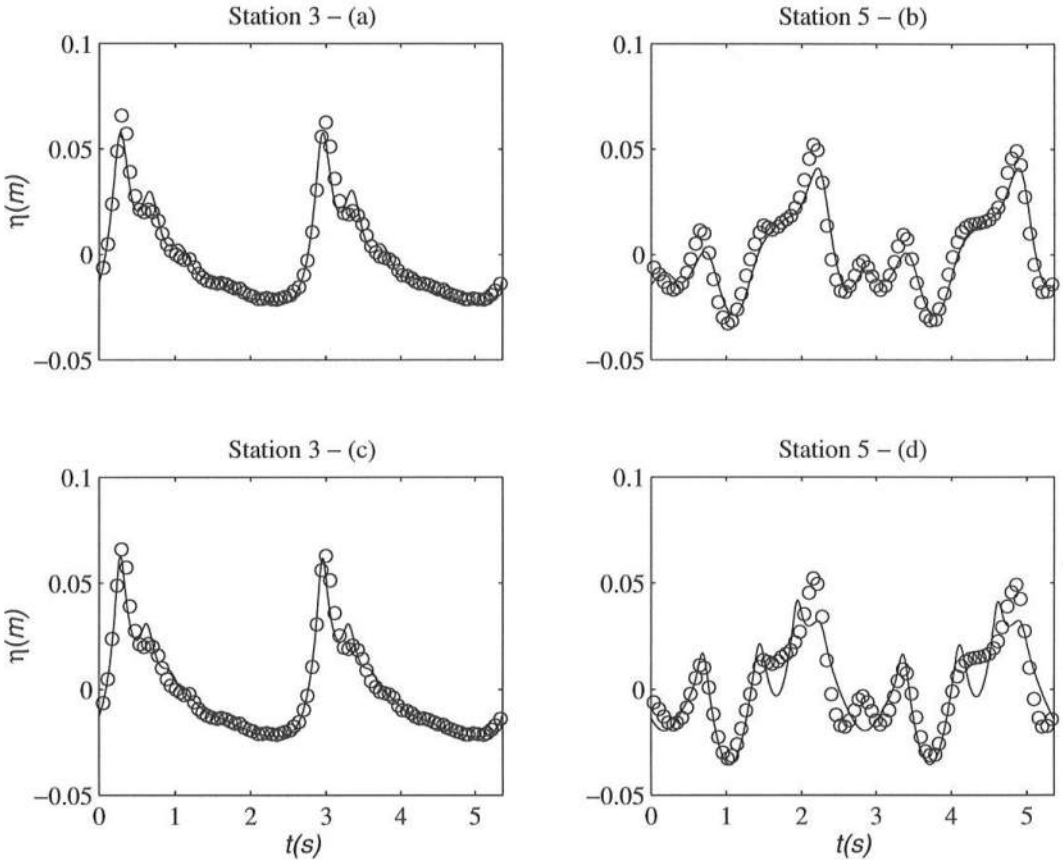

Figure 6.14: Comparisons of free surface displacement with case (6) of the Ohyama experimental data at stations 3 and 5. FN4 (upper panels - a,b), WKGS (lower panels c,d), data (circles).

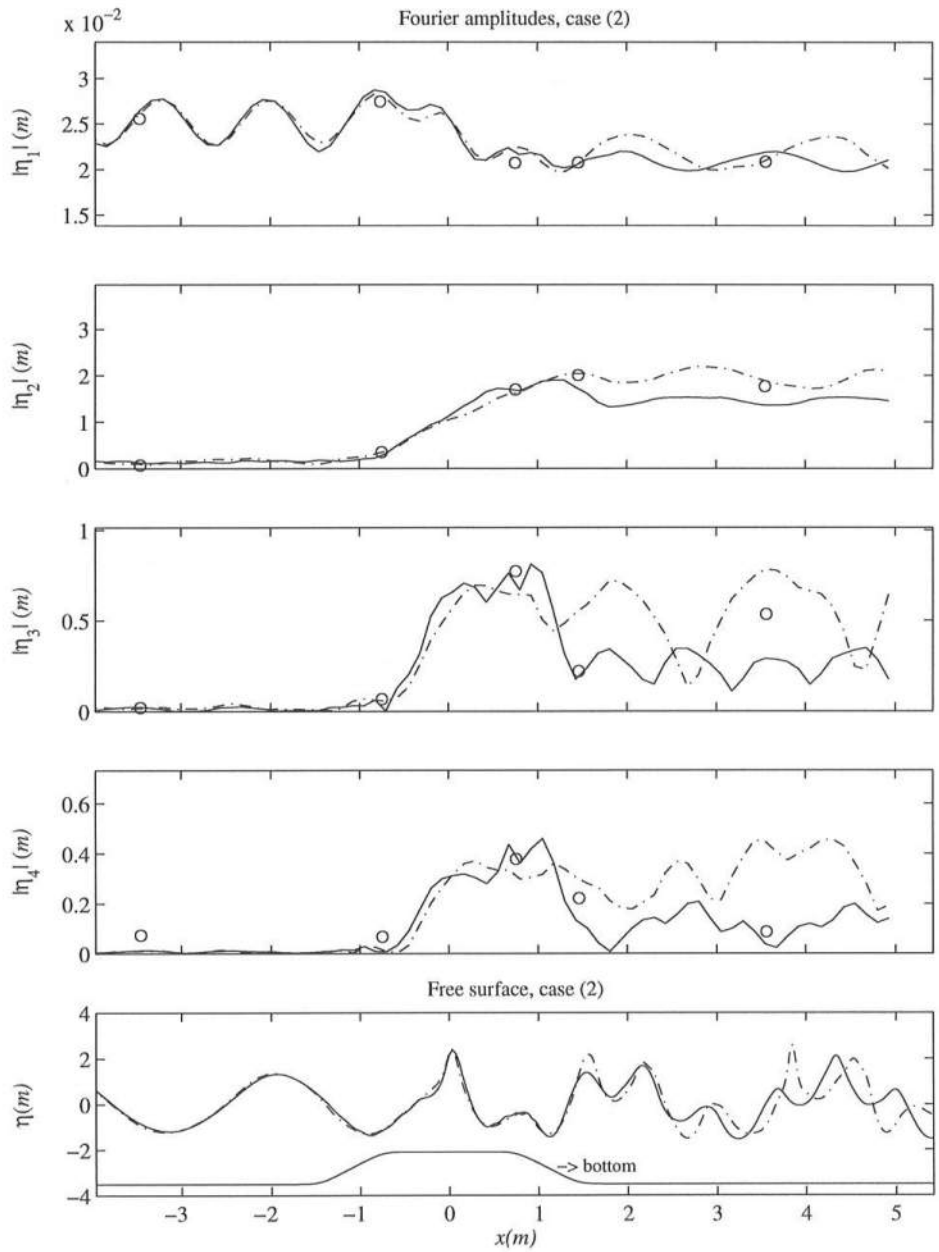

Figure 6.15: Comparisons of the spatial variation of the Fourier components of the free surface displacement with case (2) of the Ohyama experimental data. Bottom panel shows the free surface elevation. FN4 (solid), WKGS (dash-dot), data (circles).

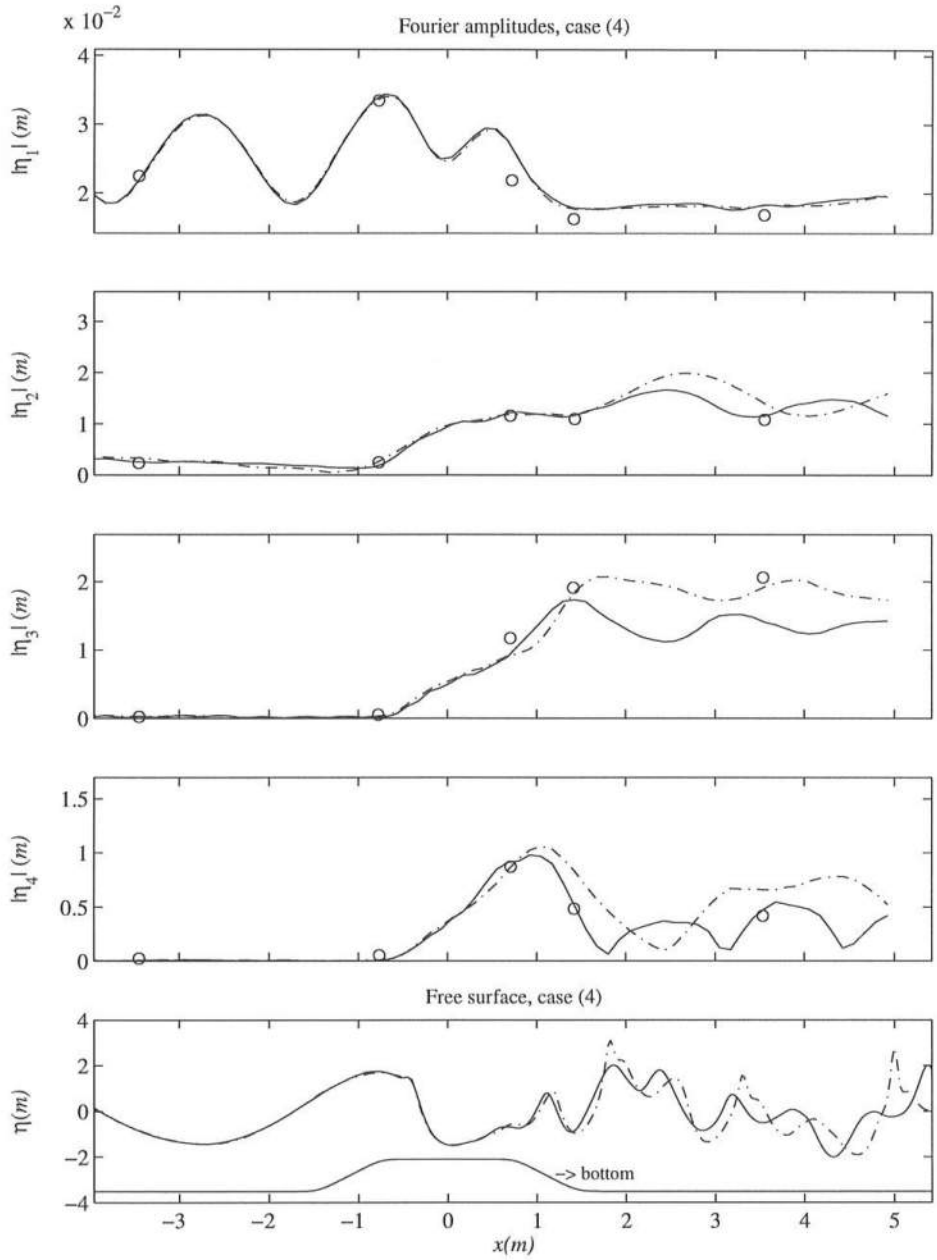

Figure 6.16: Comparisons of the spatial variation of the Fourier components of the free surface displacement with case (4) of the Ohyama experimental data. Bottom panel shows the free surface elevation. FN4 (solid), WKGS (dash-dot), data (circles).

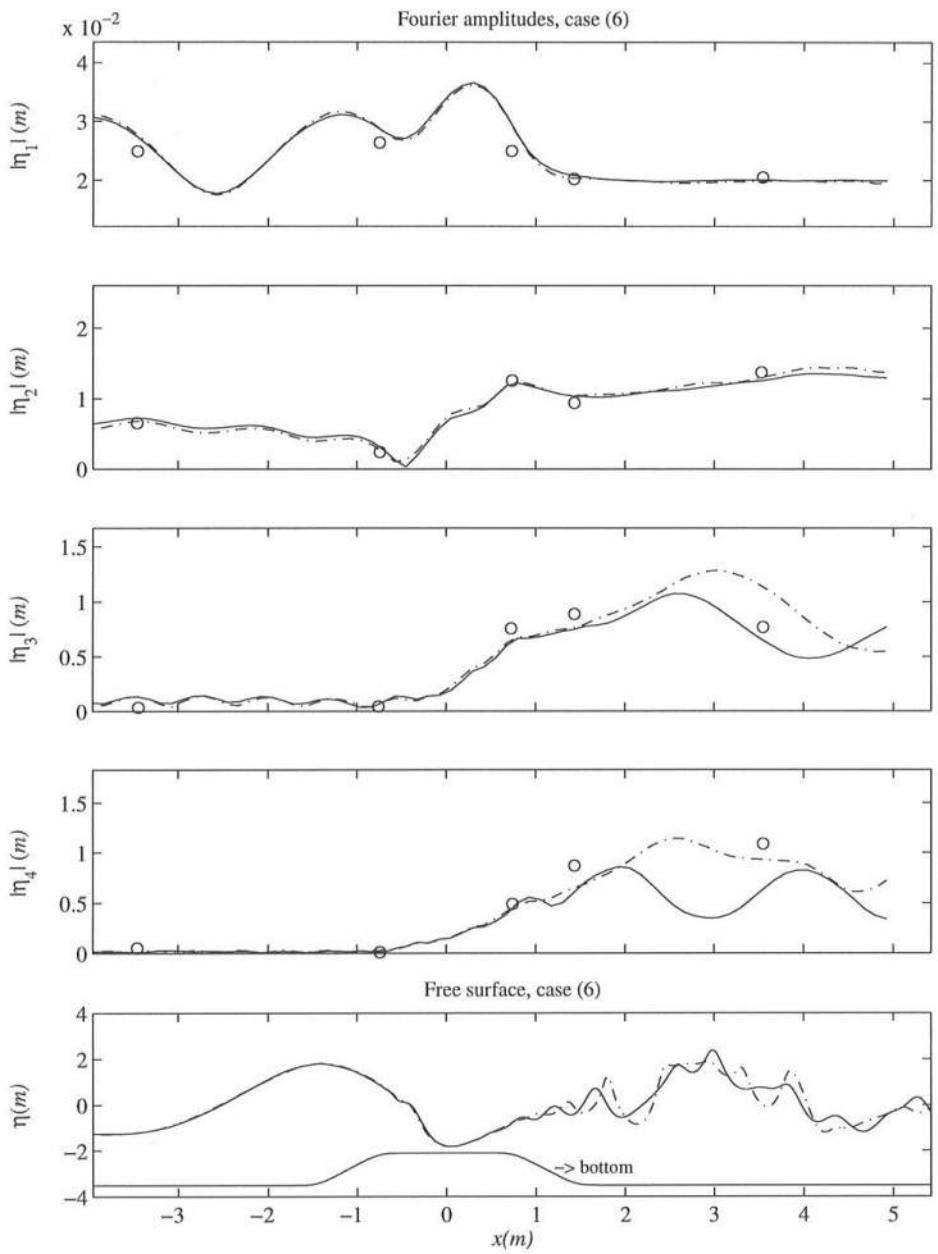

Figure 6.17: Comparisons of the spatial variation of the Fourier components of the free surface displacement with case (6) of the Ohyama experimental data. Bottom panel shows the free surface elevation. FN4 (solid), WKGS (dash-dot), data (circles).

and (4), the results indicate a better agreement with the data by WKGS than by FN4. By inspecting time series comparisons in Figures 6.12 and 6.13, it is clear that the better agreement index for the WKGS model is only due to a systematic phase error by the FN4 model, which, overall has a better qualitative agreement.

Chapter 7

CONCLUSIONS AND RECOMMENDATIONS

7.1 Conclusions

A Boussinesq-type model with $O(1)$ nonlinearity and $O(\mu^4)$ dispersion and vertical dependence was developed. By conveniently defining one of the dependent variables as the weighted average of the velocity potential at two distinct water depths, it is possible to achieve an accurate (4,4) Padé approximant form for the linear dispersion relationship. A major improvement over the existing second order models has been found in the prediction of the linear internal flow kinematics.

A perturbation approach was carried out to analyze random wave second order nonlinear interactions and it has been shown that the FN4 predicts very well the transfer coefficients of super and subharmonics generation over a wide range of water depths. The model's cubic nonlinear Schrödinger equation governing the propagation of wave group envelope was obtained by a standard WKB perturbation multiple scales approach and its coefficients were compared to those of the full model as well as of WKGS $O(\mu^2)$ model. The model's cubic term coefficient was shown to have good agreement with the full model.

A numerical implementation of the 1-dimensional version of the model was used to simulate wave evolution over arbitrary bottom topography. The numerical model included absorbing sponge layers to simulate radiation boundary conditions,

and generation of waves inside the domain by the inclusion of a source function in the system of equations. The source function was derived from Green's functions linear theory, but it was shown that it also works well for finite, relatively small amplitude waves.

Several numerical computations were carried out for solitary waves propagating over both horizontal and sloping bottoms, and many solitary wave properties were compared with both the exact solution and other models. It was shown that the FN4 model agrees better with the exact solution than does the WKGS model. Comparisons between FN4 and GN3 (third order Green-Naghdi model) with the exact solution showed that GN3 agrees better than FN4 for some properties. For sloping bottom, FN4 and WKGS models were compared with the very accurate BEM, and FN4 agreed with BEM better than WKGS. A set of GN3 evolution equations for variable depth is not available at this time, therefore no comparisons between FN4 and GN3 are available for this case.

Finally, numerical computations of FN4 and WKGS were compared to several laboratory measurements of waves propagating over submerged bars, and FN4 generally gave better agreement with the data. The weakly nonlinear version of the present model, WN4, was also compared to some of the experimental data. The results showed that the higher order nonlinear terms neglected in WN4 are essential for accurate prediction of higher amplitude waves, specially if these waves are in deeper water, since the higher harmonics are more susceptible to phase errors.

7.2 Recommendations for Future Work

The numerical implementation of the present model was found to have the following minor problems: (i) for very steep (nonlinear) waves, the convergence

of the iterative time integration can be fairly slow, besides that, in some cases, a very low under-relaxation parameter is needed to avoid divergence of the solution. Further investigation is required to improve the model in this aspect. (ii) A better treatment of the derivatives of the water depth at locations where they are singular could improve the performance of the model in that as it is now, filtering has to be applied to the solution every several time steps, and in cases of very abrupt transition, the sharp corners of the bottom needs to be smoothed.

In this work we used Green's function theory (linear) to derive the necessary source function for wave generation inside the domain. In cases of relatively high amplitude waves, the waves generated by the source function are not a solution to the equations, and therefore, undesirable frequencies may appear in the solution near the source region to "make up" for the differences. Further investigation is needed in this direction to: (i) quantify the validity of the use of a source function derived from linear theory with a nonlinear set of equations. (ii) derive a source function which generates solutions of the nonlinear problem for regular waves such as Stokes and cnoidal waves.

Lastly, the numerical implementation can be expanded to two spatial dimensions in a straightforward manner, although the computational cost involved in solving the system would be quite high for present standards. This step is also left for future work.

Appendix A

APPLICATION OF NWOGU'S METHOD AT $O(\mu^4)$

The procedure of Nwogu (1993) rests on choosing the potential or velocity at an elevation z_α in the water column such that the resulting linear dispersion relationship of the model is optimal in some sense. The dispersion relationship in a model retaining terms to $O(\mu^2)$ is given by

$$\omega^2 = \frac{1-(\alpha+1/3)\mu^2}{1-\alpha\mu^2} \tag{A.1}$$

where

$$\alpha = \frac{1}{2}z_\alpha^2 + z_\alpha \tag{A.2}$$

The choice $\alpha = -2/5$ reproduces the (2,2) Padé approximant, while the choice $\alpha = -0.39$ proposed by Nwogu minimizes the error (in a least-square sense) in the dispersion relation over the range $0 \leq \mu \leq \pi$.

Following this procedure, we extend the approximate expression for the velocity potential (in terms of ϕ_α) to $O(\mu^4)$ and obtain

$$\begin{aligned} \phi &= \phi_\alpha + \frac{\mu^2}{2}\left[(1+z_\alpha)^2 - (1+z)^2\right]\nabla^2\phi_\alpha \\ &+ \frac{\mu^4}{24}\left[5(1+z_\alpha)^4 - 6(1+z_\alpha)^2(1+z)^2 + (1+z)^4\right]\nabla^2\nabla^2\phi_\alpha \\ &+ O(\mu^6) \end{aligned} \tag{A.3}$$

This expression is used in linearized versions of (2.4) and (2.6) to obtain the linear model

$$\begin{aligned} \eta_t &+ \nabla^2\phi_\alpha + \mu^2(\alpha+1/3)\nabla^2\nabla^2\phi_\alpha + \mu^4(5\alpha^2+4\alpha+4/5)\nabla^2\nabla^2\nabla^2\phi_\alpha = 0 \\ \eta &+ \phi_{\alpha t} + \mu^2\alpha\nabla^2\phi_{\alpha t} + \mu\frac{\alpha}{6}(2+5\alpha)\nabla^2\nabla^2\phi_{\alpha t} = 0 \end{aligned} \tag{A.4}$$

The corresponding linearized dispersion relation is given by

$$\omega^2 = \frac{1-(\alpha+1/3)\mu^2+(5\alpha^2+4\alpha+4/5)\mu^4}{1-\alpha\mu^2+(5\alpha^2/6+\alpha/3)\mu^4} \tag{A.5}$$

This is equivalent to Nwogu's result if terms of $O(\mu^4)$ are dropped. The resulting dispersion relation contains only a single parameter, and there is no choice of α which reproduces the desired (4,4) Padé approximant:

$$\omega^2 = \frac{1+(1/9)\mu^2+(1/945)\mu^4}{1+(4/9)\mu^2+(1/63)\mu^4} + O(\mu^6). \tag{A.6}$$

It has been shown, therefore, that by using Nwogu's method of choosing the potential at a depth z_α as the dependent variable in a 4^{th} degree polynomial in z, it is not possible to obtain the desired (4,4) Padé approximant.

Appendix B

DERIVATION OF THE SCHRÖDINGER EQUATION ASSOCIATED WITH THE PRESENT MODEL

Here we present the derivation of the Schrödinger equation for the present model in dimensional form. The nondimensional final results are presented in Chapter 3.

The constant depth versions of the evolution equations for $\tilde{\phi}$ and η in dimensional form are:

$$\begin{aligned}
\eta_t &+ \nabla\cdot\left\{H\left[\nabla\tilde{\phi}+\frac{1}{2}\left(B-\frac{1}{3}H^2\right)\nabla\nabla^2\tilde{\phi}\right.\right. \\
&+ \left.\left.\frac{1}{4}\left(B^2-\frac{1}{6}D-\frac{1}{3}BH^2+\frac{1}{30}H^4\right)\nabla\nabla^2\nabla^2\tilde{\phi}\right]\right\}=0 \qquad \text{(B.1)} \\
g\eta &+ \tilde{\phi}_t+\frac{1}{2}\left|\nabla\tilde{\phi}\right|^2+\frac{1}{2}\left(B-H^2\right)\nabla^2\tilde{\phi}_t \\
&+ \frac{1}{4}\left(B^2-\frac{1}{6}D-BH^2+\frac{1}{6}H^4\right)\nabla^2\nabla^2\tilde{\phi}_t \\
&+ \nabla\tilde{\phi}\cdot\nabla\left[\frac{1}{2}\left(B-H^2\right)\nabla^2\tilde{\phi}\right. \\
&+ \left.\frac{1}{4}\left(B^2-\frac{1}{6}D-BH^2+\frac{1}{6}H^4\right)\nabla^2\nabla^2\tilde{\phi}\right] \\
&+ \frac{1}{8}\nabla\left|\left(B-H^2\right)^2\left(\nabla^2\tilde{\phi}\right)\right|^2+\frac{1}{2}H^2\left(\nabla^2\tilde{\phi}\right)^2 \\
&+ \frac{1}{4}\left(BH^2-\frac{1}{3}H^4\right)\nabla^2\tilde{\phi}\nabla^2\nabla^2\tilde{\phi}=0 \qquad \text{(B.2)}
\end{aligned}$$

Assuming δ as our small parameter, we expand for our dependent variables as:

$$\begin{aligned}\eta &= \delta\eta_1 + \delta^2\eta_2 + \delta^3\eta_3 \\ \tilde{\phi} &= \delta\phi_1 + \delta^2\phi_2 + \delta^3\phi_3\end{aligned} \tag{B.3}$$

and introduce multiple scales for the independent variables as:

$$\begin{aligned}t &= t' + \delta t' + \delta^2 t' = t' + T_1 + T_2 \\ x &= x' + \delta x' + \delta^2 x' = x' + X_1 + X_2 \\ y &= \delta y' + \delta^2 y' = Y_1 + Y_2\end{aligned} \tag{B.4}$$

Before we proceed, we define the following operators:

$$\begin{aligned}L_1(\cdot) &\equiv -(\cdot)_{tt} + gh(\cdot)_{xx} - gC_1h^3(\cdot)_{xxxx} + gC_2h^5(\cdot)_{xxxxxx} \\ &+ C_3h^2(\cdot)_{xxtt} - C_4h^4(\cdot)_{xxxxxx} \qquad \text{(B.5)} \\ L_2(\cdot) &\equiv -2(\cdot)_{tT_1} + 2gh(\cdot)_{xX_1} + 2gh(\cdot)_{xX_1} + 4C_1h^3(\cdot)_{xxxX_1} \\ &+ 6gC_2h^5(\cdot)_{xxxxxX_1} + 2C_3h^2(\cdot)_{xxtT_1} \\ &+ 2C_3h^2(\cdot)_{xX_1tt} - 2C_4h^4(\cdot)_{xxxxtT_1} - 4C_4h^4(\cdot)_{xxxX_1tt} \qquad \text{(B.6)} \\ L_3(\cdot) &\equiv -(\cdot)_{T_1T_1} - 2(\cdot)_{tT_2} + gh(\cdot)_{X_1X_1} + 2gh(\cdot)_{xX_2} + gh(\cdot)_{Y_1Y_1} \\ &- C_1h^3\left[6(\cdot)_{xxX_1X_1} + 4(\cdot)_{xxxX_2} + 2(\cdot)_{xxY_1Y_1}\right] \\ &+ C_2h^5\left[15(\cdot)_{xxxxX_1X_1} + 6(\cdot)_{xxxxxX_2} + 3(\cdot)_{xxxxY_1Y_1}\right] \\ &+ C_3h^5\left[(\cdot)_{xxT_1T_1} + 2(\cdot)_{xxtT_2} + 4(\cdot)_{xX_1tT_1}\right. \\ &+ \left.(\cdot)_{X_1X_1tt} + 2(\cdot)_{xX_2tt} + (\cdot)_{Y_1Y_1tt}\right] \\ &- C_4h^4\left[(\cdot)_{xxxT_1T_1} + (\cdot)_{xxxxtT_2} + 2(\cdot)_{xxxxtT_2} + 8(\cdot)_{xxxX_1tT_1}\right. \\ &+ \left.6(\cdot)_{xxX_1X_1tt} + 4(\cdot)_{xxxX_2tt} + 2(\cdot)_{xxY_1Y_1tt}\right] \qquad \text{(B.7)} \\ L_1'(\cdot) &\equiv (\cdot)_t - C_3h^2(\cdot)_{xxt} + C_4h^4(\cdot)_{xxxxt} \qquad \text{(B.8)} \\ L_2'(\cdot) &\equiv (\cdot)_{T_1} - C_3h^2\left[(\cdot)_{xxT_1} + 2(\cdot)_{xX_1t}\right]\end{aligned}$$

$$+ \quad C_4 h^4 \left[(\cdot)_{xxxxT_1} + (\cdot)_{xxxX_1 t} \right] \tag{B.9}$$

$$\begin{aligned} L_3'(\cdot) \equiv\ & (\cdot)_{T_2} - C_3 h^2 \left[2(\cdot)_{xX_1T_1} + (\cdot)_{xxT_2} + 2(\cdot)_{xX_2t} + (\cdot)_{X_1X_1t} + (\cdot)_{Y_1Y_1t} \right] \\ & + C_4 h^4 \left[(\cdot)_{xxxxT_2} + 4(\cdot)_{xxxX_1T_1} + 4(\cdot)_{xxxX_2t} \right. \\ & \left. + 6(\cdot)_{xxX_1X_1t} + 2(\cdot)_{xxY_1Y_1t} \right] \end{aligned} \tag{B.10}$$

where C_1, C_2, C_3, C_4 are given in the section below. For each order $n = 0, 1, \ldots$ we assume the following solution corresponding to a nonlinear wave train propagating mainly in the x direction, but allowing the amplitudes ϕ_{nm} and η_{nm} to have slow variations in space and time:

$$\eta_n = \sum_{m=-n}^{n} \eta_{nm}(X_1, X_2, Y_1, Y_2, T_1, T_2) E^m \tag{B.11}$$

$$\phi_n = \sum_{m=-n}^{n} \phi_{nm}(X_1, X_2, Y_1, Y_2, T_1, T_2) E^m \tag{B.12}$$

where $E \equiv e^{i(kx-\omega t)}$, n indicates the order of the solution, and negative m indices indicate the complex conjugate of $-m$ for both η_{nm} and ϕ_{nm}. Substituting (B.3) and (B.4) into the t derivative of (B.2) minus g times (B.1), and into (B.2), and ordering the problem in powers of δ, we obtain for $n = 1$:

$$L_1 \phi_1 = 0 \tag{B.13}$$

$$g\eta_1 + L_1' \phi_1 = 0 \tag{B.14}$$

Substituting (B.11) and (B.12) with $n = 0$ into (B.13) and (B.14), we obtain:

$$D_1 \phi_{11} = 0 \tag{B.15}$$

and

$$\phi_{11} = \frac{-igA}{2\omega \left[1 + C_3 (kh)^2 + C_4 (kh)^4 \right]}, \qquad A \equiv 2\eta_{11} \tag{B.16}$$

where

$$D_1 \equiv -gk(kh)\left[1 + C_1(kh)^2 + C_2(kh)^4\right] + \omega^2\left[1 + C_3(kh)^2 + C_4(kh)^4\right] \quad \text{(B.17)}$$

and (B.15) is the linear dispersion relationship. We arbitrarily assumed that $\eta_{10} = 0$. We now proceed to seek a "slowly varying equation" for A.

For $n = 2$, we obtain the equations:

$$\begin{aligned} L_1\phi_2 \;+\; & L_2\phi_1 + g(\eta_1\phi_{1x})_x - gC_3h^2(\eta_1\phi_{1xxx})_x \\ + \; & gC_4h^4(\eta_1\phi_{1xxxxx})_x + h(\eta_1\phi_{1xxt})_t - \frac{1}{2}(\phi_{1x}\phi_{1x})_t \\ - \; & C_1h^3(\eta_1\phi_{1xxxt})_t + C_3h^3(\phi_{1x}\phi_{1xxx})_t \\ - \; & C_4h^4(\phi_{1x}\phi_{1xxxxx})_t - \frac{1}{2}C_3^2h^4(\phi_{1xxx}\phi_{1xxx})_t \\ - \; & \frac{1}{2}h^2(\phi_{1xx}\phi_{1xx})_t + C_1h^4(\phi_{1xx}\phi_{1xxxx})_t = 0 \end{aligned} \quad \text{(B.18)}$$

and

$$\begin{aligned} g\eta_2 \;+\; & L_1'\phi_2 + L_2'\phi_1 - h\eta_1\phi_{1xxt} + \frac{1}{2}\phi_{1x}\phi_{1x} + C_1h^3\eta_1\phi_{1xxxxt} \\ + \; & C_3h^2\phi_{1x}\phi_{1xxx} + C_4h^4\phi_{1x}\phi_{1xxxxx} \\ + \; & \frac{1}{2}h^2\phi_{1xx}\phi_{1xx} - C_1h^2\phi_{1xx}\phi_{1xxxx} = 0 \end{aligned} \quad \text{(B.19)}$$

Substituting (B.11) and (B.12) with $n = 1$ into (B.18), and matching the coefficients of each power of E, we obtain (all terms $\sim E^0$ are zero for this equation at this order):

(i) terms $\sim E^1$:

$$2i\omega\left[1 + C_3(kh)^2 + C_4(kh)^4\right]\left[\phi_{11T_1} + C_g\phi_{11X_1}\right] = 0 \quad \text{(B.20)}$$

which implies that

$$\phi_{11T_1} + C_g\phi_{11X_1} = 0 \quad \text{(B.21)}$$

where $C_g \equiv \partial\omega/\partial k$ from the dispersion relationship (B.15).

(ii) terms $\sim E^2$:

$$\begin{aligned} D_2\phi_{22} &- 2gk^2\left\{1 + C_3(kh)^2 + C_4(kh)^4\right. \\ &- \left.\frac{\omega h}{g}\left[1 + C_1(kh)^2\right]\right\}\eta_{11}\phi_{11} \\ &- i\omega k^2\left[1 + 2C_3(kh)^2 + 4C_4(kh)^4\right. \\ &+ \left. C_3^2(kh)^4 - (kh)^2 - 2C_1(kh)^4\right]\phi_{11}^2 \end{aligned} \tag{B.22}$$

where

$$\begin{aligned} D_2 &\equiv -4gk(kh)\left[1 + 4C_1(kh)^2 + 8C_2(kh)^4\right] \\ &+ 4\omega^2\left[1 + 4C_3(kh)^2 + 8C_4(kh)^4\right] \end{aligned} \tag{B.23}$$

Substituting (B.16) into (B.22), we obtain after some algebra:

$$\begin{aligned} \phi_{22} &= \frac{-igA^2}{16\omega h}\left\{2\left[1 + C_3(kh)^2 + C_4(kh)^4\right]^2\right. \\ &- 2(kh)^2\left[1 + C_1(kh)^2 + C_2(kh)^4\right]\left[1 + C1(kh)^2\right] \\ &+ \left. 1 + (2C_3 - 1)(kh)^2 - 2C_4(kh)^4 + C_3^2(kh)^4 - C_1(kh)^4\right\}\left\{(kh)^2\right. \\ &+ \left. 15(C_4 - C_2)(kh)^4 + 12(C_1C_4 - C_2C_3)(kh)^6\right\}^{-1} \end{aligned} \tag{B.24}$$

Substituting (B.11) and (B.12) with $n = 1$ into (B.19), and matching the coefficients of each power of E, we obtain:

(i) terms $\sim E^0$:

$$\begin{aligned} g\eta_{20} &= -\phi_{10T_1} - \left[(2C_3 + 1)(kh)^2 + 1\right]k^2\phi_{11}\phi_{1-1} \\ &+ i\omega k^2 h(\eta_{1-1}\phi_{11} - \eta_{11}\phi_{1-1}) - (2C_1 + C_3^2 + 2C_4)(kh)^4k^2\phi_{11}\phi_{1-1} \\ &+ i\omega C_1K^4h^3(\eta_{1-1}\phi_{11} - \eta_{11}\phi_{1-1}) \end{aligned} \tag{B.25}$$

Using (B.16) into (B.25), we obtain after some algebra:

$$\begin{aligned}\eta_{20} &= -\frac{1}{g}\phi_{10T_1} \\ &+ \left\{\frac{-\left[(2C_3+1)(kh)^2+1\right]+\left[-2C_3-C_1^2-2C_4\right](kh)^4}{1+C_1(kh)^2+C2(kh)^4}\right. \\ &+ \left. 2(kh)^2+2C_1(kh)^4\right\}\frac{|A|^2}{4h\left[1+C_3(kh)^2+C5(kh)^4\right]} \qquad \text{(B.26)}\end{aligned}$$

(ii) terms $\sim E^1$:

$$\begin{aligned}g\eta_{21} &= i\omega\left[1+C_3(kh)^2+C_4(kh)^4\right]\phi_{21}-\left[1+C_3(kh)^2+C_4(kh)^4\right]\phi_{11T_1} \\ &+ 2\omega kh^2\left[C_3+2C_4(kh)^2\right]\phi_{11X_1} \qquad \text{(B.27)}\end{aligned}$$

Since ϕ_{21} can be absorbed into ϕ_{11}, we set $\phi_{21}=0$ without loss of generality. Substituting (B.16) into (B.27), we obtain after some algebra:

$$\eta_{21}=\frac{i}{2\omega}A_{T_1}-i\frac{C_3(kh)^2+2C_4(kh)^4}{k\left[1+C_3(kh)^2+C_4(kh)^4\right]}A_{X_1} \qquad \text{(B.28)}$$

(ii) terms $\sim E^2$:

$$\begin{aligned}g\eta_{22} &= 2i\omega\left[1+4C_3(kh)^2+16C_4(kh)^4\right]\phi_{22} \\ &+ i\omega k^2h\eta_{11}\phi_{11}+\frac{1}{2}k^2\phi_{11}^2+i\omega C_1k^4h^3\eta_{11}\phi_{11}+C_3k^4h^2\phi_{11}^2 \\ &+ C_4k^6h^4\phi_{11}^2+\frac{1}{2}C_3^2k^6h^4\phi_{11}^2-\frac{1}{2}k^4h^2\phi_{11}^2-C_1k^6h^4\phi_{11}^2 \qquad \text{(B.29)}\end{aligned}$$

Substituting (B.16) and (B.24) into (B.29), we rewrite (B.29) is the schematic form:

$$\eta_{22}=S_{22}\frac{A^2}{8h} \qquad \text{(B.30)}$$

where S_{22} is a complicated function of kh.

We are now ready to move on to the next order, $n = 3$. At this order, a great amount of algebra is necessary in the evaluation of all the nonlinear terms, and since we already have evaluated all the dependent variables appearing in these terms from the previous orders, from this point, we only outline the steps before we give the final result. For $n = 3$, the combined equation

$\partial/\partial t$ (B.2) - $g\times$ (B.1) becomes:

$$L_1\phi_3 + L_2\phi_2 + L_3\phi_1 + Z_1 + Z_2 + Z_3 = 0 \tag{B.31}$$

where Z_3 are the nonlinear cubic terms involving products of η_1 and ϕ_1, and their fast time (t) and spatial (x) derivatives. Z_2 are the nonlinear terms involving products between either η_1 and ϕ_2 or η_2 and ϕ_1, and Z_1 are nonlinear terms involving products between η_1 and ϕ_1 and containing either a T_1 or an X_1 derivative. We now substitute (B.11) and (B.12) with $n = 2$ into (B.31). To obtain the Schrödinger equation for A, only information $\sim E^0$ and $\sim E^1$ is needed. The only linear term in (B.31) that contributes to $\sim E^0$ and $\sim E^1$ is $L_3\phi_1$. Using the relations

$$\phi_{11T_1} = -C_g\phi_{11X_1} \tag{B.32}$$

$$\phi_{11T_1T_1} = C_g^2\phi_{11X_1X_1} \tag{B.33}$$

$$\phi_{11X_1T_1} = -C_g\phi_{11X_1X_1} \tag{B.34}$$

after some algebra, the linear term $L_3\phi_1$ becomes:

$$\begin{aligned} L_3\phi_1 &= 2i\omega\left[1 + C_3(kh)^2 + C_4(kh)^4\right]\times \\ &\quad \left(\phi_{11T_2} + C_g\phi_{11X_2} - \frac{i}{2}\omega''\phi_{11X_1X_1} - i\frac{C_g}{2k}\phi_{11Y_1Y_1}\right)E^1 \\ &+ \left[-\phi_{10T_1T_1} + gh\left(\phi_{10X_1X_1} + \phi_{10Y_1Y_1}\right)\right] \end{aligned} \tag{B.35}$$

Where ω'' is obtained by twice differentiating ω with respect to k in the dispersion relationship.

Substituting the relations between η_{11}, η_{20}, η_{22}, ϕ_{11}, ϕ_{22}, and A in all $\sim E^1$ nonlinear terms in (B.31), and combining them with the $\sim E^1$ terms in (B.35), we find the following equation:

$$\begin{aligned} & A_{T_2} + C_g A_{X_2} - \frac{i}{2}\omega'' A_{X_1 X_1} - \frac{iC_g}{2k} A_{Y_1 Y_1} + i\sigma_1 |A|^2 A \\ + \quad & i\delta\mu \left\{ \phi_{10_{X_1}} + \frac{1 + C_3\mu^2 + C_4\mu^4 - \mu^2\omega^2 (1 + C_1\mu^2)}{2\omega (1 + C_3\mu^2 + C_4\mu^4)} \phi_{10_{X_1}} \right\} = 0 \end{aligned} \quad \text{(B.36)}$$

where σ_1 is given in nondimensional form in the next section.

Similarly, we combine the linear and nonlinear $\sim E^0$ terms, and after some algebra, we obtain

$$-\phi_{10_{T_1 T_1}} + gh \left(\phi_{10_{X_1 X_1}} + \phi_{10_{Y_1 Y_1}} \right) = \frac{g^2 k}{2\omega} |A|^2_{X_1} + S_0 |A|^2_{T_1} \quad \text{(B.37)}$$

where

$$S_0 = \frac{-\omega^2 \left[1 - C1(kh)^2\right] \left[1 + (1 + 2C_3)(kh)^2 + (2C_4 + C_3^2 + 2C_1)(kh)^4\right]}{4(kh)^2 \left[1 + C_1(kh)^2 + C_2(kh)^4\right]} \quad \text{(B.38)}$$

Now we introduce the changes of variables

$$\xi = X_1 - C_g T_1, \quad \tau = \delta T_1 \quad \text{(B.39)}$$

Substituting (B.39) into (B.37) and integrating once with respect to ξ we get:

$$\phi_{10_\xi} = \frac{g^2 k/(2\omega) - C_g S_0}{C_g^2 - gh} |A|^2 + \gamma_0(\tau) \quad \text{(B.40)}$$

where $\gamma_0(\tau)$ is an integration constant which vanishes for a wave train beginning from rest where A and $\phi_{10\xi}$ tend to zero as $\xi \to \infty$ (see Mei, 1989). Substituting (B.40) with (B.39) into (B.36) with T_2/δ replacing T_1, we have:

$$A_\tau - \frac{i}{2}\omega'' A_{\xi\xi} - \frac{i}{2}\frac{C_g}{k} A_{Y_1 Y_1} + i\sigma |A|^2 A + \gamma_1(\tau) A = 0 \qquad \text{(B.41)}$$

where $\gamma_1(\tau)$ absorbs $\gamma_0(\tau)$. Without Y_1 derivatives and without the last term containing $\gamma_1(\tau)$, equation above is the cubic Schrödinger equation. The last term can be absorbed into a new dependent variable by the transformation $A' = Ae^{i\int \gamma_1 d\tau}$. The nondimensional version of equation above is given in Chapter 3. The coefficient $\sigma = \sigma_1 + \sigma_2$ is given in nondimensional form in the next section.

B.1 Expressions for Cubic Term Coefficient

$$\begin{aligned}
\sigma_1 &= \frac{-P_{22}}{\omega Q_1 Q_2}\left[4 + 16C_1\mu^2 - \omega^{-2}\left(1 + 4C_3\mu^2 + 16C_4\mu^4\right)\right] \\
&- \frac{\omega}{2Q_1}\left(E_{20} + E_{22}\right)\left(\mu + C_1\mu^3 - \omega^{-2}\mu^{-1}Q_1\right) \\
&+ \frac{P_{22}}{4\mu^2\omega^3 Q_1^2 Q_2}\left[1 + (2 + 5C_3)\mu^2 + \left(10C_1 + 17C_4 + 4C_3^2\right)\mu^4\right] \\
&- \frac{3}{16Q_1}\left[1 + C_3\mu^2 - \omega^{-2}\left(1 + C_1\mu^2\right)\right] \\
&+ \frac{1}{\omega Q_1^2}\left[4 + (8C_3 + 1/6)\mu^2\right] \\
\sigma_2 &= \frac{\left(\frac{1}{2\omega\mu^2} - C_g Q_3\right)}{2\left(C_g^2 - 1\right)}\left[\frac{C_g}{\omega Q_1}\left\{Q_1 - \mu^2\left(1 + C_1\mu^2\right)\right\} + \left(1 + \frac{1}{Q_1}\right)\right]
\end{aligned}$$

Where

$$\begin{aligned}
Q_1 &= 1 + C_3\mu^2 + C_4\mu^4 \\
Q_2 &= 4\left(1 + \omega^{-2}\right)\left(1 + 4C_1\mu^2 + 4C_4\mu^4\right)
\end{aligned}$$

$$
\begin{aligned}
Q_3 &= \frac{1}{2Q_1}\left\{1-C_1\mu^2\right\}+\frac{1}{4\omega^2Q_1^2\mu^2}\left\{1+\left(2C_3+1\right)\mu^2+\left(2C_4+C_3^2+2C_1\right)\mu^4\right\}\\
P_{22} &= -2\left[Q_1-\mu^2\left(1+C_1\mu^2\right)\right]-Q_1^{-1}\left[2Q_1-1-\mu^2-\left(2C_1-C_3^2\right)\mu^4\right]\\
E_{20} &= \frac{\mu}{2Q_1}\left(1+C_1\mu^2\right)-\frac{1}{\mu\omega^2Q_1^2}\left[2Q_1-1+\mu^2+\left(2C_1+C_3^2\right)\mu^4\right]\\
E_{22} &= \frac{1}{2\omega^2Q_2Q_1}P_{22}\left(1+4C_3\mu^2+16C_4\mu^4\right)\\
&+ \frac{\mu}{4Q_1}\left(1+C_1\mu^2\right)-\frac{1}{\mu\omega^2Q_1^2}\left[2Q_1-1-\mu^2+\left(2C_1-C_3^2\right)\mu^4\right]
\end{aligned}
$$

and

$$
\begin{aligned}
C_1 &= -\frac{1}{2}\left(B-1/3\right); \quad C_2=\frac{1}{4}\left(B^2-B/3-D/6+1/30\right)\\
C_3 &= -\frac{1}{2}\left(B-1\right); \quad C_4=\frac{1}{4}\left(B^2-B-D/6+1/6\right)
\end{aligned}
$$

The corresponding σ_1 and σ_2 for the full boundary value problem are given by:

$$
\begin{aligned}
\sigma_1 &= \frac{\cosh 4\mu+8-2\tanh^2\mu}{16\sinh^4\mu}\\
\sigma_2 &= \frac{1}{2\omega\left(C_g^2-1\right)}\left(1+\frac{C_g}{2\omega\cosh^2\mu}\right)^2
\end{aligned}
$$

Appendix C

DERIVATION OF SOURCE FUNCTION

Here we derive the x-direction source function for regular waves. The linearized versions of the mass and momentum equations for $\tilde{\phi}$ over a flat bottom, including the source function is given, in dimensional form, as:

$$\eta_t - h\nabla^2\tilde{\phi} + C_1h^3\nabla^2\nabla^2\tilde{\phi} + C_2h^5\nabla^2\nabla^2\nabla^2\tilde{\phi} = f_s(x,y,t), \tag{C.1}$$

$$\tilde{\phi}_t + g\eta + h\nabla^2\tilde{\phi} - C_3h^3\nabla^2\nabla^2\tilde{\phi}_t + C_4h^5\nabla^2\nabla^2\nabla^2\tilde{\phi}_t = 0, \tag{C.2}$$

where coefficients C_1, C_2, C_3, C_4 are as defined in Appendix B. Taking the t derivative of the momentum equation and eliminating η from (C.1) and (C.2), gives:

$$\begin{aligned}\tilde{\phi}_{tt} &- gh\nabla^2\tilde{\phi} + C_1gh^3\nabla^2\nabla^2\tilde{\phi} - C_2gh^5\nabla^2\nabla^2\nabla^2\phi \\ &- C_3h^3\nabla^2\nabla^2\tilde{\phi}_{tt} + C_4h^5\nabla^2\nabla^2\nabla^2\tilde{\phi}_{tt} = -gf_s(x,y,t).\end{aligned} \tag{C.3}$$

We introduce the following transformations:

$$\tilde{\phi}(x,y,t) = \left(\frac{1}{2\pi}\right)^2 \int_{-\infty}^{+\infty}\int_{-\infty}^{+\infty} \hat{\phi}(x)e^{i\lambda y}e^{-i\omega t}d\lambda d\omega \tag{C.4}$$

$$f(x,y,t) = \left(\frac{1}{2\pi}\right)^2 \int_{-\infty}^{+\infty}\int_{-\infty}^{+\infty} \hat{f}(x)e^{i\lambda y}e^{-i\omega t}d\lambda d\omega. \tag{C.5}$$

Substituting (C.4) and (C.5) into (C.3) we have:

$$a\hat{\phi}^{[6]} + b\hat{\phi}^{[4]} + c\hat{\phi}^{[2]} + d\hat{\phi} = g\hat{f}, \tag{C.6}$$

where the numbers in brackets denote order of x derivatives, and

$$\begin{aligned} a &\equiv C_2 g h^5, \\ b &\equiv -C_1 g h^3 + C_4 h^4 \omega^2 - 3C_2 g h^5 \lambda^2, \\ c &\equiv gh - C_3 h^2 \omega^2 + 2C_1 g h^3 \lambda^2 - 2C_4 h^4 \lambda^2 \omega^2 + 3C_2 g h^5 \lambda^4, \\ d &\equiv \omega^2 - gh\lambda^2 + C_3 h^2 \lambda^2 \omega^2 - C_1 g h^3 \lambda^4 + C_4 h^4 \lambda^4 \omega^2 - C_2 g h^5 \lambda^6. \end{aligned} \quad \text{(C.7)}$$

Now we multiply (C.6) by a Green's function $G(\xi, x)$, and integrate the product with respect to ξ, from $-\infty$ to $+\infty$, which gives:

$$\begin{aligned} & \int_{-\infty}^{+\infty} \left(aG^{[6]} + bG^{[4]} + cG^{[2]} + dG \right) \hat{\phi} d\xi \\ + \; & a \left[G\hat{\phi}^{[5]} - G^{[1]}\hat{\phi}^{[4]} + G^{[2]}\hat{\phi}^{[3]} - G^{[3]}\hat{\phi}^{[2]} + G^{[4]}\hat{\phi}^{[1]} + G^{[5]}\hat{\phi} \right]_{-\infty}^{+\infty} \\ + \; & b \left[G\hat{\phi}^{[3]} - G^{[1]}\hat{\phi}^{[2]} + G^{[2]}\hat{\phi}^{[1]} - G^{[3]}\hat{\phi} \right]_{-\infty}^{+\infty} \\ + \; & c \left[G\hat{\phi}^{[1]} - G^{[1]}\hat{\phi} \right]_{-\infty}^{+\infty} = g \int_{-\infty}^{+\infty} G\hat{f} d\xi, \end{aligned} \quad \text{(C.8)}$$

where the numbers in brackets denote order of ξ derivatives. Notice that ξ is a dummy variable and x is now an arbitrary fixed point in the ξ coordinate. Following the traditional Green's function theory, we seek a solution such that:

$$aG^{[6]} + bG^{[4]} + cG^{[2]} + dG = \delta(\xi - x), \quad \text{(C.9)}$$

with boundary conditions such that all boundary terms in (C.8) are eliminated:

$$G^{[n]} \to (\pm il)^n G, \;\; \hat{\phi}^{[n]} \to (\pm il)^n \hat{\phi}; \;\; n = 1, ..., 5, \;\; x \to \pm\infty, \quad \text{(C.10)}$$

where $\delta(\xi - x)$ is the Dirac delta function at $\xi = x$. We are interested in solutions where $a \neq 0$. By integrating (C.9) just across $\xi = x$, from $x - \epsilon$ to $x + \epsilon$ ($\epsilon \to 0$), and requiring continuity of G,$G^{[1]}$,$G^{[2]}$,$G^{[3]}$, $G^{[4]}$, we are left with:

$$aG^{[5]}\Big|_{x-\epsilon}^{x+\epsilon} = 1 \quad \text{(C.11)}$$

Away from $\xi = x$ we can write:

$$G^{[6]} + a_1 G^{[4]} + a_2 G^{[2]} + a_3 G = 0, \tag{C.12}$$

where $a_1 = b/a$, $a_2 = c/a$, $a_3 = d/a$. Seeking a solution of the form:

$$G \sim e^{i\sigma\xi}, \tag{C.13}$$

we obtain the characteristic polynomial:

$$\sigma^6 - a_1\sigma^4 - a_2\sigma^2 - a_3 = 0. \tag{C.14}$$

For the case in which we are interested, the roots of (C.13) can be written as:

$$\sigma_1 = -\sigma_4 = l, \tag{C.15}$$

$$\sigma_2 = -\sigma_5 = iL_1, \tag{C.16}$$

$$\sigma_3 = -\sigma_6 = iL_2. \tag{C.17}$$

where l, L_1, L_2 are positive real numbers, and can be obtained from the roots of the bi-cubic polynomial (C.14). We now write the solution for the source function:

$$G(\xi, x) = \begin{cases} G_+ = A_G e^{il(\xi - x)} + B_G e^{L_1(\xi - x)} + C_G e^{L_2(\xi - x)} & \text{if} \quad \xi < x \\ G_- = A_G e^{il(x - \xi)} + B_G e^{L_1(x - \xi)} + C_G e^{L_2(x - \xi)} & \text{if} \quad \xi > x \end{cases} \tag{C.18}$$

Continuity of G, $G^{[2]}$, $G^{[4]}$ are satisfied automatically, as are the boundary conditions at $\pm\infty$. Continuity of $G^{[1]}$, $G^{[3]}$, and substitution of (C.18) into (C.11) gives 3 equations for the 3 unknowns A_G, B_G, and C_G, the solution being:

$$A_G = \frac{-i}{2al\left(l^2 + {L_1}^2\right)\left(l^2 + {L_2}^2\right)} \tag{C.19}$$

$$B_G = \frac{1}{2al\left(l^2 + {L_1}^2\right)\left({L_1}^2 - {L_2}^2\right)} \tag{C.20}$$

$$C_G = \frac{1}{2al\left(l^2 + {L_2}^2\right)\left({L_2}^2 - {L_1}^2\right)} \tag{C.21}$$

(C.19) can be rearranged to give:

$$A_G = \frac{-il}{2\left(2l^6 - a_1 l^4 + a_3\right)}. \tag{C.22}$$

From (C.8) we can write:

$$\begin{aligned} \hat{\phi}(x) &= \int_{-\infty}^{+\infty} G(\xi, x) g\hat{f}(\xi) d\xi \\ &= \int_{-\infty}^{x} G_-(\xi, x) g\hat{f}(\xi) d\xi + \int_{x}^{+\infty} G_+(\xi, x) g\hat{f}(\xi) d\xi. \end{aligned} \tag{C.23}$$

We arbitrarily choose:

$$\hat{f}(x) = D_s \exp\left(-\beta_s x^2\right). \tag{C.24}$$

For sufficiently large values of x (progressive wave traveling to greater values of x), and using (C.22):

$$\begin{aligned} \hat{\phi}(x) &= \int_{-\infty}^{x} G_-(\xi, x) g\hat{f}(\xi) d\xi \\ &= g D_s \left[A_G I_1 e^{ilx} + B_G I_2 e^{-L_1 x} + C_G I_3 e^{-L_2 x}\right], \end{aligned} \tag{C.25}$$

where

$$I_1 = \int_{-\infty}^{+\infty} \exp\left(-\beta_s x^2 - ilx\right) dx = \sqrt{\frac{\pi}{\beta_s}} \exp\left(-\frac{l^2}{4\beta_s}\right), \tag{C.26}$$

$$I_2 = \int_{-\infty}^{+\infty} \exp\left(-\beta_s x^2 + L_1 x\right) dx = \sqrt{\frac{\pi}{\beta_s}} \exp\left(\frac{L_1^2}{4\beta_s}\right), \tag{C.27}$$

$$I_3 = \int_{-\infty}^{+\infty} \exp\left(-\beta_s x^2 + L_2 x\right) dx = \sqrt{\frac{\pi}{\beta_s}} \exp\left(\frac{L_2^2}{4\beta_s}\right). \tag{C.28}$$

$$\tag{C.29}$$

I_2 and I_3 become negligibly small as $x \to \infty$, so:

$$\hat{\phi}(x) \approx g D_s A_G I_1 e^{ilx}. \tag{C.30}$$

We here are interested in waves propagating in the x direction. The desired progressive wave solution (waves propagating in x) of (C.1) and (C.2) away from the source region ($x \to \infty$) is:

$$\eta = \eta_0 e^{i(kx-\omega t)} \tag{C.31}$$

$$\tilde{\phi} = \tilde{\phi}_0 e^{i(kx-\omega t)} \tag{C.32}$$

$$\tilde{\phi}_0 = \frac{ig\eta_0}{\omega\left[1 + C_3(kh)^2 + C_4(kh)^4\right]} \tag{C.33}$$

$$\omega^2 = gk^2h\frac{1 + C_1(kh)^2 + C_2(kh)^4}{1 + C_3(kh)^2 + C_4(kh)^4}, \tag{C.34}$$

Setting $\lambda = 0$ (no y dependence) and $l = k$ we can write:

$$\tilde{\phi}(x, y, t) = gD_s A_G I_1 e^{i(kx-\omega t)}. \tag{C.35}$$

Substitution of (C.32) and (C.33) into (C.35), gives the relationship between the source function amplitude D_s and the desired wave amplitude η_0:

$$D_s = \frac{i\eta_0}{\omega A_G I_1\left[1 + C_3(kh)^2 + C_4(kh)^4\right]}. \tag{C.36}$$

BIBLIOGRAPHY

Airy, G. B. (1845). *Tides and waves.* Encycl. Metrop. Section IV.

Beji, S. and J. A. Battjes (1993). Experimental investigations of wave propagation over a bar. *Coastal Engineering 19*(1,2), 151–162.

Boussinesq, J. (1871). Theorie de l'intumescence liquide appelee onde solitaire ou de translation se propageant dans un canal retangulaire. *Comtes Rendus Acad Sci. 72*, 755–759.

Boussinesq, J. (1872). Théorie des ondes et des remous qui se propaent le long d'un canal rectangulaire horizontal, en communiquant au liquide contenu dans ce canal des vitesses sensiblement pareilles de la surface au dond. *Math. Pures Appliq. 17*, 55–108.

Broer, L. J. F. (1974). On the hamiltonian theory of surface waves. *Appl. Sci. Res. 30*, 430–446.

Broer, L. J. F. (1975). Approximate equations for long water waves. *Appl. Sci. Res. 31*, 377–395.

Broer, L. J. F., E. W. C. van Groesen, , and J. M. W. Timmers (1976). Stable model equations for long water waves. *Appl. Sci. Res. 32*, 619–636.

Chen, Y. and P. L.-F. Liu (1995). Modified Boussinesq equations and associated parabolic models for water wave propagation. *J. Fluid Mech. 288*, 351–381.

Demirbilek, Z. and W. C. Webster (1992). Application of the Green-Naghdi theory of fluid sheets to shallow waterwave problems. Technical Report CERC-92-11, U.S. Army Corps of Engineers, Vicksburg, MS, 45pp.

Dingemans, M. W. (1994). Comparison of computations with Boussinesq-like models and laboratory measurements. Report H-1684.12, Delft Hydraulics, 32pp.

Fenton, J. D. (1972). A ninth-order solution for the solitary wave. *J. Fluid Mech. 53*(2), 237–246.

Green, A. E., N. Laws, and P. M. Naghdi (1974). On the theory of water waves. *Proc. Roy. Soc. A 338*, 43–55.

Green, A. E. and P. M. Naghdi (1976). A derivation of equations for wave propagation in water of variable depth. *J. Fluid Mech. 78*, 237–246.

Grilli, S. T., J. Skourup, and I. A. Svendsen (1989). An efficient boundary element method for nonlinear water waves. *Engng. Anal. with Boundary Elements 6*, 97–107.

Grimshaw, R. (1971). The solitary wave in water of variable depth. *J. Fluid Mech. 86*, 415–431.

Hansen, J. B. and I. A. Svendsen (1979). Regular waves in shoaling water, experimental data. Series Paper 21, ISVA, Techn. Univ. Denmark, 20pp. plus appendices.

Hasselmann, K. (1962). On the nonlinear energy transfer in a gravity wave spectrum. *J. Fluid Mech. 12*, 481–500.

Israeli, M. and S. A. Orszag (1989). Approximations of radiation boundary conditions. *J. Comp. Phys. 41*, 115–130.

Kirby, J. T. (1997). Nonlinear, dispersive long waves in water of variable depth. In *Gravity waves on water of variable depth. Computational Mechanics Publications, 10*, 55–125. J. N. Hunt (ed).

Kirby, J. T. and G. Wei (1994). Derivation and properties of a fully nonlinear, extended Boussinesq model. In *Proc. IAHR Symposium: Waves - Phys. and Num. Model.*, Vancouver, 386–395.

Korteweg, D. J. and G. deVries (1895). On the change of form of long waves advancing in a rectangular canal and on a new type of long stationary wave. *Phil. Mag. 5*(39), 422–443.

Laitone, E. V. (1960). The second approximation to cnoidal and solitary waves. *J. Fluid Mech. 9*, 430–444.

Larsen, J. and H. Dancy (1983). Open boundaries in short-wave simulations-a new approach. *Coastal Engineering 7*, 285–297.

Longuet-Higgins, M. S. and J. D. Fenton (1974). On the mass, momentum, energy and circulation of a solitary wave. *Proc. Roy. Soc. London A 340*, 471–493.

Luth, H. R., G. Klopman, and N. Kitou (1994). Kinematics of waves breaking partially on an offshore bar; ldv measurements of waves with and without a net onshore current. Report H-1573, Delft Hydraulics, 40pp.

Madsen, P. A., R. Murray, and O. R. Sørensen (1991). A new form of Boussinesq equations with improved linear dispersion characteristics. *Coastal Engineering 15*, 371–388.

Madsen, P. A. and O. R. Sørensen (1992). A new form of Boussinesq equations with improved linear dispersion characteristics. part 2. a slowly-varying bathymetry. *Coastal Engineering 18*, 183–204.

Madsen, P. A. and O. R. Sørensen (1993). Bound waves and triad interactions in shallow water. *Ocean Engng 20*, 359–388.

McCowan, A. D. (1987). The range of application of Boussinesq type numerical short wave models. In *Proc. 22nd IAHR Congr.*

Mei, C. C. (1989). *The Applied Dynamics of Ocean Surface Waves.* World Scientific. pp. 740.

Mei, C. C. and B. L. Méhauté (1966). Note on the equations of long waves over an uneven bottom. *J. Geophys. Res. 71*, 393–400.

Mooiman, J. (1991). Boussinesq equations based on a positive definite hamiltonian. Report 294, Delft Hydraulics, 103pp.

Nwogu, O. (1993). An alternative form of the Boussinesq equations for nearshore wave propagation. *J. Waterway, Port, Coast., Ocean Engng. 119*, 618–638.

Ohyama, T., W. Kiota, and A. Tada (1994). Applicability of numerical models to nonlinear dispersive waves. *Coastal Engineering 24*, 297–213.

Peregrine, D. H. (1966). Long waves on a beach. *J. Fluid Mech. 27*, 815–820.

Schäffer, H. A. and P. A. Madsen (1995). Further enhencements of Boussinesq-type equations. *Coastal Engineering 26*(26), 1–14.

Seabra-Santos, F. J., D. P. Renouard, and A. M. Temperville (1987). Numerical and experimental study of the transform of a solitary wave over a shelf or isolated obstacle. *J. Fluid Mech. 176*, 117–134.

Serre, F. (1953). Contribution a l'etude des ecoulements permanents et variables dans les canaux. *La Houille Blanche 3*, 374–388.

Shapiro, R. (1970). Smoothing, filtering, and boundary effects. *Geophys. and Space Phys. 8*(2), 359–387.

Shields, J. J. (1986). A direct theory for waves approaching a beach. Dissertation, University of California at Berkeley, 137pp.

Shields, J. J. and W. C. Webster (1988). On direct methods in water-wave theory. *J. Fluid Mech. 197*, 171–199.

Su, C. H. and C. S. Gardner (1969). Korteweg-de Vries equation and generalizations. iii. Derivation of Korteweg-de Vries equation and Burgers equation. *J. Math. Phys. 10*, 536–539.

Tanaka, M. (1986). The stability of solitary waves. *Phys. Fluids 29*, 650–655.

Van der Veen, W. A. and F. W. Wubs (1993). A hamiltonian approach to fairly low and fairly long gravity waves. Report W-9314, Department of Mathematics, University of Groningen, 25pp.

Webster, W. C. and J. V. Wehausen (1995). Bragg scattering of water waves by Green-Naghdi theory. *Z. angew Math. Phys. 46*(Special issue), S566–S583.

Wei, G. (1997). Simulation of water waves by Boussinesq models. Dissertation, University of Delaware, 202pp.

Wei, G., J. T. Kirby, S. T. Grilli, and R. Subramanya (1995). A fully nonlinear Boussinesq model for surface waves. Part 1. Highly nonlinear unsteady waves. *J. Fluid Mech. 294*, 71–92.

Wilmott, C. J. (1981). On the validation of models. *Physical Geography 2*(2), 219–232.

Witting, J. M. (1984). A unified model for the evolution of nonlinear water waves. *J. Comp. Phys. 56*, 203–239.